JOINT INSTITUTE FOR NUCLEAR RESEARCH

The Report on Project

“MPD. MultiPurpose Detector”

02-1-1065-3-2011/2025

Feasibility study of the second stage of the MPD

Theme: 02-0-1065-2007/2026

LEADER *V.M.Golovatyuk, V.D.Kekelidze, V.G.Riabov*

Submitted

LHEP Science and Technology Council

TABLE OF CONTENTS

1. Introduction

The Nuclotron-based Ion Collider fAcility (NICA) is under construction at the Joint Institute for Nuclear Research (JINR), with commissioning of the facility expected in late 2025. The Multi-Purpose Detector (MPD) is one of the two dedicated heavy-ion collision experiments at NICA and its components are currently in production. Its main scientific purpose is to search for novel phenomena in the baryon-rich region of the QCD phase diagram by means of colliding heavy-ion beams in the energy range of 4 GeV $\leq \sqrt{s_{NN}} \leq$ 11 GeV and/or studying fixed-target collisions in the energy range 2.3 GeV $\leq \sqrt{s_{NN}} \leq$ 3.5 GeV.

The structure of the QCD phase diagram is shown in Fig. 1, which indicates different phases of QCD matter. The Critical End-Point (CEP) occurs where the phase transition from the hadronic phase to a Quark-gluon plasma (QGP) changes from a smooth crossover to the first-order transition. Calculations within the thermal model indicate that the highest baryon density is achieved in the NICA energy range, which makes the MPD particularly well suited to experimentally search for the existence of the CEP. Studies at NICA can also contribute to investigation of the properties of nuclear matter inside neutron stars, which is one of the goals of modern astrophysics. The recent observation of a neutron star merger, both by direct detection of gravitational waves as well as in the electromagnetic spectrum initiated a new era of multi-messenger astronomy. Recent model calculations reveal that in a neutron star merger, nuclear matter reaches densities and temperatures similar to those occurring in heavy-ion collisions in the NICA energy range [1,2], that are therefore relevant to investigate the onset of deconfinement, albeit at higher isospin density. Therefore, the MPD offers a unique opportunity to complement the study of neutron star mergers by obtaining data from a terrestrial laboratory experiment.

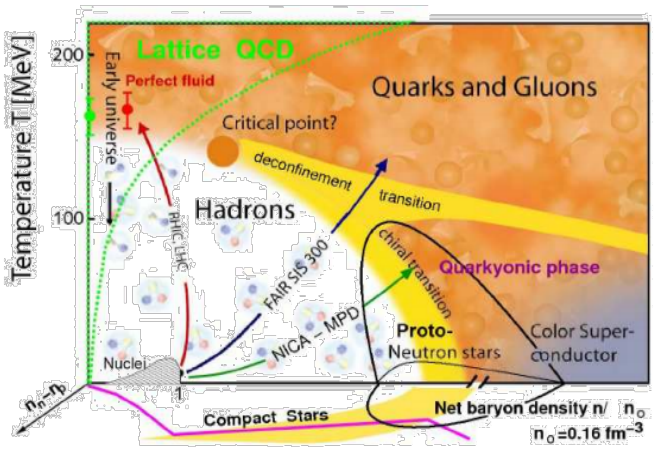

Fig. 1. Schematic representation of the QCD phase diagram.

For the first beams, we can expect Xe or Bi nuclei, which provide more reliable operation of the NICA injection and acceleration complexes during the commissioning. The kinetic energy of the beam provided by the Nuclotron will be limited to 2.5 GeV per nucleon. Therefore, the initial collision energy may vary from 4 up to 7 GeV and from 2.3 to 2.9 GeV in collider the fixed-target modes. The properties of the matter created in heavy-ion collisions at NICA energies will be characterized using a variety of observables. The global quantities, such as multiplicity (dN/dy) and transverse energy (E_T) are considered as the main tools to reveal the energy density achieved in the collision. The first-day key global observables that can be measured with the initial data samples are expected to provide the basic information for physics studies relevant to the onset of

quark confinement, chiral symmetry restoration and for the search of the CEP on the phase-diagram of strongly interacting matter.

Hadrochemistry. The structure of the QCD phase diagram is tested by measuring abundances of hadron species, while different regions of the diagram are accessible by varying the collision energy. Experimental results on hadron abundances produced in heavy-ion collisions in the range from AGS to LHC energies indicate that the final state of such collisions is close to chemical equilibrium. Thus, the yields can be fitted by the thermal statistical model using two free parameters, namely, T and μ_B. Assuming the measured multiplicities to be preserved throughout the final hadron-resonance cascade expansion, the analysis reveals the hadronization point along the QCD parton-hadron boundary line in terms of the extracted T and μ_B values. Within the thermal statistical model, one can show that the NICA energy range covers the region where the matter created in nuclear collisions transitions from net baryon to meson-dominated matter.

MPD is well suited for the measurement and identification of hadrons in a wide momentum and rapidity range thanks to charged particle track reconstruction in the TPC and particle identification by ionization loss (<dE/dx>) measurements in the TPC and time-of-flight measurements in the TOF. Besides, neutral mesons can be reconstructed using their decay channels with photons in the final state where photons can be detected directly in the ECAL or measured as e^+e^- pairs from photon conversion in the beam pipe and inner vessels of the TPC. To summarize, MPD has excellent capabilities for the measurement of a wide variety of identified hadrons including different states of π, K, p, $\phi(1020)$, Λ, Σ, Ξ, Ω, etc., and light (hyper)nucei such as d, t, ^{3}He, $^{\Lambda}$H3, $^{\Lambda}H^4$, and $^{\Lambda}He^4$.

An example of a relevant observable to study the onset of deconfinement [55] is the kaon-to-pion ratio. Fig. 2a) shows the excitation functions for K^+/π^+, K^-/π^- and Λ/π^+ ratios. From AGS up to LHC energies, K^+/π^+ and Λ/π^+ ratios show a peak structure, whereas the K^-/π^- ratio exhibits a monotonic rise [4]. This feature is very well described by the thermal statistical model of chemical freezeout where it appears to be due to the drop of the baryochemical potential with increasing collision energy and to the transition from baryon dominance to meson dominance. A similar behavior is also observed in other model calculations, some of which even show a sharper peak, followed by a plateau in the K^+/π^+ ratio as a function of T/μ_B. The MPD will offer the capability to cover this energy range using a single experimental set up and to provide results of higher precision.

Anisotropic flow. The predicted first-order phase transition between hadronic and QGP phase is characterized by a dramatic drop in the pressure, or a softening of the EoS [5]. Signals such as anisotropic flow are very promising in this context due to their sensitivity to the EoS. The rapidity-odd component of the directed flow (v_1) can probe the very early stages of the collision as it is generated during the passage time of the two colliding nuclei $t_{pass} = 2R/\gamma_s\beta_s$. Both hydrodynamic and transport model calculations indicate that the directed flow of charged particles, especially baryons at midrapidity, is very sensitive to the EoS. The slope of the rapidity dependence dv_1/dy close to mid-rapidity is a convenient way to characterize the overall magnitude of the rapidity odd component of the directed flow signal. A minimum in dv_1/dy at midrapidity could be related to the softening of the EoS due to a first order phase transition between hadronic matter and QGP. The elliptic flow v_2 is one of the most extensively studied observables in relativistic nucleus-nucleus collisions and was measured in different experiments in the last three decades. However, high-statistics differential measurements of v_2 as a function of centrality, p_T and rapidity, for different particle species are not yet available in the NICA energy range. In order to describe the existing $v_2(p_T)$ results at NICA energies, calculations with state-of-the-art models were performed [6,7]: hybrid models with QGP formation provide a relatively good description of $v_2(p_T)$ of protons in Au+Au collisions at $\sqrt{s_{NN}}$ = 7.7 GeV and above, pure hadronic transport models generally

underestimate the measured v_2 values, see Fig. 2b). The situation is different for Au+Au collisions at $\sqrt{s_{NN}}$ = 4.5 GeV and below, where pure hadronic transport system seems to explain the new $v_2(p_T)$ measurements from the STAR fixed-target program, see Fig. 1c). The results of model to data comparison for $v_2(p_T)$ at $\sqrt{s_{NN}}$ = 7.7 GeV and 4.5 GeV may indicate that at NICA energies a transition occurs from partonic to hadronic matter. The high-statistics differential measurements of v_n in MPD experiment at NICA are expected to provide valuable information about this parton-hadron transient energy domain.

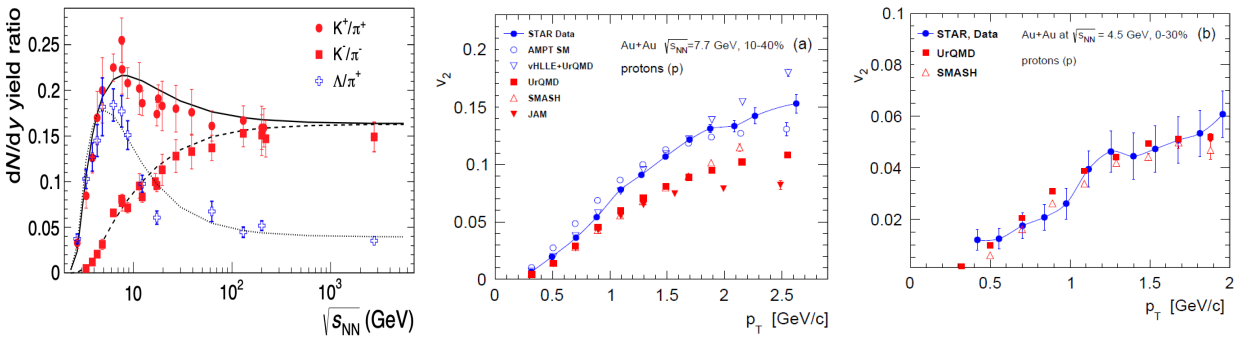

Fig. 2. (a) Excitation functions for K^+/π^+, K^-/π^- and Λ/π^+ ratios, the lines represent the results of the thermal statistical model of chemical freezeout. Momentum dependence of v_2 of protons from 10-40% central Au+Au collisions at $\sqrt{s_{NN}}$ = 7.7 GeV and (b) 0-30% central Au+Au collisions at $\sqrt{s_{NN}}$ = 4.5 GeV. Blue closed circles correspond to the experimental data from STAR experiment [8], other symbols to the results from different models as indicated.

Femtoscopy. Femtoscopy is used in heavy-ion collision to determine the size of the particle-emitting produced system and consequently, details of the space-time dynamics of that system's evolution. In particular, two-pion measurements are straightforward to perform due to the high statistics of pion production and the well understood methodology. The technique of the correlation function used in the measurements is, to a good approximation, insensitive to single particle acceptance effects. As a result, measurements of the two-pion femtoscopic correlation functions are usually among the first ones performed at accelerator experiments immediately after their startup and as such, are excellent candidates for first-day physics measurements. Femtoscopy measurements have been performed for several decades, as a function of collision energy, colliding system, collision centrality, pair transverse momentum, reaction plane orientation and more [9-10]. The dependence on collision energy of the freeze-out volume, obtained from two-pion interferometry is of particular interest for the MPD. A rather striking non-monotonic behavior of the volume is observed in the NICA energy range. However, it is unclear whether this can be explained by the onset of multiparticle production in elementary reactions or by systematic uncertainties. The measurements at energies above $\sqrt{s_{NN}}$ = 7.7 GeV were performed with detectors in a collider geometry, whereas the results obtained at lower energies suffer from limited statistics and were performed in fixed-target experiments. More precise data, based on a large-statistics sample in a collider geometry experiment and analyzed with modern techniques will be provided by the MPD.

Fluctuations. An important feature of the QCD phase structure is the existence of a CEP, followed by a first order phase transition line at higher values of μ_B. If the phase trajectory of the system passes near this point, significant variations of the system's thermodynamical parameters are expected [11]. Such variations can be found in the analyses of event-by-event fluctuations of

conserved charges, for example, the baryon number or strangeness. QCD-based calculations indicate that the moments of event-by-event multiplicity distributions, as well as their combinations, are sensitive to the correlation length, a characteristic parameter of a phase transition, and to the susceptibilities of the conserved charges. Moreover, higher moments of the distributions of conserved quantities have stronger dependence on the correlation length. The promising higher moments are the skewness and kurtosis. Recent STAR measurements from the RHIC-BES program [12] do not show any prominent signs of a non-monotonic behavior of the excitation function for the net-proton moments in central Au+Au collisions in the region below $\sqrt{s_{NN}}$ =20 GeV, which may be an effect of signal dissipation in the hadronic phase or effect of the limited phase space. The MPD experiment at NICA will be able to scan the region of the collision energies $\sqrt{s_{NN}}$ = 2.3-11 GeV with significantly higher precision.

Electromagnetic probes. Electromagnetic probes are sensitive to two main characteristic properties of the QGP, the deconfinement of quarks and gluons and the chiral symmetry restoration. They are penetrating probes carrying information about the medium at the time of production. The main topic of interest is the identification of the thermal radiation emitted at the early stage of the collision where QGP formation and deconfinement occur, as well as during the subsequent hadronization phase, where chiral symmetry restoration effects take place.

The MPD is very well suited for the study of electron pairs, covering the entire invariant mass range of interest. It benefits from a large acceptance, excellent particle ID and the NICA high integral luminosity. Electrons will be identified via their dE/dx in the TPC, time-of-flight in the TOF and E/p = 1 in the ECAL. The MPD will focus on an energy range that has not been covered in the study of EM probes, but is crucial for understanding the thermal radiation. The dilepton yield in the intermediate mass region (IMR), 1-3 GeV/c^2, has been singled out as the most appropriate region to observe the thermal radiation from the QGP. At NICA energies, contribution from heavy flavor decays is negligible allowing a relatively clean measurement of the thermal radiation in the IMR. The inverse-slope parameter, T_s, of the invariant mass spectra in this mass range is closely related to the initial temperature T_i of the fireball and thus can be regarded as a "thermometer" for the heavy-ion collision, see Fig.3 [13]. A very interesting result of these calculations is the prediction of QGP thermal radiation down to collision energies as low as $\sqrt{s_{NN}}$ = 6-8 GeV setting the onset of QGP formation well within the energy range covered by NICA.

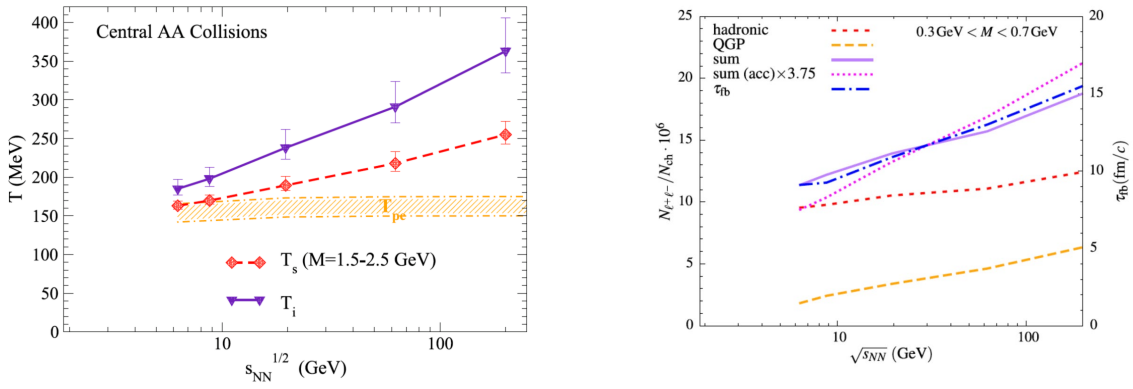

Fig. 3. Excitation function of the inverse-slope parameter (a) and low-mass thermal dilepton radiation (b).

In the low-mass region (LMR), < 1 GeV/c^2, an enhancement has been observed in all heavy-ion collision systems and at all energies. At the SIS-17, SPS and RHIC energies, the excess,

dominated by the thermal radiation from the hadron gas, is linked to the restoration of chiral symmetry that manifests itself in a broadening of the ρ(770) meson spectral function [14]. The dilepton excess, integrated over a mass window 0.3–0.7 GeV/c^2, was found to be proportional to the fireball lifetime, see Fig. 3. The dilepton excess in the LMR can therefore be considered as a "chronometer" of the fireball. Deviations from the proportionality of the dilepton excess and the fireball lifetime could then signal lifetime variations associated with the conjectured critical phenomena and onset of a first order phase transition.

Real photons carry the same physics information are thus an important part of the physics program of relativistic heavy-ion experiments. The inclusive photon yield includes "direct" photons on top of an overwhelming background originating from hadronic decays, mostly from π^0. The "direct" photons are produced either in hard scattering processes or emitted as thermal radiation from the produced medium. Indeed, at the high energies of RHIC and LHC, a signal of direct photons, on top of the hadronic background, has been identified [15-16], consistent with pQCD calculations at $E_\gamma > 5$ GeV and thermal radiation from the QGP and hadronic phase at lower energies. At the lower SPS energy, only an upper limit [17] or a small effect was established. The MPD will make measurements of real photons by detecting them in the ECAL or using the conversion method, but in both cases, the measurements will be quite challenging.

[1] S. Blacker, N.U.F. Bastian, A. Bauswein, D.B. Blaschke, T. Fischer, M. Oertel, T. Soultanis, S. Typel, Phys. Rev. D 102(12), 123023 (2020). DOI 10.1103/PhysRevD.102.123023

[2] E.R. Most, L. Jens Papenfort, V. Dexheimer, M. Hanauske, H. Stoecker, L. Rezzolla, Eur. Phys.J. A 56(2), 59 (2020). DOI 10.1140/epja/s10050-020-00073-4

[3] M. Gazdzicki, Eur. Phys. J. ST 229(22-23), 3507 (2020). DOI 10.1140/epjst/e2020-000090-9

[4] A. Andronic, Int. J. Mod. Phys. A 29, 1430047 (2014). DOI 10.1142/S0217751X14300476

[5] H. Stoecker, Nucl. Phys. A750, 121 (2005). DOI 10. 1016/j.nuclphysa.2004.12.074

[6] A. Taranenko, P. Parfenov, A. Truttse, Phys. Part. Nucl.51(3), 309 (2020). DOI 10.1134/S1063779620030296

[7] P. Parfenov, A. Taranenko, D. Idrisov, V.B. Luong, N. Geraksiev, A. Demanov, A. Povarov, V. Kireyeu, A. Truttse, E. Volodihin, (2020)

[8] J. Adam, et al., Phys. Rev. C 103(3), 034908 (2021). DOI 10.1103/PhysRevC.103.034908

[9] J. Adamczewski-Musch, et al., Phys. Lett. B795, 446 (2019). DOI 10.1016/j.physletb.2019.06.047

[10] C. Adler, et al., Phys. Rev. Lett. 87, 082301 (2001). DOI 10.1103/PhysRevLett.87.082301

[11] M. Stepanov, Phys. Rev. Lett. 102, 032301 (2009). DOI 10.1103/PhysRevLett.102.032301

[12] J. Adam, et al., Phys. Rev. Lett. 126(9), 092301 (2021). DOI 10.1103/PhysRevLett.126.092301

[13] R. Rapp, H. van Hees, Phys. Lett. B 753, 586 (2016). DOI 10.1016/j.physletb.2015.12.065

[14] J. Adamczewski-Musch, et al., Nature Phys. 15(10), 1040 (2019). DOI 10.1038/s41567-019-0583-8

[15] A. Adare, et al., Phys. Rev. Lett. 104, 132301 (2010). DOI 10.1103/PhysRevLett.104.132301

[16] L. Adamczyk, et al., Phys. Lett. B 770, 451 (2017). DOI 10.1016/j.physletb.2017.04.050

[17] R. Albrecht, et al., Phys. Rev. Lett. 76, 3506 (1996). DOI 10.1103/PhysRevLett.76.3506

2. MPD performance studies

During the period of 2020-24 a comprehensive program of MPD detector performance and feasibility studies was carried out with emphasis on the collider mode of MPD-NICA operation with heavy ion beams. The results of these studies have been presented at many international conferences where collaboration members gave over 200 oral presentations. The number of physics feasibility publications in referred journals exceeded 60 with the first collaboration paper published in a high-rated European journal EPJA ("Status and initial physics performance studies of the MPD experiment at NICA", Eur.Phys.J.A 58 (2022) 7, 140). Below, we highlight selected results with a short summary of activities supported by the references in the end.

2.1 Event centrality

In heavy-ion collisions, centrality of a collision is characterized by the impact parameter, which is the distance between the centers of the nuclei in the plane perpendicular to the beam axis. The impact parameter determines the overlap region of the nuclei and the size of the collision system. The value of the impact parameter is not accessible experimentally and must be obtained from the data by using the measurable quantities approximately proportional to the nuclear overlap region. The centrality of an event can be characterized by the charged particle multiplicity or transverse energy measured in a predefined pseudorapidity interval, or by the energy of fragments registered in the forward direction. Different procedures are considered to determine the centrality in the MPD experiment. Below, we present centrality determined from the charged-particle multiplicity measured in the TPC at midrapidity.

Centrality was evaluated for events with a reconstructed vertex within |z-vertex| < 130 cm where the trigger efficiency remains constant. Rather loose selections were used for the reconstructed tracks: number of TPC hits $N_{TPC} > 10$, transverse momentum $p_T > 0.1$ GeV/c, track matching to the primary vertex |DCA| < 2 cm, and track pseudirapidity $|\eta| < 0.5$. Each track is corrected for reconstruction efficiency estimated as a function of event z-vertex and track pseudorapidity to account for TPC inefficiency. A typical multiplicity distribution is shown in Fig. 1. The event centrality is estimated as a percentile of the total multiplicity with the maximum value accounting for the limited trigger efficiency, which samples only 91% of inelastic cross section.

The standard Monte Carlo Glauber (MCG) model was used to reproduce the reconstructed multiplicity distribution and estimate the geometrical parameters of the collisions. The MCG particle multiplicity distribution is modeled as a sum of particles produced from a set of independent emitting sources (N_a), each producing particles according to a negative binominal distribution NBD(μ, k). The number of emitting sources is parameterized as $N_a = f \cdot N_{part} + (1-f) \cdot N_{coll}$, where N_{part} and N_{coll} are the number of participating nucleons and number of inelastic binary nucleon-nucleon collisions in the simulated MCG event. The parameters μ, k and f are varied to better describe the measured multiplicity distribution in the range of multiplicity $N_{tracks} > 10$. The red curve in Fig. 1 shows the result of this procedure, a good agreement between the measured and MCG-simulated multiplicity distributions in the overlap region can be observed. The ratio of the reconstructed and MCG multiplicity distributions serves as an estimate of the trigger efficiency, the weighted average efficiency estimated from the ratio is ~ 90%, which is very close to the expected value of 91%. The MCG model is then used to estimate the initial geometry of the centrality classes. The values of the impact parameter, N_{part} and N_{coll} for 10% centrality intervals are evaluated for the UrQMD, PHSD, DCM-QGSM-SMM and PHQMD event generators. The right panel in Fig. 1 shows example of the mean and RMS values for impact parameter distributions with markers and error bars, respectively, the points for different event generators are staggered for visibility. The extracted values of model parameters are in good agreement.

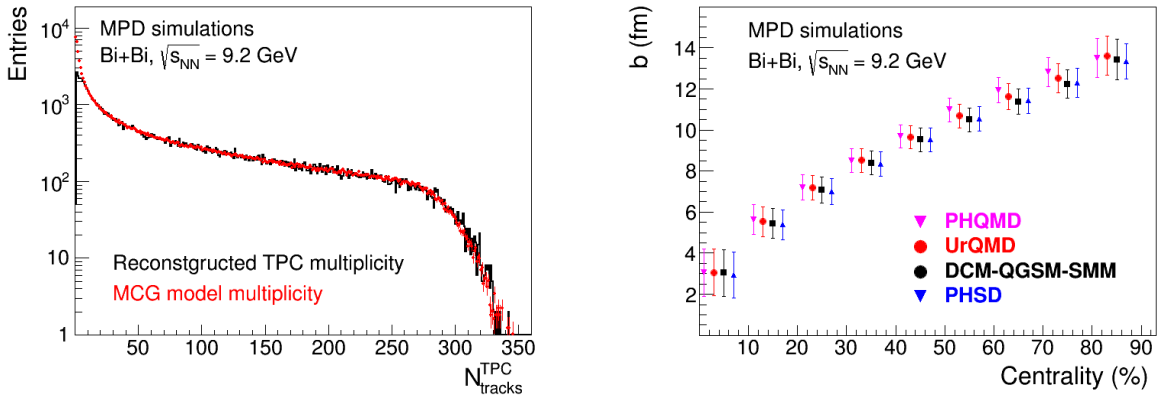

Fig. 1. The reconstructed TPC (black) and MCG modeled (red) multiplicity distributions (left). Values of the impact parameter for 10% centrality intervals modeled with the UrQMD, PHSD, DCM-QGSM-SMM, and PHQMD event generators (right).
Results are presented for Bi+Bi collisions at $\sqrt{s_{NN}}$ = 9.2 GeV.

2.2 Light flavor identified hadrons

Light-flavored hadrons are copiously produced and play an important role in understanding the physics of relativistic heavy-ion collisions. Experimental study of charged pion, kaon and (anti)proton production is used to determine the conditions for the formation of hot and dense baryonic matter and can provide insight into the underlying reaction dynamics. Hadron yields, spectra and ratios show whether conditions favorable for a phase transition to QGP are achieved. They also allow testing of thermal and chemical equilibrium in the system, unveiling the freeze-out space-time geometry of the source, as well as addressing the collective effects in the longitudinal and transverse expansion of the fireball.

Charged particle identification was achieved by a combination of energy loss dE/dx and time-of-flight measurements, corrections have been made for hadron misidentification, for reconstruction losses, for geometrical acceptance, as well as for the contamination from secondary interactions in the detector material and from weak decays of hyperons (relevant for pions and protons). The yields of charged hadrons are obtained in centrality-selected events and for several rapidity intervals. As an example, Fig. 2 shows the transverse momentum spectra of positively charged pions (left panel) and protons (central panel) for 0-10% central Bi+Bi collisions at $\sqrt{s_{NN}}$ = 9.2 GeV . The spectra shown are in rapidity intervals of Δy =0.2 in the range $-1 < y < 1$ and are scaled down relative to the data at midrapidity by successive orders of two for clarity. The MPD detector has limited p_T coverage at low transverse momentum and to extrapolate spectra to the unmeasured p_T –range, the spectra were fitted with appropriate functional forms. The extrapolation varies for different particle species, but does not exceed 5%, 10%, and 15% for pions, kaons, and protons, respectively.

The rapidity density distributions (dN/dy) of positively charged hadrons (π^+, K^+, p) are obtained by integrating the transverse momentum spectra, see right panel of Fig.2. The measurements for pions and kaons cover approximately 65% of the total phase-space and the rapidity distributions can be approximated by a Gaussian, thus, an integrated mean total multiplicity of π, K can be obtained with ~10% uncertainty. The situation for protons is more complicated because the shape of their rapidity distributions varies with centrality. The MPD phase-space coverage for protons is not sufficient to reconstruct the total (4π) yield of protons without models assumptions but can accurately predict the proton yields near the beam rapidity.

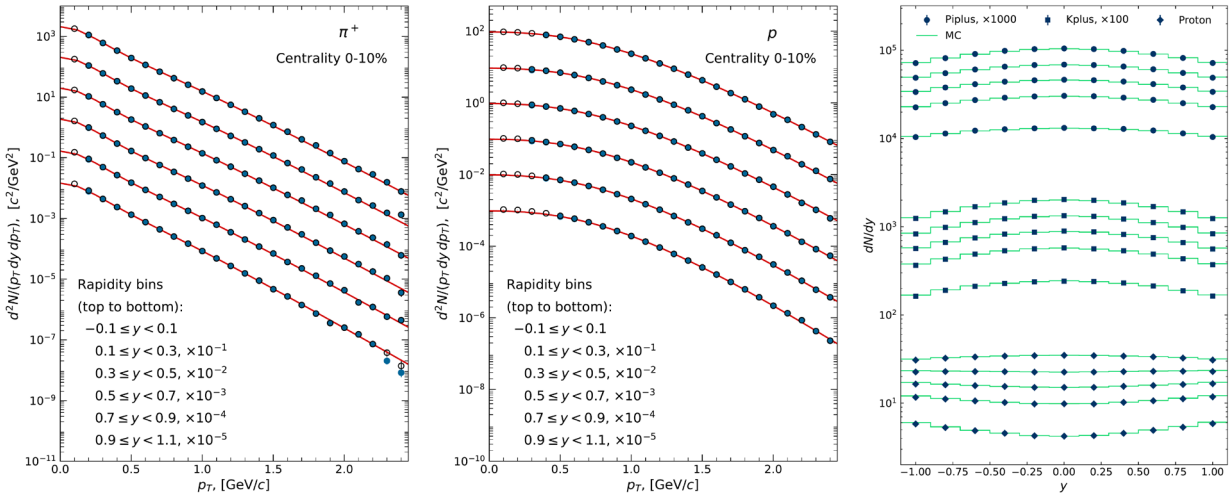

Fig. 2. Invariant p_T -spectra of π^+ (left) and p (center) in different rapidity bins. The reconstructed and generated data are shown with solid and open symbols, respectively. Rapidity distributions of π^+, K^+ and p (right). The reconstructed data are shown by symbols while the model data are depicted by histograms. Examples are shown for 10% central Bi+Bi collisions at $\sqrt{s_{NN}}$ = 9.2 GeV.

Neutral mesons are reconstructed in the decay channel $\pi^0(\eta)\to\gamma\gamma$, where final state photons are measured in the calorimeter (ECAL) or reconstructed as e^+e^- pairs from photons conversion (PCM). The ECAL-ECAL method has the highest efficiency, but measurements at low momenta suffer from poor energy resolution, high hadronic and combinatorial background. In contrast, the PCM-PCM approach takes advantage of much better energy resolution of the tracking system and the superior purity of photon reconstruction at low momenta, resulting in much narrower reconstructed peaks and lower background. However, the method suffers from low efficiency due to small photon conversion probability. The hybrid ECAL-PCM method occupies an intermediate position, sharing the advantages and disadvantages of the above two methods. Nevertheless, measurements with ECAL-PCM and PCM-PCM are important to study the performance and systematic effects in the calorimeter. The available statistics are sufficient to measure only centrality-integrated η meson production using the ECAL-ECAL method. The differential yields measured for π^0 and η mesons as a function of transverse momentum in centrality differential Bi+Bi collisions at $\sqrt{s_{NN}}$ = 9.2 GeV are shown in Fig. 3. The measurements span a wide p_T range from 0.1 to 4.5 GeV/c with the accumulated statistics. The reconstructed spectra are compared to truly generated ones shown with histograms in the same figures. The reconstructed spectra match the generated ones within statistical uncertainties.

2.3. (Multi)strange hyperons and hypernuclei

Since the energy threshold for strangeness production in the QGP phase is smaller than in the hadron gas phase, the enhanced production of strange particles (kaons and hyperons) was proposed as a signature of the phase transition. For hyperons, the increase of the production rate with respect to elementary pp reactions was observed in a broad energy range from AGS to the LHC, stronger for particles with larger strangeness content. However, there are other possible explanations for the observed strangeness enhancement such as multi-mesonic reactions in dense nuclear matter, partial chiral symmetry restoration, vanishing of the canonical suppression with increasing multiplicity or calculations within a core-corona approach. The p_T distributions of hyperons provide important information on the reaction dynamics. Due to their small hadronic reaction cross sections, the transverse momentum spectra of cascades reflect the initial conditions of a collision.

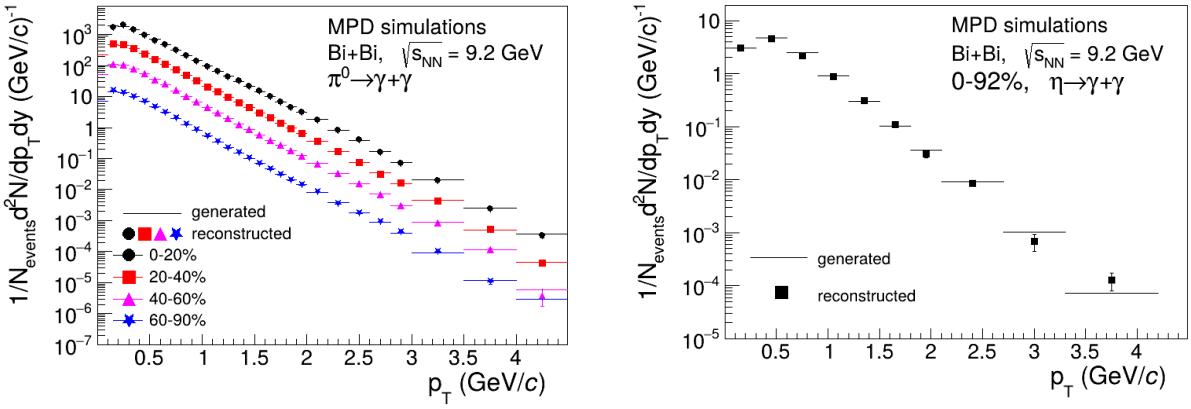

Fig. 3. Differential production spectra for π^0 and η mesons in Bi+Bi collisions at $\sqrt{s_{NN}}$ = 9.2 GeV. Results for π^0 meson are shown in different centrality intervals. The measured points are compared to truly generated spectra shown with histograms.

The reconstruction of Λ ($\bar{\Lambda}$) was carried out using the 'V0' decay mode $\Lambda \rightarrow p + \pi^-$ ($\bar{\Lambda} \rightarrow \bar{p} + \pi^+$). For each event, all possible pairs of (anti)protons and charged pions are identified. For each pair, the point of closest approach of particle trajectories is determined by extrapolating tracks back to the beam axis. In order to reduce combinatorial background, several cuts are imposed. These cuts include: a) the distance of closest approach (DCA) of the daughters to the primary vertex; b) DCA of the V0 particle to the primary vertex; c) the distance between the primary and secondary vertices; d) the value of angle between the direction of V0 momentum vector and the line connecting the primary and secondary vertices. For each selected pair of daughter particles, the invariant mass of the parent hyperon is then calculated. The raw yields of hyperons extracted from the invariant mass distributions are then corrected for the losses due to the finite detector acceptance, track reconstruction efficiency, and the applied cuts. Reconstructed invariant transverse momentum spectra of Λ and $\bar{\Lambda}$ in centrality selected Bi+Bi collisions $\sqrt{s_{NN}}$ = 9.2 GeV are shown in Fig. 4. The reconstructed midrapidity (|y| < 0.5) distributions are shown with solid symbols, while the model-generated distributions are plotted with empty symbols. As one can see, the reconstructed and generated spectra agree within the measurement uncertainties.

Once Λ-hyperons are reconstructed, an analysis is conducted for cascade hyperons using the decay mode $\Xi^- \rightarrow \Lambda + \pi^-$. The Λ candidate for pairing with π^- is determined requiring the invariant mass to be within ±5σ with respect to the nominal value. To improve the signal purity, topological selection criteria similar to (a)–(d) described above are applied. Fig. 4 shows the reconstructed invariant p_T spectra of Ξ^--hyperons in centrality selected Bi+Bi collisions. The difference between the reconstructed and model generated spectra is small. The yield of Ω-hyperon in heavy-ion collisions is small, thus, the analysis was performed in a wider rapidity interval (|y| < 1) for 0-80% central collisions. The right panel of Fig. 4 shows the reconstructed p_T -spectrum of Ω^- in Bi+Bi interactions.

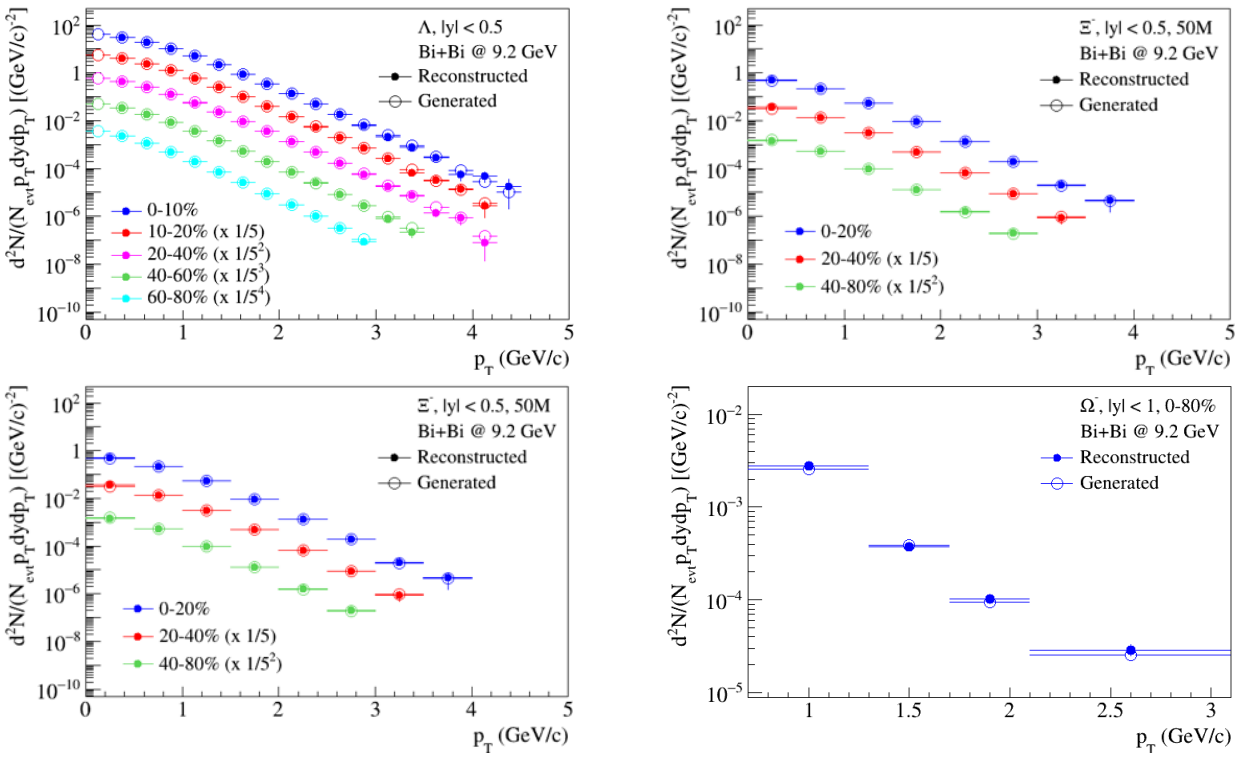

Fig. 4. Transverse momentum spectra of Λ (top left), $\bar{\Lambda}$ (top right), Ξ^- (bottom left) and Ω^- (bottom right) in different centrality Bi+Bi collisions at $\sqrt{s_{NN}}$ = 9.2 GeV. Reconstructed and generated distributions are shown with solid and empty symbols, respectively.

Measurement of hypernuclei is important to better understand properties of the compact neutron stars and to study Λ-N interaction potentials. The raw yields of hypertritons extracted from the invariant mass distribution of ^{3}Heπ^- pairs was then corrected for the total efficiency, which includes the acceptance of the setup, the probability of decay in a given channel (branching), and signal losses due to selection criteria and particle identification. Fig.5 (left panel) shows the invariant p_T spectrum of hypertritons from Bi+Bi collisions. The spectra are obtained for the rapidity interval $|y| < 0.5$ without selection on the collision centrality. The reconstructed and generated distributions are shown with triangles and rectangles, respectively, the agreement between the reconstructed and generated spectra is good in all transverse momentum intervals. The hypertriton yield was analyzed in several intervals of proper time in a range 0.1–1.5 ns to estimate its lifetime. Right panel of Fig. 5 shows the fully corrected distribution of hypertritons as a function of proper time. The slope parameter 'p1' of the fit curve is a lifetime, which was estimated equal to 265±4 ps, in good agreement with the value of the lifetime used in the event generator (263 ps). In summary, according to simulation-based estimates of the MPD detector efficiency for hypertritons and model predictions on (hyper)nuclei yields, about a 10^3 hypertritons can be registered in one week of data taking of Bi+Bi collisions at $\sqrt{s_{NN}}$ = 9.2 GeV with luminosity $L \approx 10^{25}$ cm^{-2}s^{-1}.

2.4. Azimuthal anisotropy

The sensitivity of the azimuthal anisotropic collective flow to the equation of state (EoS) and the transport properties of the strongly interacting matter makes it one of the promising observables in the relativistic heavy-ion experiments.

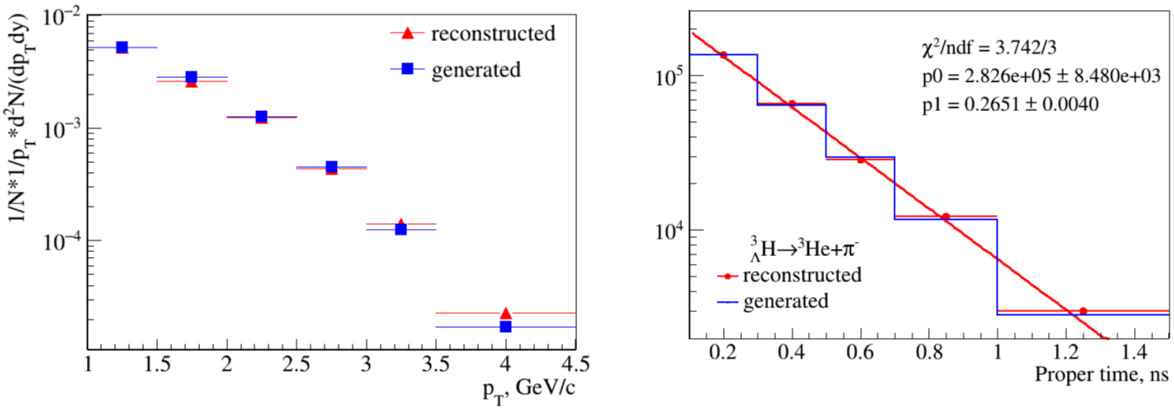

Fig. 5. Invariant yield distribution for hypertritons (left). Distribution of the number of hypertritons in intervals of proper time (right). Results are for Bi+Bi collisions at $\sqrt{s_{NN}}$ = 9.2 GeV.

Fig.6 shows comparison of the generated and reconstructed $v_2(p_T)$ and $v_1(y)$ signals for charged pions, kaons and protons in Bi+Bi collisions at $\sqrt{s_{NN}}$ = 9.2 GeV. Identification of the charged hadrons is based on a combination of momentum information, the specific energy loss (dE/dx) in the TPC and time-of-flight measurements from the TOF detector. The results were obtained using different analysis methods and the reconstructed signals are found to be consistent within uncertainties with the generated ones for all particle species and event centralities. For all particle species, the directed flow v_1 crosses zero at midrapidity. Different methods of flow measurements have different sensitivity to the flow fluctuations and to so-called non-flow correlations. They include the overall transverse momentum conservation, small angle azimuthal correlations due to final state interactions, resonance decays, mini-jet production, and quantum correlations due to the HBT effect.

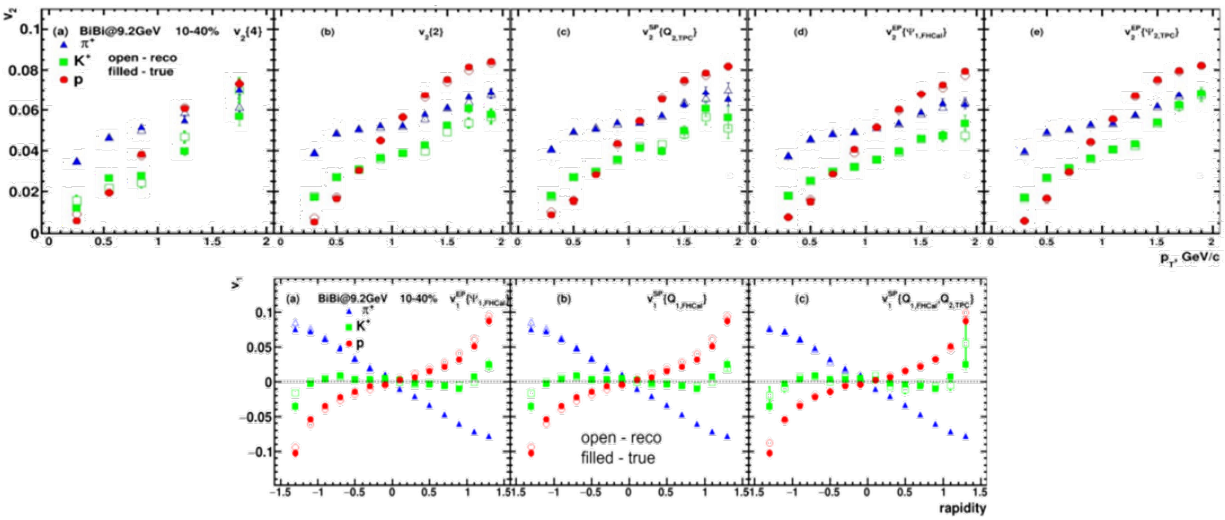

Fig. 6. Reconstructed and generated $v_2(p_T)$ and $v_1(y)$ signals for charged pions, kaons and protons in Bi+Bi collisions at $\sqrt{s_{NN}}$ = 9.2 GeV.

Similar studies have been performed for V0 particles such as Λ and K_s using the event plane and invariant mass fit methods. As in previous case, a very good agreement between the generated and reconstructed $v_2(p_T)$ and $v_1(y)$ signals was observed. Flow measurements have also been attempted for inclusive photons and neutral pions reconstructed in $\pi^0 \rightarrow \gamma\gamma$ decay channel using different methods for photon reconstruction revealing a good consistency between the reconstructed and generated signals. The studies performed confirm that MPD is well equipped to

perform v_1, v_2 and v_3 measurements for a wide variety of identified hadrons with the first collected datasets.

2.5. Dielectron continuum

Dielectrons provide possibility to measure the temperature of hot matter without blue shift, which appears due to radial expansion of the fireball. One can expect, that at NICA energies, the heavy flavor decay contribution will be negligible and thermal virtual photon emission will be the dominant source in the intermediate mass region 1-3 GeV/c^2. This will provide access to the temperature of hot source. Thermal photon emission will also appear in the low mass region, < 0.5 GeV/c^2, where one can relate virtual and real photon yield with Kroll-Wada formula and calculate real direct photon yield. Finally, the di-lepton invariant mass distribution is sensitive to the in-medium modifications of spectral function of ρ-meson.

The MPD is well suited for such measurements. Accurate tracking and electron identification with TPC, TOF and ECAL provide the means to reach ~ 45% efficiency of electron track reconstruction at ~ 100% purity of the signal at p_T > 200 MeV/c. This is achieved by the combined effect of the measurements of the average specific energy loss (dE/dx) of the track while traversing the TPC gas, the particle time-of-flight in the TOF and ECAL detectors, and the particle energy in the ECAL. The latter contributes to the electron identification and hadron rejection by requiring the energy over momentum E/p ratio of the particle to be unity. Tight matching of the reconstructed tracks to the primary vertex also removes nearly 98% of conversion electrons produced beyond the beam pipe.

The main challenge for dielectron measurements is huge combinatorial background resulting from electrons produced in Dalitz decays of neutral mesons. A novel pair analysis strategy was developed. To enhance the chances of recognizing electrons originating from π^0-Dalitz and gamma conversions, the rapidity phase space of fully reconstructed electrons is divided into a fiducial ($|\eta| < 0.7$) and a veto ($0.7 < \eta < 1.0$) region. In addition, the total electron sample is categorized in three different sub-samples or pools. Pool-1 includes the fully reconstructed electron tracks within the fiducial acceptance area, $|\eta| < 0.7$ whereas Pool-2 contains the fully reconstructed electron tracks within the veto acceptance area $0.7 < \eta < 1.0$. Pool-3 contains partially reconstructed electron tracks, i.e. electrons reconstructed in the TPC, and not identified at least in one the outer detectors, the TOF or ECAL. The analysis procedure consists of three steps. In the first step, tracks belonging to Pool-1 in a given event are paired with oppositely charged tracks in the same event from Pool-1 and Pool-2. Pairs with invariant mass smaller than 120 MeV/c^2 are tagged as pairs from π^0 Dalitz or conversions and not used for further pairing. In the second step, the remaining tracks from Pool-1 are paired with oppositely charged tracks from Pool-3 in the same event and both tracks are removed as a potential Dalitz pair if they have mass less than 80 MeV/c^2 and opening angle (θ) smaller than 5 or 10 degrees. In the third step, the remaining tracks from Pool-1 with p_T > 200 MeV/c are paired among themselves to build the unlike sign invariant mass spectra. The accumulated invariant mass distribution along with combinatorial background estimated using like-sign pairs is shown in Fig.7. A signal-to-background ratio of about 6% is observed over the integrated mass range of 0.2-1.5 GeV/c^2, which is a factor of two improvement over the previous results.

In summary, the MPD experiment demonstrates a strong capability for comprehensive dielectron measurements, benefiting from excellent electron identification and high electron purity, particularly due to the critical role of the ECAL in reducing the hadronic contamination.

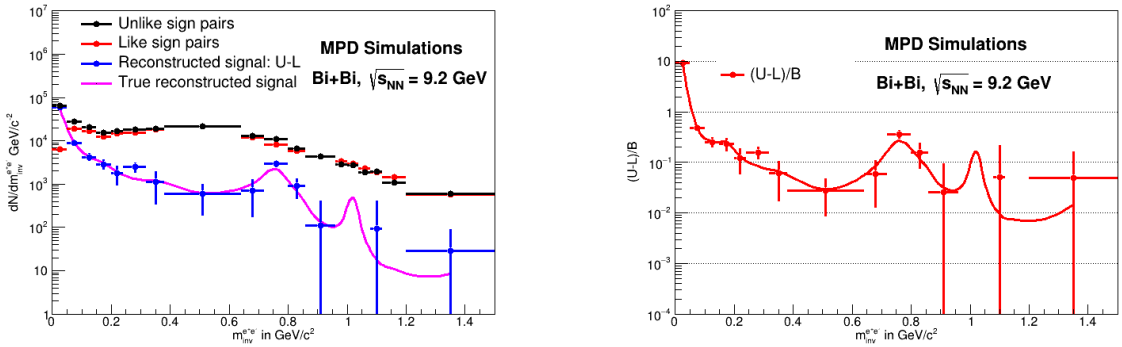

Fig. 7. The dielectron continuum and combinatorial background estimated with like-sign pairs (left) and the signal-to-background ratio (right) in Bi+Bi collisions at $\sqrt{s_{NN}}$ = 9.2 GeV.

2.6. Other main results

The following main results of physics feasibility studies were obtained in 2020-2024:

1. Determination of efficiency of the MPD trigger system (FFD, FHCAL and TOF) for selection of A-A collisions at $\sqrt{s_{NN}}$ = 4-11 GeV as a function of event centrality and event vertex.
2. Determination of event centrality in heavy-ion collisions using signals from the TPC, ECAL and FHCAL, estimation of biases for different physics observables.
3. Measurement of event geometry (event plane) suing different detector subsystems (FFD, FHCAL, TPC) and analysis methods.
4. Determination of collision geometry using Glauber model and Γ-fit method.
5. Comparative analysis of different models and event generators to identify those, which provide most realistic signal estimates for A-A collisions at NICA energies.
6. Measurement of hyperon global polarization in Bi+Bi collisions at $\sqrt{s_{NN}}$ = 9.2 GeV.
7. Estimation of direct photons yields in Au+Au collisions at $\sqrt{s_{NN}}$ = 4-11 GeV using model calculation and empirical scaling.
8. Study of two-pion correlation functions (HBT) with Gaussian and Levy shapes, charged balance function and factorial moments in A-A collisions at $\sqrt{s_{NN}}$ = 4-11 GeV.
9. Measurement of light nuclei production (d, t, ^{3}He) as a function of transverse momentum, rapidity and event centrality in Bi+Bi collisions at $\sqrt{s_{NN}}$ = 9.2 GeV.
10. Measurement of hadronic resonance production (ρ(770), K*(892), ϕ(1020), Λ(1520), Σ(1385)) as a function of transverse momentum and event centrality in A-A collisions at $\sqrt{s_{NN}}$ = 4-11 GeV.
11. Measurement of net-proton and net-kaon multiplicity distributions in search of fluctuation signals pointing to approaching to Critical End-Point in Au+Au collisions at $\sqrt{s_{NN}}$ = 4-11 GeV.
12. Measurement of charmed D and D_s-mesons in pp and A-A collisions at NICA energies using the future ITS detector.

Main References:

[1] Optimization of Techniques for Λ Hyperon Measurement at MPD/NICA
V. Kolesnikov (Dubna, JINR), D. Suvarieva (Dubna, JINR and Plovdiv U.), V. Vasendina (Dubna, JINR), A. Zinchenko (Dubna, JINR)
DOI: 10.1134/S106377962470028X
Published in: Phys.Part.Nucl. 55 (2024) 4, 827-831,
[2] Prospects of the MPD Detector for Measuring the Spectra of Identified Hadrons in ${\mathbf{Bi}} + {\mathbf{Bi}}$ Collisions at Energy $\sqrt {{{s}_{{NN}}}} = 9.2$ GeV
A. Mudrokh (Dubna, JINR)
DOI: 10.1134/S1063779624700291
Published in: Phys.Part.Nucl. 55 (2024) 4, 973-977,

[3] Anisotropic Flow Measurements of Identified Hadrons with Fixed-Target Mode of MPD Detector at NICA
P. Parfenov (Moscow Phys. Eng. Inst. and Moscow, INR), M. Mamaev (Moscow Phys. Eng. Inst. and Moscow, INR), A. Taranenko (Moscow Phys. Eng. Inst. and Dubna, JINR)
DOI: 10.1134/S1063779624700369
Published in: Phys.Part.Nucl. 55 (2024) 4, 853-858,
[4] Prospects for Studying the Production of Hyperons and Hypernuclei in the MPD Experiment at the NICA Accelerator Complex
V.I. Kolesnikov (Dubna, JINR), V.A. Vasendina (Dubna, JINR), A.I. Zinchenko (Dubna, JINR)
DOI: 10.1134/S1063779624700205
Published in: Phys.Part.Nucl. 55 (2024) 4, 797-802,
[5] Initial physics performance and status of the MPD at NICA
MPD Collaboration • Ivonne Maldonado (Dubna, JINR) for the collaboration.
DOI: 10.1393/ncc/i2024-24238-1
Published in: Nuovo Cim.C 47 (2024) 4, 238
[6] Bayesian approach to particles identification in the MPD experiment
V.A. Babkin (Unlisted, RU), V.M. Baryshnikov (Unlisted, RU), M.G. Buryakov (Unlisted, RU), S.G. Buzin (Unlisted, RU), A.V. Dmitriev (Unlisted, RU) et al.
e-Print: 2406.12879 [physics.ins-det]
DOI: 10.1088/1748-0221/19/08/P08007
Published in: JINST 19 (2024) 08, P08007
[7] Performance study of the hyperon global polarization measurements with MPD at NICA
Elizaveta Nazarova (Dubna, JINR), Vadim Kolesnikov (Dubna, JINR), Petr Parfenov (Dubna, JINR and Moscow Phys. Eng. Inst.), Arkadiy Taranenko (Moscow Phys. Eng. Inst.), Oleg Teryaev (Dubna, JINR) et al.
DOI: 10.1140/epja/s10050-024-01308-4
Published in: Eur.Phys.J.A 60 (2024) 4, 85
[8] Study of bulk properties of the medium produced in heavy ion collisions at MPD
Anil Sharma (UGC-DAE CSR, Kolkata), Alexey Aparin (Dubna, JINR)
Published in: DAE Symp.Nucl.Phys. 67 (2024), 1027-1028
[9] Multilayer Perceptron Neural Model for Particle Identification in MPD
G. Tolkachev (Moscow Phys. Eng. Inst.), A. Korobitsin (Dubna, JINR), A. Aparin (Dubna, JINR)
DOI: 10.1134/S1063778823050381
Published in: Phys.Atom.Nucl. 86 (2023) 5, 845-849
[10] Machine Learning Application for Particle Identification in MPD
V. Papoyan (Dubna, JINR and Yerevan Phys. Inst. and Dubna Intl. Univ.), A. Aparin (Dubna, JINR), A. Ayriyan (Dubna, JINR and Yerevan Phys. Inst. and Dubna Intl. Univ. and Yerevan State U.), H. Grigorian (Dubna, JINR and Yerevan Phys. Inst. and Dubna Intl. Univ. and Yerevan State U.), A. Korobitsin (Dubna, JINR) et al.
DOI: 10.1134/S1063778823050332
Published in: Phys.Atom.Nucl. 86 (2023) 5, 869-873
[11] Prospects for Photon Conversion Measurements in the Future MPD Experiment at NICA
E. Kryshen (St. Petersburg, INP), N. Burmasov (St. Petersburg, INP), D. Ivanishchev (St. Petersburg, INP), D. Kotov (St. Petersburg, INP and St. Petersburg Polytechnic Inst.), M. Malaev (St. Petersburg, INP) et al.
DOI: 10.1134/S1063779623040226
Published in: Phys.Part.Nucl. 54 (2023) 4, 613-618,
[12] Searching for the Baryon-to-Meson Transition Region with the MPD at NICA

Alejandro Ayala (Mexico U., ICN and Cape Town U. and Santa Maria U., Brazil), Wolfgang Bietenholz (Mexico U., ICN), Eleazar Cuautle (Mexico U., ICN), Rodrigo GarcÃ¬a FormentÃ¬ (Mexico U., ICN), Rodrigo GuzmÃ¡n (Mexico U., ICN)
e-Print: 2305.02455 [hep-ph]
DOI: 10.1134/S1063778823050071
Published in: Phys.Atom.Nucl. 86 (2023) 5, 901-907
[13] A Monte Carlo Study of Hyperon Production with the MPD and BM@N Experiments at NICA
Alexander Zinchenko (LHEP JINR, Dubna), Mikhail Kapishin (LHEP JINR, Dubna), Viktar Kireyeu (LHEP JINR, Dubna), Vadim Kolesnikov (LHEP JINR, Dubna), Alexander Mudrokh (LHEP JINR, Dubna) et al.
DOI: 10.3390/particles6020027
Published in: Particles 6 (2023) 2, 485-496
[14] Centrality Determination in MPD at NICA
MPD Collaboration • A. Aparin (Dubna, JINR) et al.
DOI: 10.1134/S1547477122050065 , 10.1134/s1547477122050065
Published in: Phys.Part.Nucl.Lett. 19 (2022) 5, 489-492
[15] Study of Material Budget of the MPD Detectors
D. Myktybekov (Dubna, JINR and IPT, Kazakstan and Al Farabi Kazakh Natl. U.), O. Rogachevsky (Dubna, JINR), S. Sabyr (Dubna, JINR and IPT, Kazakstan)
DOI: 10.1134/S1547477122050314
Published in: Phys.Part.Nucl.Lett. 19 (2022) 5, 497-500
[16] Hadronic resonances in heavy-ion collisions at NICA energies and their reconstruction in the MPD setup
Victor Riabov (St. Petersburg, INP and Moscow Phys. Eng. Inst.)
DOI: 10.1142/S0217751X22440031
Published in: Int.J.Mod.Phys.A 37 (2022) 34, 2244003
[17] Centrality Determination in Heavy-Ion Collisions with MPD Detector at NICA
MPD Collaboration • Dim Idrisov (Moscow Phys. Eng. Inst.) for the collaboration.
DOI: 10.3103/S0027134922020424
Published in: Moscow Univ.Phys.Bull. 77 (2022) 2, 206-207
[18] Anisotropic Flow Measurements in MPD Experiment Using Two- and Three-Particle Correlation Scalar Product Method
Petr Parfenov (Moscow Phys. Eng. Inst.)
DOI: 10.3103/S002713492202076X
Published in: Moscow Univ.Phys.Bull. 77 (2022) 2, 245-246
[19] Short-Lived Resonances in the Physical Program of the MPD Experiment at NICA
D.A. Ivanishchev (St. Petersburg, INP), D.O. Kotov (St. Petersburg, INP), M.V. Malaev (St. Petersburg, INP), V.G. Ryabov (St. Petersburg, INP and Moscow Phys. Eng. Inst.), Yu. G. Ryabov (St. Petersburg, INP)
DOI: 10.1134/S1063779622020368
Published in: Phys.Part.Nucl. 53 (2022) 2, 347-353, Phys.Part.Nucl. 53 (2022) 2, 347-353
[20] Performance of the MPD Detector in the Study of Strangeness Production and Event-by-Event Fluctuations in Au + Au Collisions at NICA
A. Mudrokh (Dubna, JINR), V. Kolesnikov (Dubna, JINR)
DOI: 10.1134/S1063779622020599
Published in: Phys.Part.Nucl. 53 (2022) 2, 292-296, Phys.Part.Nucl. 53 (2022) 2, 292-296
[21] Performance of the MPD Detector for the Study of Strongly-Intensive Multiplicity and Transverse Momentum Fluctuations in Heavy-Ion Collisions

E. Andronov (St. Petersburg State U.), I. Altsybeev (St. Petersburg State U.), D. Prokhorova (St. Petersburg State U.)
DOI: 10.1134/S1063779622020095
Published in: Phys.Part.Nucl. 53 (2022) 2, 122-126, Phys.Part.Nucl. 53 (2022) 2, 122-126
[22] Perspectives of Strangeness Study at NICA/MPD from Realistic Monte Carlo Simulation
J. Drnoyan (Dubna, JINR), V. Kolesnikov (Dubna, JINR), A. Mudrokh (Dubna, JINR), V. Vasendina (Dubna, JINR), A. Zinchenko (Dubna, JINR)
DOI: 10.1134/S1063779622020307
Published in: Phys.Part.Nucl. 53 (2022) 2, 203-206, Phys.Part.Nucl. 53 (2022) 2, 203-206
[23] Generative Adversarial Networks for the fast simulation of the Time Projection Chamber responses at the MPD detector
A. Maevskiy (Higher Sch. of Economics, Moscow), F. Ratnikov (Higher Sch. of Economics, Moscow and Yandex Sch. Data Anal., Moscow), A. Zinchenko (Dubna, JINR), V. Riabov (St. Petersburg, INP), A. Sukhorosov (Higher Sch. of Economics, Moscow) et al.
e-Print: 2203.16355 [physics.ins-det]
DOI: 10.1088/1742-6596/2438/1/012087
Published in: J.Phys.Conf.Ser. 2438 (2023) 1, 012087,
[24] Status and initial physics performance studies of the MPD experiment at NICA
MPD Collaboration • V. Abgaryan (Yerevan Phys. Inst. and Dubna, JINR) et al.
e-Print: 2202.08970 [physics.ins-det]
DOI: 10.1140/epja/s10050-022-00750-6
Published in: Eur.Phys.J.A 58 (2022) 7, 140
[25] Monte Carlo Studies of the MPD Detector Performance for the Measurement of Hypertritons in Heavy-Ion Collisions at NICA Energies
V.I. Kolesnikov (Dubna, JINR), V.A. Kireyeu (Dubna, JINR), A.A. Mudrokh (Dubna, JINR), V.A. Vasendina (Dubna, JINR), A.I. Zinchenko (Dubna, JINR) et al.
DOI: 10.1134/S1547477122010071
Published in: Phys.Part.Nucl.Lett. 19 (2022) 1, 46-53
[26] The NICA Complex and the MPD experiment at JINR: status and physics potential
Adam Kisiel (Dubna, JINR and Warsaw U. of Tech.)
DOI: 10.1051/epjconf/202225909002
Published in: EPJ Web Conf. 259 (2022), 09002
[27] MPD Prospects for the Study of Hadron and (hyper)nuclei Production at NICA Energies
MPD Collaboration • A. Mudrokh (Dubna, JINR) et al.
DOI: 10.1134/S1063778823010386
Published in: Phys.Atom.Nucl. 85 (2022) 6, 1007-1010
[28] Detailed Study of the MPD Detector Performance for Reconstruction of Hyperons in Heavy-Ion Collisions at NICA Energies
J.R. Drnoyan (Dubna, JINR), V.I. Kolesnikov (Dubna, JINR), E.A. Levterova (Dubna, JINR), A.A. Mudrokh (Dubna, JINR), V.A. Vasendina (Dubna, JINR) et al.
DOI: 10.1134/S1547477121060042
Published in: Phys.Part.Nucl.Lett. 18 (2021) 6, 676-686
[29] Thermal Photon and Neutral Meson Measurements Using the Photon Conversion Method in the MPD Experiment at the NICA Collider
MPD Collaboration • E. Kryshen (St. Petersburg, INP) et al.
DOI: 10.1134/S1063779621040390
Published in: Phys.Part.Nucl. 52 (2021) 4, 669-674
[30] Study of Production Features, Modeling and Optimization of Algorithms for Reconstruction of Short-Lived Hadron Resonances in the MPD Experimental Setup at the NICA Collider
MPD Collaboration • D. Ivanishchev (St. Petersburg, INP) et al.

DOI: 10.1134/S1063779621040286
Published in: Phys.Part.Nucl. 52 (2021) 4, 703-709,
[31] Performance for Directed Flow Measurements of the MPD Experiment at NICA Collider
MPD Collaboration • P. Parfenov (Moscow Phys. Eng. Inst.) et al.
DOI: 10.1134/S106377962104047X
Published in: Phys.Part.Nucl. 52 (2021) 4, 618-623,
[32] Methods for Elliptic Flow Measurements with the MPD Experiment at NICA
D. Idrisov (Moscow Phys. Eng. Inst.), V.B. Luong (Moscow Phys. Eng. Inst.), N. Geraksiev (Plovdiv U. and Dubna, JINR), A. Demanov (Moscow Phys. Eng. Inst.), P. Parfenov (Moscow Phys. Eng. Inst.) et al.
DOI: 10.1134/S1063779621040274
Published in: Phys.Part.Nucl. 52 (2021) 4, 637-643,
[33] Measurements of Spectators with Forward Hadron Calorimeter in MPD/NICA Experiment
A. Ivashkin (Moscow, INR), M. Golubeva (Moscow, INR), F. Guber (Moscow, INR and Moscow, MIPT), N. Karpushkin (Moscow, INR), S. Morozov (Moscow, INR and Moscow Phys. Eng. Inst.) et al.
DOI: 10.1134/S1063779621040298
Published in: Phys.Part.Nucl. 52 (2021) 4, 578-583,
[34] Feasibility Study for the Net-Proton and Net-Kaon Event-by-Event Fluctuations Measurements with the MPD Detector
MPD Collaboration • A. Mudrokh (Dubna, JINR) et al.
DOI: 10.1134/S1063779621040432
Published in: Phys.Part.Nucl. 52 (2021) 4, 644-647,
[35] Overview of the MPD Experiment
A. Kisiel (Warsaw U. of Tech. and Dubna, JINR)
DOI: 10.1134/S1063779621040328
Published in: Phys.Part.Nucl. 52 (2021) 4, 501-505,
[36] MPD Prospects for the Study of Strangeness Production at NICA Energies
V. Kolesnikov (Dubna, JINR), A. Mudrokh (Dubna, JINR)
DOI: 10.1134/S1063779621040341
Published in: Phys.Part.Nucl. 52 (2021) 4, 698-702,
[37] Event Reconstruction and Physics Signal Selection in the MPD Experiment at NICA
A. Zinchenko (Dubna, JINR), J. Drnoyan (Dubna, JINR), V. Kolesnikov (Dubna, JINR), A. Mudrokh (Dubna, JINR), I. Rufanov (Dubna, JINR) et al.
DOI: 10.1134/S1063779621040626
Published in: Phys.Part.Nucl. 52 (2021) 4, 691-697,
[38] Factorial Moments in the NICA/MPD Experiment
O. Kodolova (SINP, Moscow), M. Cheremnova (SINP, Moscow), I. Lokhtin (SINP, Moscow), A. Chernyshov (SINP, Moscow), L. Malinina (SINP, Moscow and Dubna, JINR) et al.
DOI: 10.1134/S106377962104033X
Published in: Phys.Part.Nucl. 52 (2021) 4, 658-662,
[39] Electron Identification from $dE{\text{/}}dx$ Measurements in the MPD TPC
I. Rufanov (Dubna, JINR), A. Zinchenko (Dubna, JINR)
DOI: 10.1134/S1063779621040535
Published in: Phys.Part.Nucl. 52 (2021) 4, 783-787,
[40] Development of a Vector Finder Toolkit for Track Reconstruction in MPD ITS
D. Zinchenko (Dubna, JINR), A. Zinchenko (Dubna, JINR), E. Nikonov (Dubna, JINR)
DOI: 10.1134/S106377962104064X
Published in: Phys.Part.Nucl. 52 (2021) 4, 788-792
[41] Evaluation of Prospects for Hypernuclei Studies with MPD at NICA

J. Drnoyan (Dubna, JINR), V. Kolesnikov (Dubna, JINR), A. Mudrokh (Dubna, JINR), I. Rufanov (Dubna, JINR), V. Vasendina (Dubna, JINR) et al.
DOI: 10.1134/S1063779621040249
Published in: Phys.Part.Nucl. 52 (2021) 4, 720-724
[42] Monte Carlo Study of Λ Polarization at MPD
E. Nazarova (Dubna, JINR), R. Akhat (Dubna, JINR and IPT, Kazakstan), M. Baznat (Dubna, JINR and IAP, Chisinau), O. Teryaev (Dubna, JINR), A. Zinchenko (Dubna, JINR)
DOI: 10.1134/S1547477121040142
Published in: Phys.Part.Nucl.Lett. 18 (2021) 4, 429-438
[43] Application of FHCal for Heavy-Ion Collision Centrality Determination in MPD/NICA Experiment
Vadim Volkov (Moscow, INR and Moscow, MIPT), Marina Golubeva (Moscow, INR), Fedor Guber (Moscow, INR and Moscow, MIPT), Alexander Ivashkin (Moscow, INR and Moscow, MIPT), Nikolay Karpushkin (Moscow, INR and Moscow, MIPT) et al.
DOI: 10.3390/particles4020022
Published in: Particles 4 (2021) 2, 236-240
[44] Techniques for Reconstruction of Strange Objects at MPD
Alexander Zinchenko (Dubna, JINR)
DOI: 10.3390/particles4020016
Published in: Particles 4 (2021) 2, 178-185
[45] Production and reconstruction of short-lived resonances in heavy-ion collisions at NICA energies using the MPD detector
MPD Collaboration • Victor Riabov (St. Petersburg, INP and Moscow Phys. Eng. Inst.) for the collaboration.
DOI: 10.1088/1402-4896/abf212
Published in: Phys.Scripta 96 (2021) 6, 064002
[46] Anisotropic Flow Measurements of Identified Hadrons with MPD Detector at NICA
Petr Parfenov (Moscow Phys. Eng. Inst.), Dim Idrisov (Moscow Phys. Eng. Inst.), Vinh Ba Luong (Moscow Phys. Eng. Inst.), Nikolay Geraksiev (Plovdiv U. and Dubna, JINR), Anton Truttse (Moscow Phys. Eng. Inst.) et al.
DOI: 10.3390/particles4020014
Published in: Particles 4 (2021) 2, 146-158
[47] Reconstruction of Photon Conversions in the MPD Experiment
MPD Collaboration • Evgeny Kryshen (St. Petersburg, INP) et al.
DOI: 10.3390/particles4010008
Published in: Particles 4 (2021) 1, 55-62
[48] Resonance Reconstruction in the MPD
Dmitry Ivanishchev (St. Petersburg, INP), Dmitry Kotov (St. Petersburg, INP), Mikhail Malaev (St. Petersburg, INP), Victor Riabov (St. Petersburg, INP and Moscow Phys. Eng. Inst.), Yury Ryabov (St. Petersburg, INP)
DOI: 10.3390/particles4010003
Published in: Particles 4 (2021) 1, 29-36
[49] The MPD Experiment and JINR: construction status and physics performance
MPD Collaboration • A. Kisiel (Dubna, JINR and Warsaw U. of Tech.) for the collaboration.
DOI: 10.1016/j.nuclphysa.2020.122006
Published in: Nucl.Phys.A 1005 (2021), 122006
[50] Performance of the MPD Detector for the Study of Multi-strange Baryon Production in Heavy-ion Collisions at the Nuclotron-based Ion Collider Facility (NICA)
MPD Collaboration • N. Geraksiev (Dubna, JINR and Plovdiv U.) et al.
DOI: 10.5506/APhysPolBSupp.14.529

Published in: Acta Physica Polonica B Proceedings Supplement 14 (2021) 3, 529-532
[51] Detection of \(D^+\)-meson Decays in the Tracking System of NICA-MPD
V. Kondratiev (St. Petersburg State U.), C. Ceballos (Dubna, JINR), S. Igolkin (St. Petersburg State U.), A. Kolozhvari (Dubna, JINR), Y. Murin (Dubna, JINR) et al.
DOI: 10.5506/APhysPolBSupp.14.497
Published in: Acta Physica Polonica B Proceedings Supplement 14 (2021) 3, 497-501
[52] Centrality Determination in Heavy-ion Collisions with MPD Detector at NICA
P. Parfenov (Moscow Phys. Eng. Inst.), I. Segal (Moscow Phys. Eng. Inst.), D. Idrisov (Moscow Phys. Eng. Inst.), V.B. Luong (Moscow Phys. Eng. Inst.), A. Taranenko (Moscow Phys. Eng. Inst.) et al.
DOI: 10.5506/APhysPolBSupp.14.503
Published in: Acta Physica Polonica B Proceedings Supplement 14 (2021) 3, 503-506
[53] Short-lived Resonances and Neutral Mesons in the Physical Program of the NICA-MPD
Victor Riabov (St. Petersburg, INP and Moscow Phys. Eng. Inst.)
DOI: 10.5506/APhysPolBSupp.14.491
Published in: Acta Physica Polonica B Proceedings Supplement 14 (2021) 3, 491-495
[54] Properties of rho(770), K*(892), phi(1020), Sigma(1385), Lambda(1520) and Xi (1530) resonances in heavy-ion collisions at a center of mass energy of and their reconstruction using the MPD detector at NICA
MPD Collaboration • D.A. Ivanishchev (St. Petersburg, INP) et al.
DOI: 10.1088/1742-6596/2103/1/012140
Published in: J.Phys.Conf.Ser. 2103 (2021) 1, 012140, J.Phys.Conf.Ser. 2103 (2021) 1, 012140
[55] Prospects for Measuring Short-Lived Resonances in the MPD Experiment on the NICA Accelerator
D.A. Ivanishchev (St. Petersburg, INP), D.O. Kotov (St. Petersburg, INP), M.V. Malaev (St. Petersburg, INP), V.G. Riabov (St. Petersburg, INP and IITP, Moscow and Lebedev Inst. and Moscow Phys. Eng. Inst. and Moscow, ITEP), Yu. G. Ryabov (St. Petersburg, INP)
DOI: 10.3103/S1062873821120078
Published in: Bull.Russ.Acad.Sci.Phys. 85 (2021) 12, 1439-1444, Izv.Ross.Akad.Nauk Ser.Fiz. 85 (2021) 12, 1800-1806
[56] Perspectives of Neutral Meson Measurements in the MPD Experiment at NICA
Dmitry Ivanishchev (St. Petersburg, INP), Evgeny Kryshen (St. Petersburg, INP), Dmitry Kotov (St. Petersburg, INP and St. Petersburg Polytechnic Inst.), Mikhail Malaev (St. Petersburg, INP), Victor Riabov (St. Petersburg, INP and Moscow Phys. Eng. Inst.) et al.
DOI: 10.1142/9789811233913_0063
Published in:
[57] Study of Φ(1020) and K*(892) Meson Production in Heavy-ion Collision at NICA-MPD
Dmitry Ivanishchev (St. Petersburg, INP), Dmitry Kotov (St. Petersburg, INP), Mikhail Malaev (St. Petersburg, INP), Victor Riabov (St. Petersburg, INP and Moscow Phys. Eng. Inst.), Yuriy Riabov (St. Petersburg, INP)
DOI: 10.1142/9789811233913_0061
Published in:
[58] Simulating the time projection chamber responses at the MPD detector using generative adversarial networks
A. Maevskiy (Higher Sch. of Economics, Moscow), F. Ratnikov (Higher Sch. of Economics, Moscow and Yandex Sch. Data Anal., Moscow), A. Zinchenko (Dubna, JINR), V. Riabov (St. Petersburg, INP)
e-Print: 2012.04595 [physics.ins-det]
DOI: 10.1140/epjc/s10052-021-09366-4
Published in: Eur.Phys.J.C 81 (2021) 7, 599

[59] Hyperons from Bi + Bi Collisions at MPD-NICA: Preliminary Analysis of Production at Generation, Simulation and Reconstruction Level
Alejandro Ayala (Mexico U., ICN and U. Cape Town (main)), Eleazar Cuautle (Mexico U., ICN), Isabel DomÃ¬nguez (Sinaloa U.), M. RodrÃ¬guez-Cahuantzi (Puebla U., Mexico), Ivonne Maldonado (Sinaloa U.) et al.
e-Print: 2010.12593 [hep-ex]
DOI: 10.1134/S1063779621040092
Published in: Phys.Part.Nucl. 52 (2021) 4, 730-736
[60] Multipurpose Detector MPD for the Study of Strongly Interacting Matter at the NICA Collider
V.I. Kolesnikov (Dubna, JINR), A.A. Mudrokh (Dubna, JINR)
DOI: 10.1134/S1063778820090136
Published in: Phys.Atom.Nucl. 83 (2020) 9, 1363-1368

3. MPD detector

3.1 Introduction

The project "Multipurpose detector MPD for studying the properties of hot and dense baryon matter at the collider complex NICA" is devoted to a detailed exploration of the QCD phase diagram and search for the signals of deconfinement phase transition and the critical endpoint [1]. Comprehensive investigations in the unexplored region of the phase diagram of strongly interacting matter will be performed by a careful energy and system-size scan with ion species ranging from protons to Au^{79+} over the energy range $4 < \sqrt{s_{NN}} < 11$ GeV.

The goal of the Project is to design and build a multifunctional detector to measure heavy-ion collisions and investigate the basic Quantum Chromo Dynamics structure of matter. A vast research program in heavy-ion collisions (HIC) has been carried out over last 20 years and a number of new phenomena were discovered. There is strong evidence for a deconfinement phase transition in central HIC at low SPS energies [2]. Extensive experimental data collected by the RHIC experiments [3] suggest formation of a new state of dense partonic matter - strongly interacting Quark-Gluon Plasma (sQGP). However, it is commonly believed that a next generation of heavy ion experiments is required for much more sensitive and detailed study of the QCD phase diagram in the region of large baryochemical potential μ_B [4]. Several accelerator centers have recently started new programs with heavy ions: SPS at CERN [5], RHIC at BNL[6] and CBM at FAIR [7] may be considered as complementary programs aimed at the study of relevant physics problems of hot and dense baryonic matter.

The main advantages of the NICA/MPD project is that the NICA accelerator facility will provide a vast choice of beams (from protons to gold ions) in the energy range which brackets onset of deconfinement (center-of-mass energy from 4 to 11 GeV). A high luminosity of NICA ($L = 10^{27} cm^{-2} s^{-1}$) allows small enough energy steps and provide high interaction rate. The key feature of the proposed MPD detector design that allows studying of nuclear collisions with high precision are:

- High event rate (up to 6 KHz) allows very subtle measurements of the energy and centrality dependence of any phenomenon under interest
- MPD has full azimuthal coverage and will measure most of the momentum range in the pseudo-rapidity interval $-2 < \eta < 2$.
- Tracking and particle identification system including TPC for energy loss and TOF for time-of-flight measurements complemented by an electromagnetic calorimeter for photons and electrons with good time and energy resolution.

The first MPD concept was presented in Letter of Intent issued in February 2008, and the first version of the Conceptual Design Project was issued in December 2009 [8].

The existing international collaboration aimed in the Project realization consists of about 450 scientists from 16 Institutions from Russia and abroad. This document is organized as follows. The main physics goals of the MPD experiment are summarized in the previous Section. In Section 3, a general concept of the MPD detector is presented and the main components of MPD are described in some details. In the previous section the results of detector performance studies are presented. The document concludes with table for the cost estimate and the construction schedule.

The MPD apparatus has been designed as a 4π spectrometer capable for identifying charged hadrons, electrons and photons in heavy-ion collisions in the energy range of the NICA collider and measuring their momenta. To reach this goal, the detector will comprise a precise 3-D tracking system and a high-performance particle identification (PID) system based on the time-of-flight measurements and calorimetry. The basic design parameters have been determined by physics processes in nuclear collisions at NICA and by several technical constrains guided by a trade-of of efficient tracking and PID against a reasonable material budget. At the design luminosity, the event rate in the MPD interaction region is about 6 kHz; the total charged particle multiplicity exceeds 1000 in the most central Au+Au collisions at $\sqrt{s_{NN}}$ = 11 GeV. As the average transverse momentum of the particles produced in a collision at NICA energies is below 500 MeV/c, the detector design requires a very low material budget. The general layout of the MPD apparatus is shown in Fig.3.1.1. The whole detector setup covering ±2 units in pseudorapidity (η).

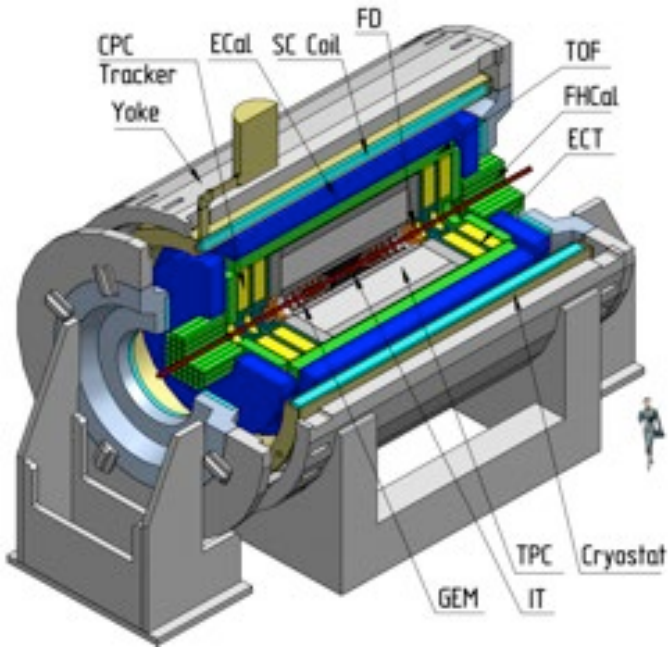

Fig. 3.1.1: Full Configuration of the MPD consists of Magnet Yoke (Yoke) and Solenoid (SC Coil), Time Projection Chamber (TPC), Time of Flight System (TOF), Fast Forward Detector (FFD), Forward hadron Calorimeter (FHCal), Forward Tracker (CPC and ECT) and Inner tracker System (IT)

As soon as construction of such detector requires long period of time, large group of physicists, engineers and technicians and large funds there was decision to build it in two stages.

The aim of this Project is to build the first stage of the MPD setup (Fig.3.1.2), which consists of the Magnet based on superconducting solenoid, Time-Projection Chamber (TPC), barrel Time-Of-Flight (TOF), Electromagnetic Calorimeter (ECal), Forward Calorimeter (FHCal) and Fast Forward Detector (FD).

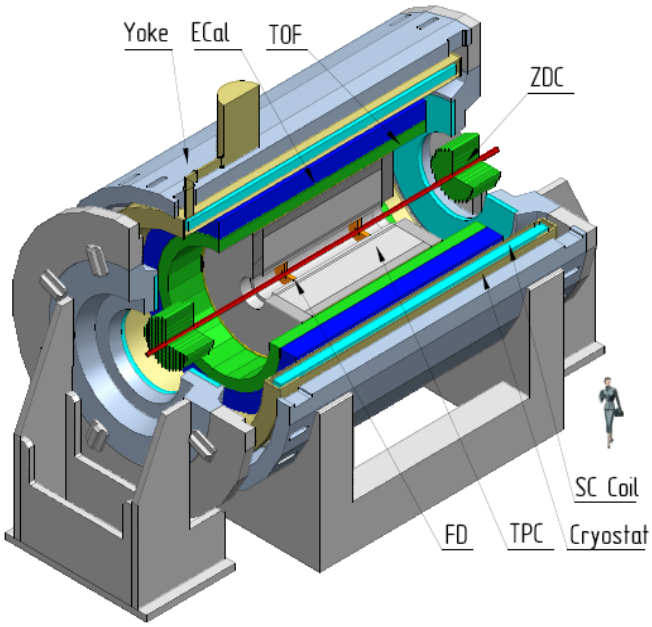

Fig. 3.1.2: The MPD setup in the first Stage. It consists of Magnet Yoke, Solenoid, Time Projection Chamber (TPC), Time of Flight detector (TOF), Electromagnetic Calorimeter (ECal), Fast Forward Detector (FFD) and Forward Hadron Calorimeter (FHCal)

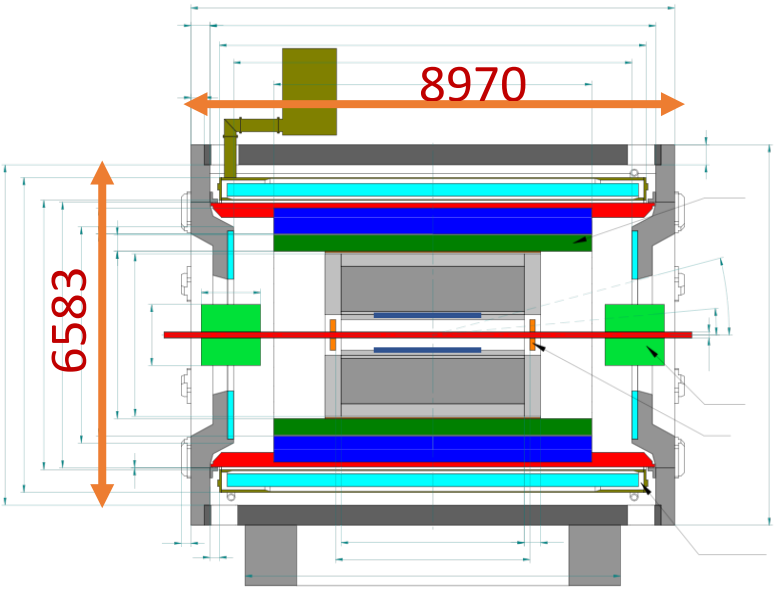

Fig. 3.1.3: Cutaway side view of the MPD in a basic Configuration with main dimensions.

The MPD is a 9 m long cylinder of about 6,6 m in diameter. The cross-sectional view of the MPD Detector in base configuration is shown in Fig. 3.1.3.

References

[1] A.N. Sissakian and A.S. Sorin, J. Phys. G: Nucl. Part. Phys. 36 (2009) 064069.

[2] C.Alt et al.Phys.Rev.C 77, 2008, 024903.

[3] Nucl.Phys. A757 (2005), 1-283

[4] Searching for a QCD mixed phase at the NICA (NICA White paper). Draft v2.01, 30 September 2009. http://nica.jinr.ru/

[5] NA61 experiment. CPOD07 (2007),023. Eprint - 0709.1646.

[6] G.S.F. Stephans, J. Phys., G32 (2006), S447-S454.

[7] P.Senger, J. Phys. G30 (2004), S1087-S1090.

[8] The MultiPurpose Detector (MPD). Conceptual Design Report, v1.0. http://nica.jinr.ru/

3.2 Superconducting magnet

The magnet of the MPD detector is intended to provide a homogeneous magnetic field with a rated value of magnetic field of 0.5 T inside its aperture. The required volume average inhomogeneity in the drift volume of TPC (of about 2.4 m in diameter and 3,4 m long) - Integral(Br/Bz)*dz≤ 1,5mm.

The superconducting magnet of MPD is intended for providing a highly homogeneous magnetic field of 0.57 T ensure the transverse momentum resolution within the range of 0.1–3 GeV/c at NICA. A constituent part of the MPD is a solenoid with a superconducting NbTi coil and a steel flux return yoke.

The MPD magnet consists of (Fig. 3.2.1):

- a cryostat with a superconducting coil and a control Dewar;
- a flux return yoke with two support rings, 28 bars, and two poles with trim coils;
- magnet support cradles;
- auxiliary platforms for moving the poles;
- roller skates for movement of the magnet and its poles.

In addition, there are power supplies for the superconducting solenoid and for the trim coils in the poles, a SC coil quenching protection system, a cryogenic system with the cryogenic pipeline, a vacuum system, helium refrigerator and a magnet control system.

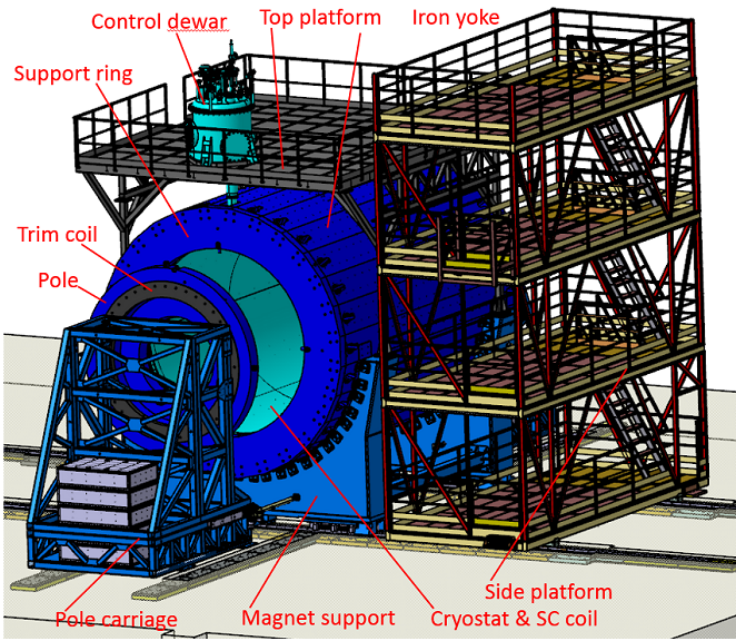

Fig. 3.2.1. Overall view of the magnet.

3.2.1 Assembly and preparation of the MPD solenoid magnet in 2021.

3.2.1.1. Unpacking the magnet (April 2021)

After the magnet arrived at JINR in 2020, it was unpacked in April 2021, as a result of which it was established:

- the shock sensors are in normal condition;

- the packaging is not damaged, there were no visible displacements of the solenoid from the lodgments;

- the upper flange of the outlet node for cryogenic pipelines and superconducting cable is missing (hereinafter referred to as the chimney node);

- the position of the cold mass was measured using reference points. The results obtained were compared with the results obtained at the ASG plant prior to transportation. The measurements and identified deviations when comparing the results presented in the S1-1 report were coordinated with ASG and are not critical.

- in accordance with the assembly qualification plan, a local electrical test was conducted for the integrity of the superconducting cable and the absence of its contact with the solenoid housing. The test was carried out at a voltage of 500V and 1000V. The test results were found to be positive.

3.2.1.2. Installation of a solenoid in a magnetic yoke (July 2021).

The next stage of the work was the installation of a solenoid in a magnetic yoke. To accurately position the solenoid relative to the magnetic yoke, it was necessary to coordinate the dimensions of the gaskets of the solenoid support brackets. The main difficulties were caused by 2 components:

- the solenoid brackets were welded with a deviation from the horizon, so high measurement accuracy, computer modeling of the position of the combined elements and further formation of the gasket profile were required;

- the different position of the coordinate axes used in JINR and at the ASG plant.

After carrying out these works and choosing a single coordinate system, the profile and size of the gaskets were agreed upon, and the solenoid was installed in the yoke of the magnet with permissible deviations that do not affect the formation of the magnetic field. The measurement results and the calculated deviation of the actual position of the solenoid axis relative to the yoke axis (taken as a base) and the signed report are shown in Figure 1.

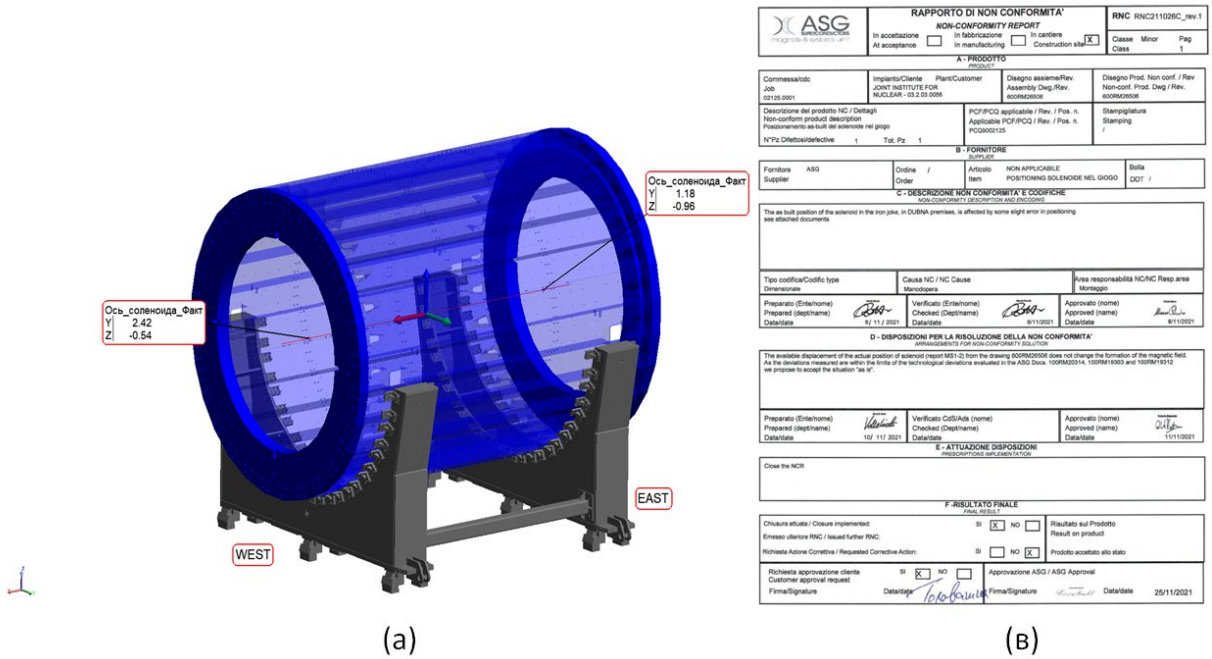

(a) (в)

Figure 1. The deviation of the actual position of the solenoid axis relative to the axis of the magnetic yoke (a) and the signed report (b).

3.2.1.3. Identified malfunctions as a result of local tests and their elimination (August – December 2021).

In accordance with the work plan for the assembly and testing of the solenoid, the sensors located inside the solenoid (temperature sensors, axial and radial displacement sensors, voltage drop sensors on a superconducting cable) were checked. As a result of the inspection, it was found that one of the F2AS1 connectors was out of order. The connector has been disassembled and repaired.

After repairing the connector, a standard vacuum system was assembled and connected to check the strength and tightness of the solenoid. The intermediate strength and tightness test included tests of the solenoid casing, the helium cooling circuit, and the nitrogen shield circuit. The testing was carried out according to the scheme agreed with ASG, by JINR specialists, with the participation of the ASG controller. As a result of the inspection, a leak of the nitrogen circuit was detected and localized. The detected leak was eliminated, and a re-check showed the complete tightness of the circuit.

3.2.2. Work on the assembly and commissioning of the magnet completed in 2022.

3.2.2.1. Development and assembly of the chimney node (February – July 2022).

The chimney node is the junction point of the control Dewar, inside which there is equipment and fittings (pipelines, a container of liquid helium, a place of input/output of a superconducting cable with a transition to a normal conduction cable, thermometry, valves, etc.) and a solenoid. This node includes 4 pipelines of the nitrogen shield circuit, 2 pipelines of the helium cooling circuit, and two plates of superconducting cable. These pipelines and cable are installed inside the vacuum casing. All elements of this node, according to the contract, had to be provided by the manufacturer ASG. Due to the fact that the terms of delivery of the completeness of this ASG node were not fulfilled, and communication was interrupted with ASG in February 2022, the JINR LHEP staff carried out work on the development and deep modernization of the node. In particular:

- it was decided to make a two-part vacuum casing. This allowed access to the main elements (bellows assemblies, superconducting cable, cryogenic supports, thermometry) without complete disassembly of the cryogenic part;

- the connection of cryogenic helium supply pipelines was made detachable in an accessible place;

- bellows units of their own design were used to prevent bending in case of increased pressure or changes in linear dimensions due to warming/cooling;

- the upper flange of the assembly, cut off in ASG, has been restored (Figure 2);

- local strength and tightness checks have been carried out;

- the upper beam of the magnetic circuit has been modified for local access to the elements of the chimney node.

All elements of the chimney assembly were manufactured, installed and tested. According to the results of local tests, all nodes are in working, satisfactory condition, there are no leaks. The new configuration of the modified beam was modeled to influence the uniformity of the magnetic field. According to the results of calculations, the modified beam does not significantly change the uniformity of the magnetic field in the volume of the solenoid.

Figure 2. Preparation of the chimney node by JINR specialists

3.2.2.2. Final assembly of the magnetic yoke, installation of a cryogenic platform and placement of equipment on it (July – August 2022).

The readiness of the chimney unit made it possible to complete the assembly of the magnetic circuit and install a cryogenic platform, begin placing equipment and testing it (Figure 3). It was carried out:

- installation of the support rings of the magnetic circuit;

- installation of magnetic yoke beams;

- measurements of the position of the magnetic yoke and support rings were carried out;

- installation of a cryogenic platform with the placement of a power supply and discharge system for the solenoid, a cooling system for the solenoid;

- solenoid monitoring and control systems.

Figure 3. Placement of solenoid engineering systems on a cryogenic platform.

3.2.2.3. Assembly and installation of solenoid correction coils on the slipway (July 2022).

The solenoid correction coils were manufactured and delivered to JINR in 2020. The coils are installed in poles with a tolerance of at least 2 mm, installed in the support rings of the magnetic circuit and close the magnetic field of the solenoid at the ends. The coil is a cable laid in a spiral and cooled with distilled water at room temperature. The weight of each coil is 2 tons, and the assembly with the pole is more than 40 tons. At the same time, it is worth considering that the coils were stacked with terminals down during transportation, which contradicted the scheme of their installation presented by ASG. In view of this, the staff of the MPD department and the LHEP Design Bureau developed a special traverse for turning the coil, with protection against spiral displacement and changing the shape of the coil when moving the flip. After mounting and installing the coils on the movable stocks, repeated (final) measurements of the coil–pole alignment was carried out. According to the measurement results, the position of the coil in the horizontal position, the alignment deviation was: for the TRIM1 coil – 1.3 mm, for the TRIM 2 coil – 0.47 mm with an acceptable deviation of 2 mm (Figure 3).

(а) (в)

Figure 3. Assembly of correction coils, where (a) is the coil-pole assembly, and (b) is the alignment measurement.

3.2.2.4. Preparation of the cryogenic solenoid system (July – December 2022).

The cryogenic solenoid system must ensure reliable operation and cooling of the superconducting cable up to 4.5 K. The main elements of the system are:

- Control Dewar;

- satellite refrigerator;

- nitrogen temperature maintenance system in cooling mode (NTSS);

- helium and nitrogen storage and delivery tanks;

- pipeline system and distribution of helium and nitrogen between consumers;

- a system of direct and reverse flow of technical gases (helium, nitrogen, air) including a reverse flow heating system.

The main difficulty of assembling these systems was that some of the performers (manufacturers ASG, ILK, Ferox, AS Scientific, etc.), citing force majeure, refused to perform their duties on the assembly and commissioning of this equipment. In view of this, in July 2022, it was decided by JINR employees to assemble and adjust the existing equipment, and place part of the orders, taking into account changes in the cooling scheme, at enterprises of the Russian Federation. Thus, the following works were performed:

- the assembly and testing of the refrigerator have begun, which was delivered in disassembled condition (Figure 4);

- a control Dewar is installed at the workplace and its connection to the solenoid is carried out;

- the algorithm of operation of the MFS nitrogen temperature maintenance system has been tested and adjusted;

- the cooling circuit of the solenoid has been redesigned taking into account changes in the infrastructure;

- orders have been placed for pipelines and reservoirs from manufacturers in the Russian Federation.

(а) (в)

Figure 4. Assembly of components of the cryogenic solenoid system, where (a) is the assembly of the refrigerator, (b) is the assembly and testing of the control Dewar.

3.2.3 Work on the assembly and commissioning of the magnet completed in 2023.

3.2.3.1 Preparation of the cryogenic system.

In 2023, work on the assembly of the refrigerator continued. As a result of the assembly and preparation of the refrigerator for operation, the absence of prepared software was revealed. The employees of the JINR LHEP and the company "Extended Range Systems" LLC carried out work on the development of a circuit and the preparation of new software with the ability to work in manual mode and telemetry visualization, based on existing PLCs. Due to the lack of calibration tables for low-temperature Cernox sensors, their restoration was not possible, and it was decided to manufacture and calibrate their own sensors by the LHEP. As a result, the satellite refrigerator is currently ready for manual operation and is integrated into the general cooling system of the solenoid.

Work continued on the assembly of cryogenic equipment on the technological platform. After installing the control Dewar on the platform and its local tests, it was connected to the solenoid

pipelines. The leads of a superconducting cable (SC) were mounted to the current leads. After electrical tests of the cable joint, it was filled with a compound. Additional temperature sensors were added to the SC cable, connecting it to the control Dewar (the most heat-loaded part), to determine the temperature of the cable during current input and stationary operation. After testing and isolating the pipelines and current leads, the control Dewar was hermetically sealed. At the same time, a vacuum pumping system of the solenoid cavity was installed and connected to the operating position. Sensors from the solenoid and vacuum system were connected to the Master control monitoring and control system (more than 500 cables). In May, the vacuum cavity of the solenoid was pumped out to a working vacuum of $5*10^{-5}$ Torr. The pumping time was 48 hours. The leakproofness tests were successful, no leaks were detected. During the tests, helium was supplied to the pipelines of the solenoid cooling system under operating pressures.

In the summer of 2023, the components of the MPD cryogenic solenoid cooling system re-ordered in the Russian Federation were received, all system elements were placed on the technological platform and the equipment was strapped with flexible cryogenic pipelines. The installation of warm pipelines for direct and reverse flows of helium and nitrogen of the semicircle “West” along the roof from the building 1B to the hall 101 (MPD hall) of the building 17 has been completed, with a total length of 500 m. In autumn, zip line suspensions were mounted, on which flexible pipelines are placed, allowing the magnet to be moved from the "assembly" position to the "bundle" position without warming the magnet and maintaining temperatures of 80K in any position of the magnet. Flexible and stationary pipelines have been tested for strength and tightness, including tests at cryogenic operating temperatures (Fig. 5).

Figure 5. General view of the technological platform, with the installed equipment.

Heaters were developed to heat the gaseous helium and nitrogen backflow, and the UK supplier AS Scientific refused to fulfill its obligations to manufacture them under the contract. In December 2022, a redesigned version of the heaters was re-ordered from Akkorod LLC of the

Russian Federation. In July, the heaters were delivered to JINR and in September 2023 they were mounted on and integrated into the general cooling system of the solenoid.

After assembling the cryogenic equipment, a trial cooling of the solenoid was carried out for 8 hours. This stage assumed the circulation of working gases in the cooling system circuits in a warm mode. At this stage of the work, the algorithms of the equipment operation were clarified, pressure parameters, valve position, the response of the software system to operator commands, checking the tightness of the system, working out interaction with the LHEP cryogenic department (NICO), as well as personnel actions were determined. The stage was completed on November 20, 2023. As a result of this work, it was determined that the cooling rate is 1.2 K/hour, and the difference does not exceed 7 K, which fits into the design parameters. During the 8-hour cooling, it was found out that by adjusting the helium flows in the refrigerator, it is possible to fairly accurately maintain the set cooling rate and the temperature of the outgoing flow into the solenoid.

3.2.3.2. The Master control monitoring, management and protection system.

In April 2023, the solenoid monitoring and control system was installed on the technological platform and its connection was started. Thanks to the contractors of “Extended Range Systems” LLC, it was possible to find passwords for logging into the system. It was updated, the electrical circuit was restored and the control signals were checked. Diagnostics showed that this system does not have an automatic mode, there is no connection “sensor–signal–command”, although it should be present according to the documentation. During the software debugging process, it was possible to fix a number of errors, update and add a number of calibration tables and links. Currently, the system can operate in manual mode and is ready for cryogenic tests. A voltage of 10 V and a current of 1.2 A were applied on the SC cable in test mode during the process of the software debugging. These data were recorded by the monitoring system on the “Voltage taps” tab (Fig. 6). Thus, at the moment, sensors of temperature, sensors of tension of suspension rods, current taps, control Dewar, vacuum system are correctly displayed in the system. Also, it is possible to control parameters in manual mode.

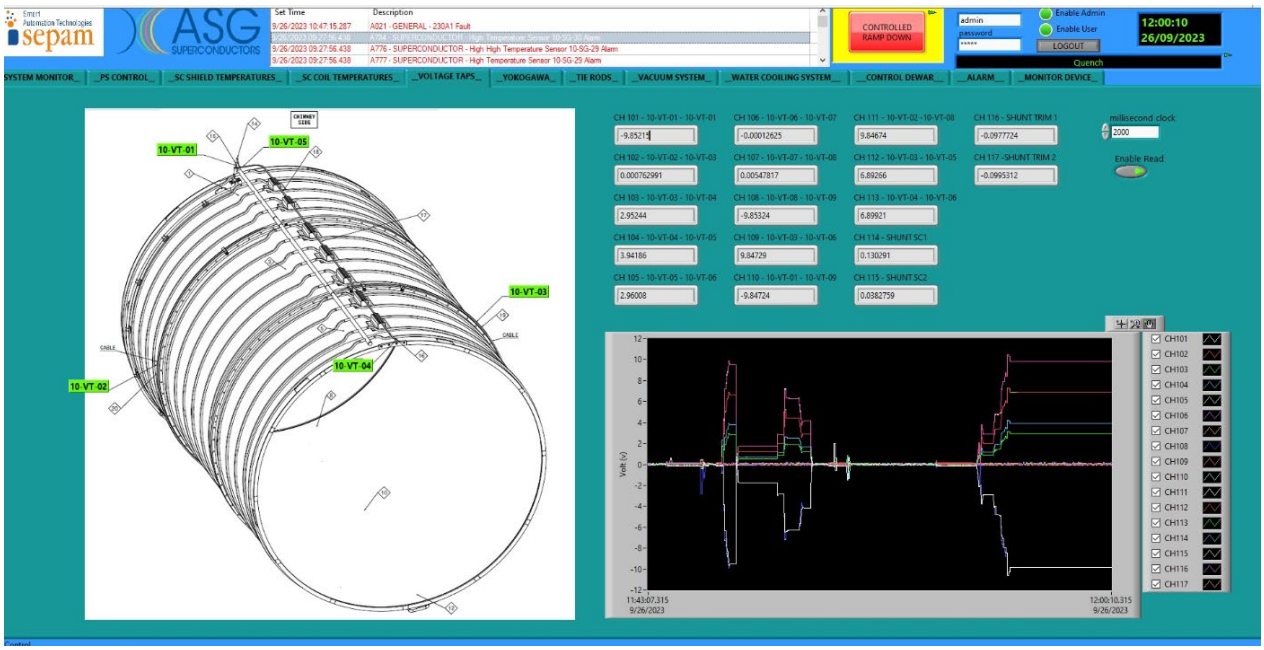

Figure 6. Testing the SC cable protection system.

3.2.4 Commissioning of the MPD magnet in 2024.

3.2.4.1. Cryogenic tests.

After the first stage of cryogenic tests in 2023, the cooling of the solenoid magnet to a temperature of 72 K was carried out in February - March 2024. As a result of the tests, the absence of cold leaks was established, cooling modes with a transition from nitrogen to helium were worked out, heat flows were determined, the operation mode of the solenoid without helium circulation under nitrogen screens was worked out, heating of the solenoid was carried out. The cooling schedule is shown in Figure 7.

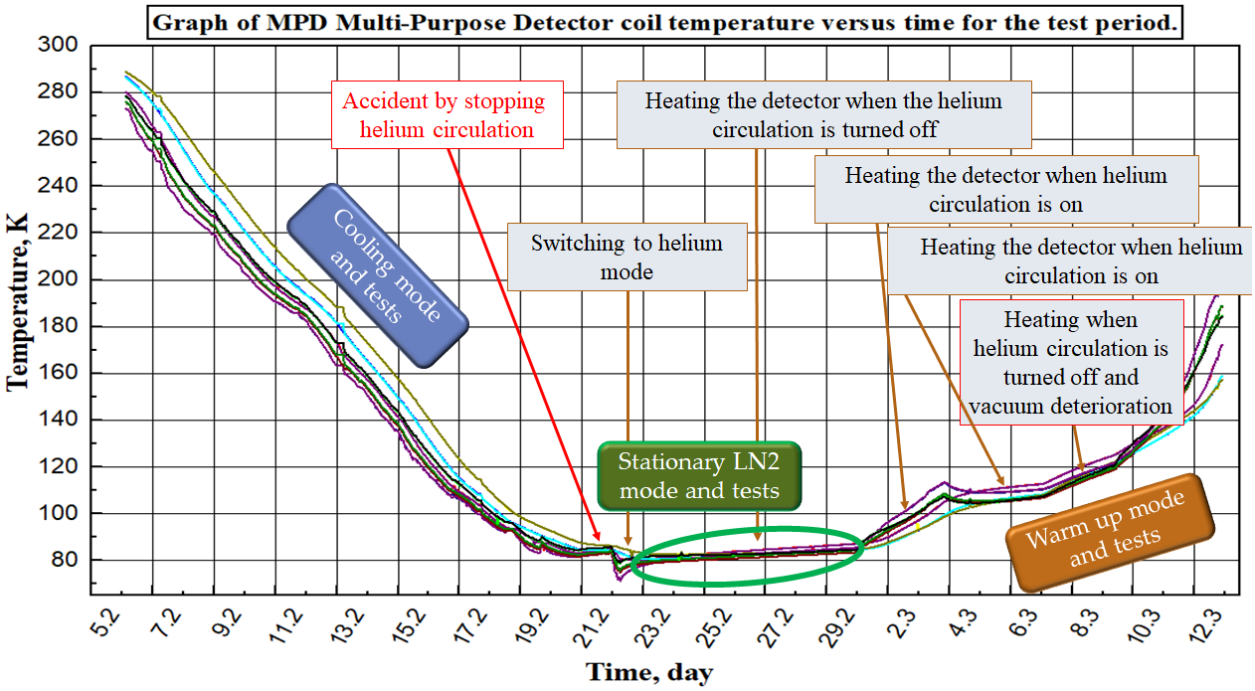

Figure 7. The cooling (warming) schedule of the solenoid in February – March 2024.

The graph shows that the cooling of the solenoid to a liquid nitrogen temperature of 77 K lasted 15 days. The average cooling rate was 0.6 K/h, which is significantly lower than the design 1-2 K/h. A lower cooling rate was chosen in order to study in detail the cooling process and the operation of the equipment. An experiment was also conducted on the transition from nitrogen cooling mode to helium, which showed a smooth transition without a significant increase in pressure. During the experiment, the operating mode on a nitrogen screen without circulation in a helium circuit was simulated. Such a mode is possible in the event of incidents, carrying out of planned preventive work on the NICA cryogenic complex or in the standby mode of the experiment on the beam (the expected hold of the magnet at a temperature of 80 K without warming). This experiment showed a total heat inflow to the system not more than 100 watts.

Also, during 2024, work was carried out to optimize the operation of technological equipment and local automation of systems. Work was carried out on the deep refinement of the refrigerator and pneumo-electric valves. The installation and testing of the main nitrogen pipeline were carried out, which allows combining the cryogenic magnet system and nitrogen tanks of 25 m^3. Thus, the main elements of the cryogenic system are assembled and ready to operate normally. There is a significant delay in the manufacture of the helium main pipeline. In this regard, a new temporary scheme has been developed for cooling the magnet to 4.5 K. Further work on measuring the magnetic field will also be carried out with a temporary pipeline for supplying liquid helium to the refrigerator. By the end of 2024, it is planned to reach the superconducting cable operating temperature of 4.5 K.

3.2.4.2 Magnet power supply systems.

From June to December 2024, work is underway on the placement and connection of power supplies for trim and SC coils. Currently, the power supply has been connected to the magnet and to the external discharge resistor (Fig.8). Testing of power supplies at the level of 10% of the nominal value begins. By the end of the year 2024, tests will be carried out to simulate the disruption of superconductivity and the operation of external resistor.

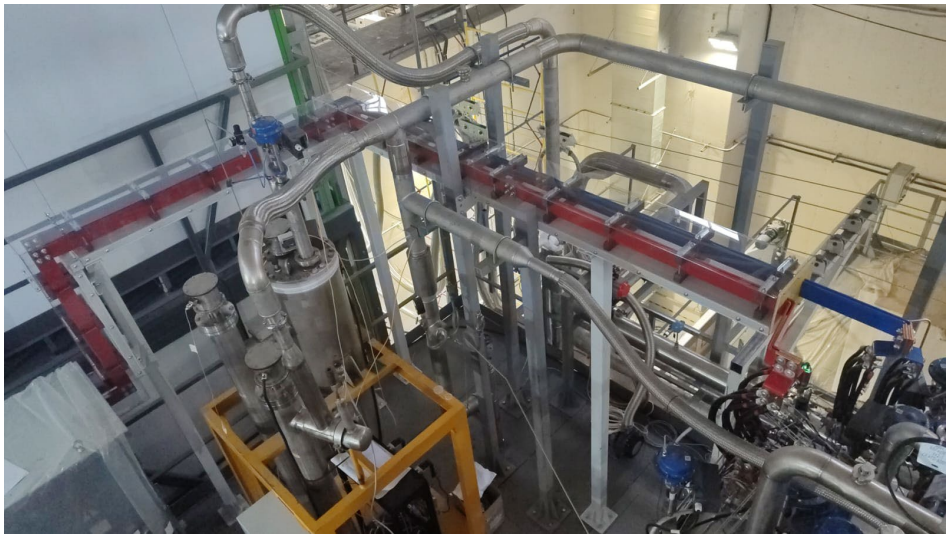

Figure 8. Busbar from the external resistor to the current leads of the SC magnet.

3.2.4.3. Magnet water cooling system.

The water cooling system ensures a stable temperature of the trim coils and power supplies. In January – May 2024, a design of cooling system was developed from an external source to a magnet cooling system. Currently the installation of cooling pipelines and sensors to the monitoring and control rack was carried out. The system is being flushed and by the early December 2024, thermal tests and commissioning of the system into regular operation will be completed.

3.2.4.4. Development of a volumetric magnetic field meter.

After CERN refused to deliver the magnetic field meter to HELP, the work on the development of a volumetric meter based on 3D Hall sensors was carried out by JINR employees, together with employees of the Budker Institute of Nuclear Physics (BINP). Currently, the manufacturing of the elements of equipment is in the final stage. The magnetic field meter is expected to be assembled and tested on the base of the BINP in December 2024,. The equipment is expected to be delivered to JINR at the end of 2024.

The plan for the commissioning of the MPD magnet in 2025.

In 2025, it is planned:

- to measure and map the magnetic field of the detector.
- to carry out the work on laying the main helium pipeline.

- optimize the operation of the equipment and begin preparations for commissioning and registration of pressurized equipment by “Rostechnadzor” (Federal Service for Environmental, Technological, and Nuclear Supervision of the Russian Federation) authorities.

- install the power frame into the solenoid.

- assemble and install a lifting platform for loading detectors from the west side.

- install suspensions for fixing the fiber-optic network, as well as flexible pipelines for supplying engineering gases.

The subdetectors will be assembled.

3.2.5 The main works planned within the framework of the project for 2026-2030.

The main task of 2026-2030 will be the operation of the detector for a physical experiment with improvements of all systems and automation of engineering equipment. It also requires the development and implementation of a project for the autonomous supply of a cryogenic system with gaseous helium from an external local compressor, a helium purification and storage system. As part of the extension of the project, work on the organization of backup autonomous power supply of the solenoid process equipment from an external generator will be carried out. Such actions will minimize the risks of equipment failure and extend the life cycle of the detector.

3.3 Time Projection Chamber - TPC

The time-projection chamber (TPC) is the main track detector of the MPD facility. Using this detector, the tracks of charged particles are reconstructed and their identification by specific losses in the detector working gas is carried out.

The parameters of the TPC are:

- acceptance η <1.2;
- momentum resolution ~ 3% (0.1 <Pt < 1 GeV/c);
- 2 track resolution - of the order of 1 cm;
- dE/dx resolution - not worse than 8%.

These parameters should be provided for the calculated luminosity of the NICA collider (at event multiplicity - up to 1000 tracks for central Au+Au collisions and event frequency - 7 kHz).

The radiation length of the cylindrical part of the TPC (for η= (0÷1.04)) is X/X0~ (9.2÷14.7)%. For end caps (η=(1.14÷2.06)) X/X0 is ~ (46 ±1)% (for the middle of ROC chamber (η=1.51) it is: C1+C2 cylinders + gas mixture ~ 5.65 %, ROC chamber ~ 14.23 %, FE electronics cards ~ 3.3 %, electronics cooling radiators ~ 11.9 %, LV power supply cables for FE cards ~ 9 %, end cup TPC thermalization shield ~ 1.62 %. Total X/X0 = 45.7%).

3.3.1. TPC design

The TPC consists of 4 cylinders (made of kevlar) with high stiffness (center deflection about of 0.1 mm or less) and low amount of material for the particle path (0.4 g/cm2). The gap between cylinders C1-C2 and C3-C4 is purged with nitrogen to prevent oxygen and water penetration from the air to the TPC volume and to protect against high-voltage breakdowns (operating voltage is about -25 kV). Fig.1 shows the scheme of TPC design, the location of the readout electronics and the direction of the beams.

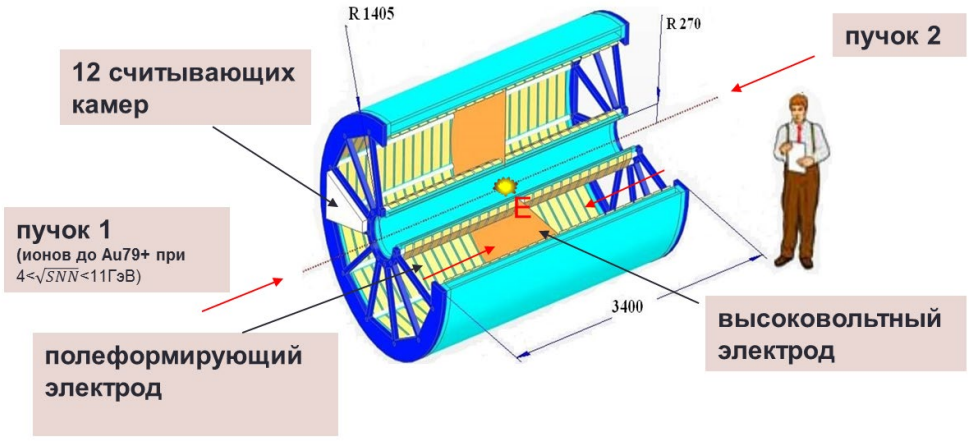

Fig.1 Schematic diagram of TPC design.

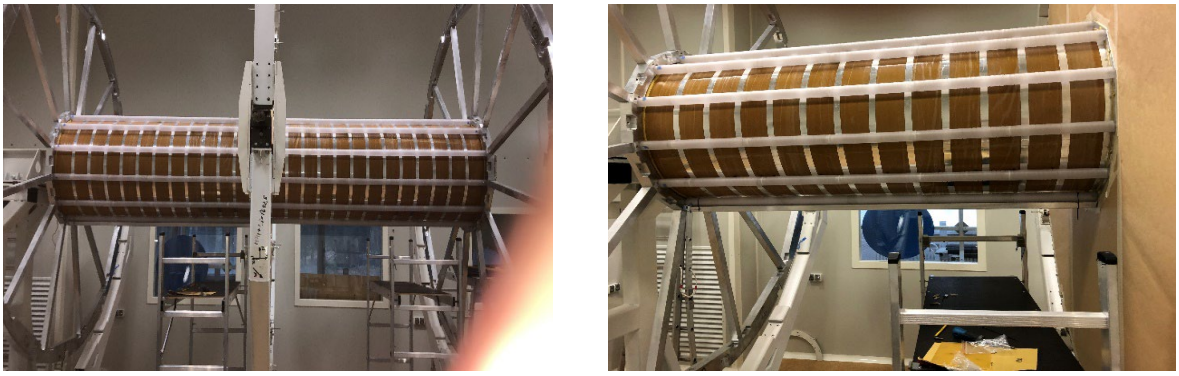

a) b)

Fig.2 Bonding of 2 flanges and high voltage electrode with C1-C2 cylinders (a). 12 tubes of the field cage system installed on the small radius of the TPC (b).

3.3.2 TPC subsystems

3.3.2.1 ROC chambers

Multiwire proportional chambers (MWPC) with cathode pads readout are chosen as baseline option. The chambers have a frame of only 13 mm width on each side, which ensures the maximum sensitive area of the chambers. Radiation length X/X0 ~ 7% is achieved by minimization of the material amount in the particle path by reducing the Al thickness of the ROC chamber frame to 5 mm without compromising its mechanical stability. Serial 24 + 2 spare ROC chambers were manufactured and tested (Fig.3-4).

Fig.3 Serial ROC chambers on the rack (26 pcs.).

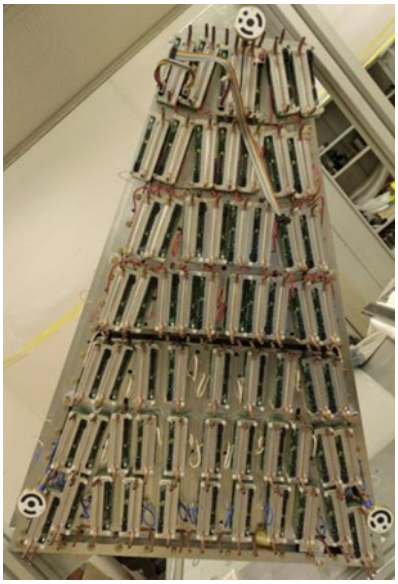

Fig.4 View of ROC chamber with installed readout electronics and cooling radiators.

Each chamber was tested first on Ar/CO2 gas mixture (80/20) and then on Ar/CH4 mixture (90/10). The test methodology includes measurement of dark current value, counting plateau, amplitude resolution, gas gain uniformity over the sensitive area and long-term stability testing.
For all ROC chambers the value of dark current in the operating range does not exceed I=1 nA. The operating voltage range is + (1400÷1550) V. The average value of amplitude resolution at uniform illumination by radiation from the Fe-55 radioactive source for all chambers is about 19%. Inhomogeneity of gas amplification at scanning by area and along the line (perpendicular to the anode wires) is about 16% at anode voltage of +1450 V for Ar/CH4 gas mixture (90/10). The long-term stability test showed that the change in the center of gravity of the main peak in the amplitude spectrum is not exceed a few percent and is in good agreement with changes in atmospheric pressure.
The distribution of the charge induced on the pad plane was tested with a 32 channel prototype card (FEC32S) based on the ASIC SAMPA. It is shown that charge is induced on 3 pads, which agrees well with the results of the pad response function calculations.
All chambers are checked for leakage. Gas leakage is less than 50 µliters/hour (10^{-3} cm3/min). The operation of the gating grid module developed in Minsk is checked. The rise time and fall time of the gating grid pulse is ~ 500 ns. To control the temperature, 4 Pt100 temperature sensors are installed on the body of each chamber.
The scheme of electronics arrangement on the ROC chamber was improved. For this purpose, the large and small radiators were upgraded and the length of flat kapton cables between the chamber and FE cards was optimized. All FE cards are now arranged in a single layer, simplifying assembly and reducing the radiation length of electronics with cooling radiators to X/X0 ~15%. The possibility of mounting the electronics (after the ROC chambers are installed into TPC) is shown.
Together with colleagues from PromGeodesia, the pads positions were measured using vector-geometric and photogrammetric methods. The position of 3968 pads in each ROC chamber is linked to the position of 3 photogrammetric marks on the chamber frame. Measurements are made for all ROC chambers.

3.3.2.2 Gas system

The gas mixture for the TPC consists of (10 ± 0.1) % CH4 in Ar at an overpressure in the TPC of dP=(2 ± 0.01) mbar. The rate of blowing the mixture through the TPC is (200÷3000) l/h. The gas system (Fig.5) is tested with the test gas volume in laboratory conditions and is currently in operation.

Fig.5 Testing of the gas system with the test volume in the LHEP bld.217.

3.3.2.3 Cooling system

The cooling system serves to temperature stabilization of the TPC and to cooling the readout electronics. The goal is to stabilize the gas mixture temperature within 0.5° C inside the TPC. The system is based on 235 Pt100 sensors placed on the TPC C4 cylinder, ROC chambers and FE card cooling radiators to provide temperature measurements with an accuracy of ~0.1°C. Distilled/deionized water is used as cooling fluid.

The full set of panels for the TPC thermal stabilization system and the full set of radiators for cooling the readout electronics are fabricated and delivered to JINR.

The cooling and thermal stabilization systems for the TPC and ECAL detectors consist of water tanks with pumps, water distribution and intake manifolds (Fig.6), piping systems on the outer surface of the MPD and piping inside the MPD. To prevent water leaks inside the MPD, all water in the pipes is pressurized below atmospheric pressure (leakless system). An automatic provides control and monitoring of the entire systems. The arrangement of tanks with collectors and 3 pumping groups on the 2nd floor of the 'South' platform has been designed. At this moment, the adopted technical solutions are being checked on a specialized stand, equipment and components are being purchased, delivered to JINR and the systems are being installed. The coordination of the equipment layout, pipes routing and thermometry system placement (between the Contractor (Research Institute of Nuclear Physics BSU, Minsk) and JINR) is in progress.

3.3.2.4 Laser calibration system

The TPC laser calibration system is required to minimize the error in the absolute measurement of particle track coordinates. In the TPC volume, 8 planes with 28 secondary laser beams in each are generated using the primary laser beam distribution system.

A design for the installation of micromirror assemblies in the tubes of the TPC field cage system has been developed. The process of assembly alignment in the tube is shown in Fig.7a). The micromirror assemblies are installed in all 8 tubes. A laser beam position detector was manufactured (Olomouc, Czech Republic). The detector was tested with a UV laser (see Fig.7b). Beam angles for micromirror assemblies were measured. Computer control of the 2 lasers of the TPC laser calibration system was developed.

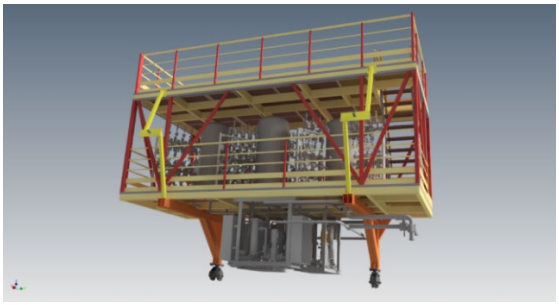

a)

b)

Fig.6 General view of the layout of the cooling and thermal stabilization systems of the TPC and ECAL detectors (a). View of 3 tanks with collectors and 3 pumping groups (b) on the 'Southern' platform.

a) b)

Fig.7 Tooling for alignment of micromirror assemblies in a tube (a). UV laser with beam position detector (b).

3.3.2.5 Data acquisition system and FEE readout electronics

The TPC data acquisition system (DAQ - Data Acquisition system) is designed to receive data from the TPC detector and contains 95232 channels. The main elements of DAQ are 1488 electronics modules (FEC - Front-End Card), 24 readout controllers (RCU - Readout and Control Unit) and 6 data concentrators (DCU - Data Concentrator Unit). The structural diagram of the TPC data acquisition system is shown in Fig.8.

FEC modules contain 64 channels and are based on specialized chips (ASIC SAMPA), programmable logic chips (FPGA) and high-speed serial data transmission interfaces. A general view of the FEC is shown in Fig. 9. At the moment, 102% of FECs have been manufactured. Preparations are underway to start production of a reserve batch of FEC modules. Testing of the fabricated FECs is ongoing.

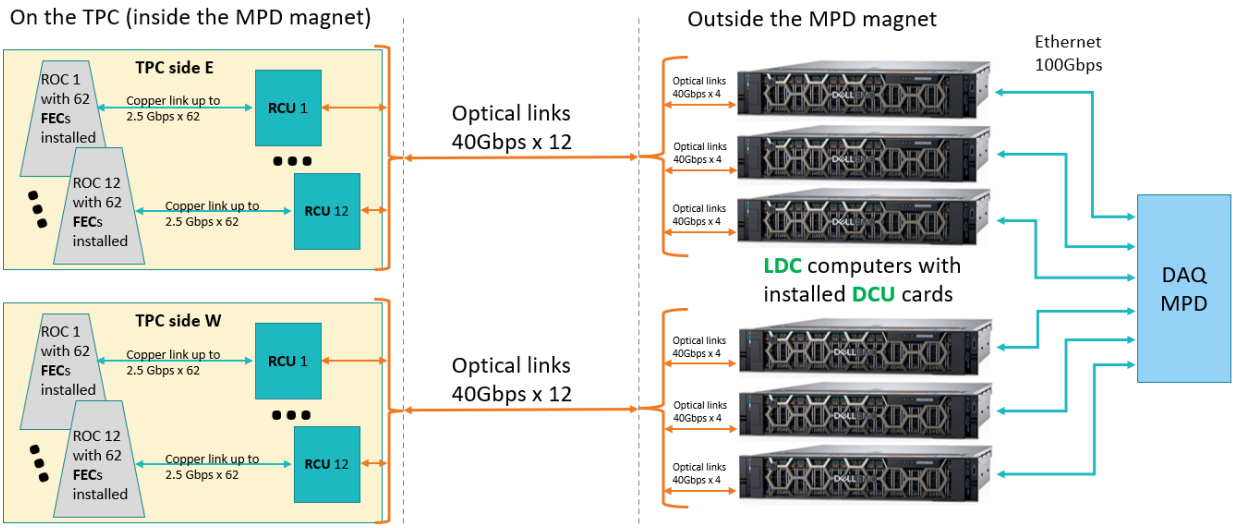

Fig.8 TPC data acquisition system structure diagram.

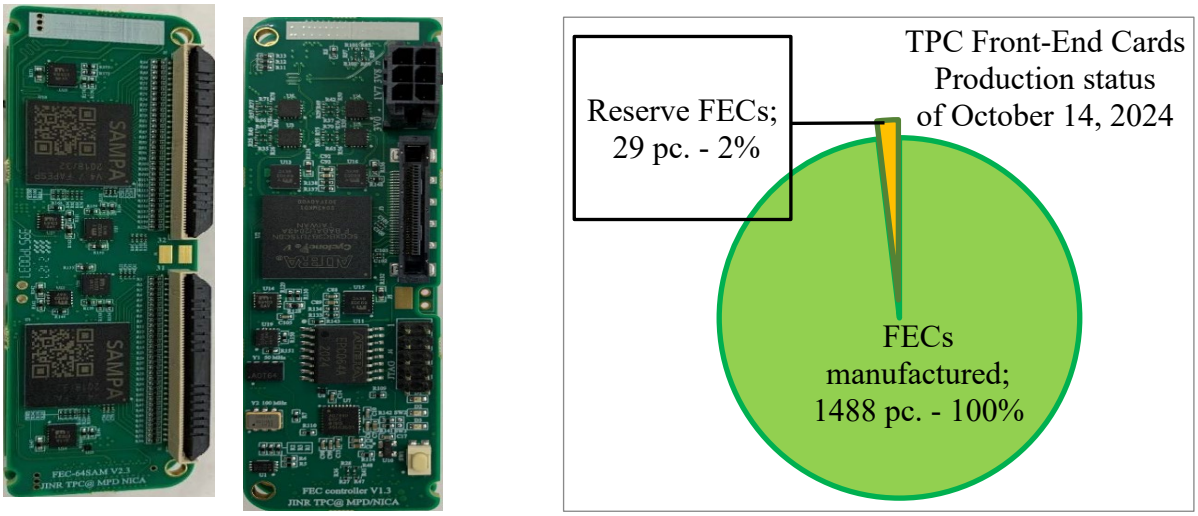

Fig.9 FEC modules: left - general view; right - manufacturing status.

RCU controller is designed to control and receive data from 62 FEC modules installed on one ROC chamber (Fig.10). At the moment testing of the RCU controller is being finalized and preparation for mass production of the RCU is underway.

Fig.10 General view of RCU controller.

DCU concentrator and LDC data storage

Each individual DCU hub receives data from 4 RCUs and is installed in a separate LDC data drive. The data acquisition system is fully equipped with the necessary number of DCU devices (6 pcs. + 2 reserve ones), the embedded software with basic functionality is prepared and the device is being tested as part of the data acquisition system. All necessary 6 servers + 1 for test set up were purchased and installed in a rack in MPD data center.

3.3.2.6 DAQ test benches

By the current moment 3 test benches with data acquisition systems + ROC chambers have been assembled (Fig.12). The first test bench is located in LHEP bld. 201 and is designed to tests DAQ with the ROC chamber switched OFF. The second stand is located in the LHEP bld. 40 and is intended for testing the DAQ with the ROC chamber ON and powering from serial (CAEN) low-voltage and high-voltage power supplies (including tests with radioactive source Fe-55 and X-ray). The third test bench is located in the Research Institute of Nuclear Physics BSU (Minsk) and is designed to identify and eliminate problems when testing FEC cards + standard cooling radiators

with data acquisition system, as well as to verify the operation of ROC chamber with readout electronics under different conditions (grounding, quality of the mains power, etc.) and for cross-check DAQ+ROC operation at Dubna and Minsk.

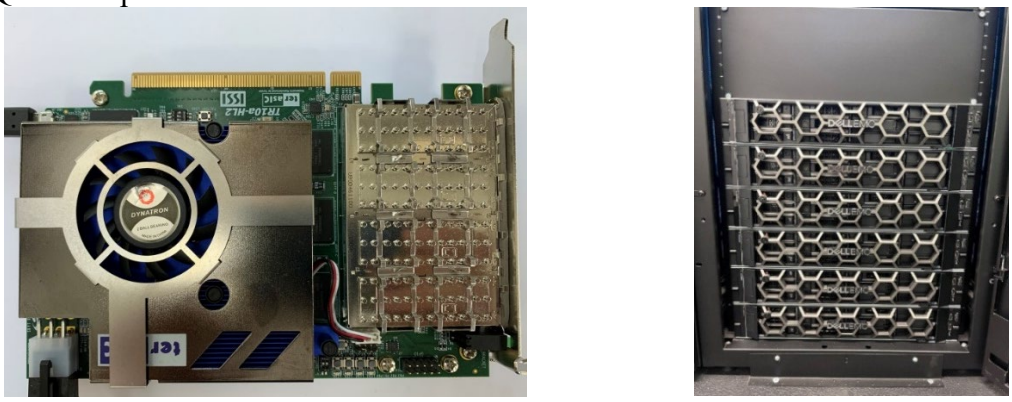

Fig.11 DCU concentrator and LDC data storage (left) and rack with LDC servers in the MPD data center (right).

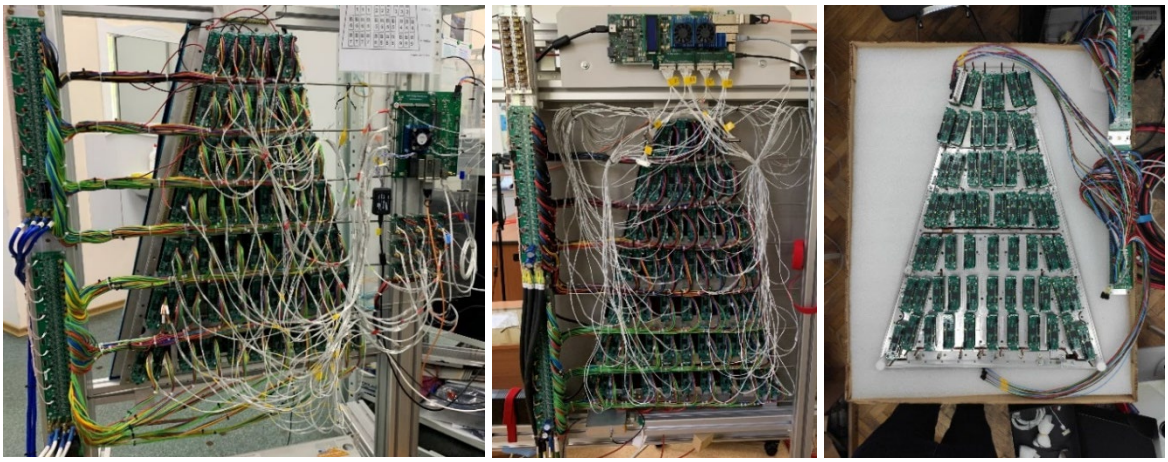

Fig.12 Test benches with data acquisition systems for a single ROC chamber. On the left - LHEP bld.201, in the centre – LHEP bld.40, on the right - Research Institute of Nuclear Physics at BSU (Minsk).

Fig.13 shows a visual picture of RMS noise for 3968 channels of the readout electronics connected to the ROC chamber pads for the test bench in the LHEP bld.201. Channels with a bigger noise (relative to the RMS=1.2ch ADC reference value) are indicated in red.

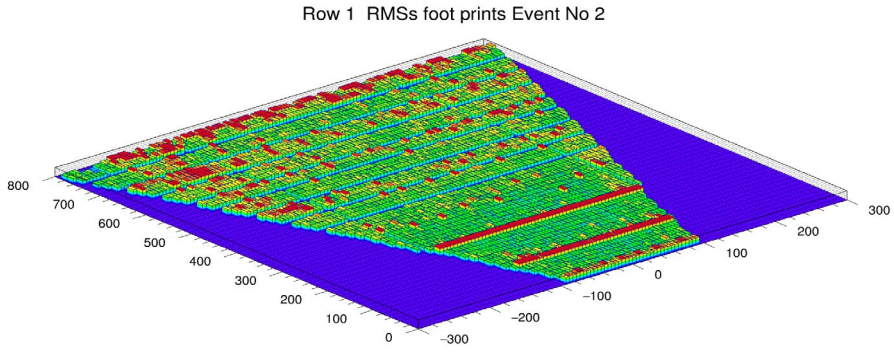

Fig.13 RMS noise for the 3968 channels of the readout electronics connected to the ROC chamber.

Low-voltage (LV) and high-voltage (HV) power supply system

The low-voltage and high-voltage power supply systems of the TPC are designed on the basis of CAEN radiation-resistant equipment (Fig.14). A complete set of equipment with spare modules is available.

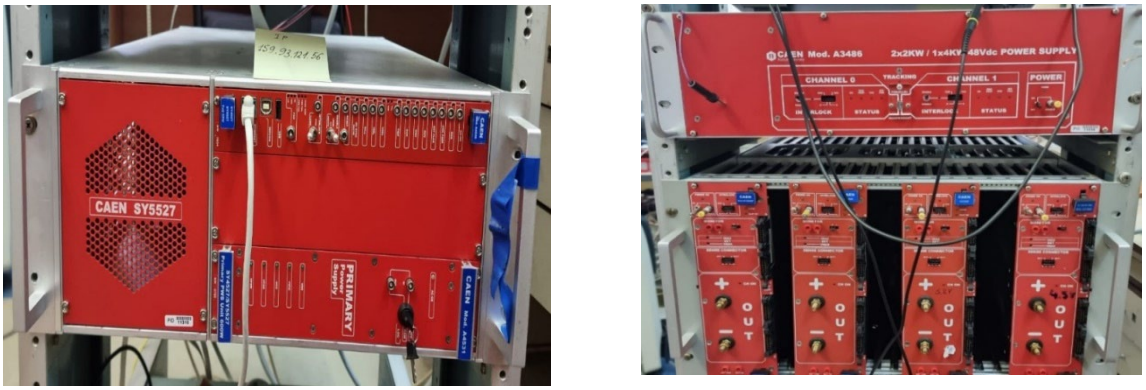

a) b)

Fig.14 LV power supply test system. Mainframe SY5527 by CAEN (a) and 3 phase A3486 AC/DC power supply with 4 pc A3100B power modules in the EASY3000 crate (b).

3.3.2.7 Slow Control System

The TPC includes the gas system, cooling system, laser system, low-voltage and high-voltage systems, high-voltage power supply for the membrane and other equipment. All these systems and equipment have their own control and parameter monitoring. For convenient operation and maintenance of TPC it is necessary to have a common control system - TPC SC. MasterScada 4D for 10 thousand parameters was chosen to create such a system. At the moment the control interface for low-voltage power supply system (see Fig.15) through OPC UA server developed and provided by CAEN company is implemented. In the future the TPC SC system will be integrated with MPD SC and RUN CONTROL systems.

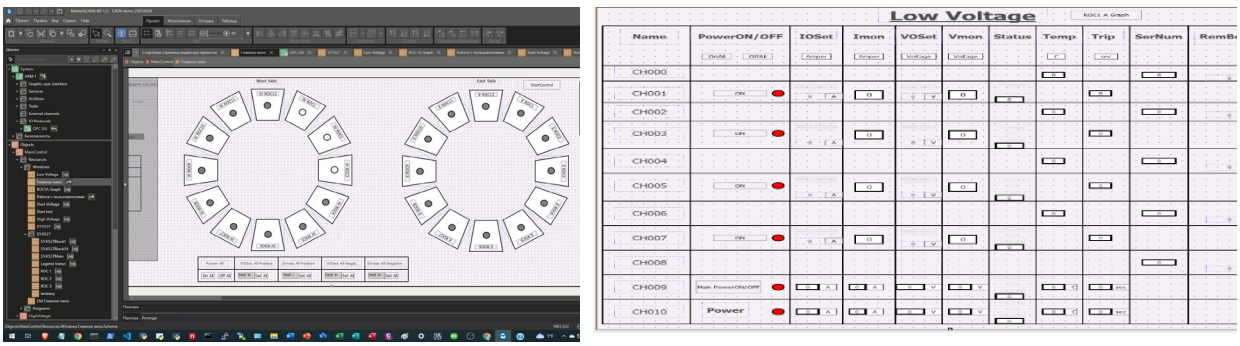

Fig.15 Slow control system for readout electronics low voltage power supply.

3.3.2.8 Equipment for TPC and tooling for installation TPC into the MPD

Work on the integration of the TPC detector equipment into the MPD facility is ongoing. There are 8 racks for TPC equipment. Racks are located on the 4-th floor of the MPD 'Electronic' platform. An occupancy scheme for these 8 racks has been developed (Figure 16a). The 'South' platform houses the cooling systems for the TPC and ECAL detectors (Fig.16b).

A specialized loading device has been developed for the installation TPC into the MPD (Fig.17a). Delivery of the loading device and specialized tooling to JINR is scheduled for December 2024 (Fig.17b).

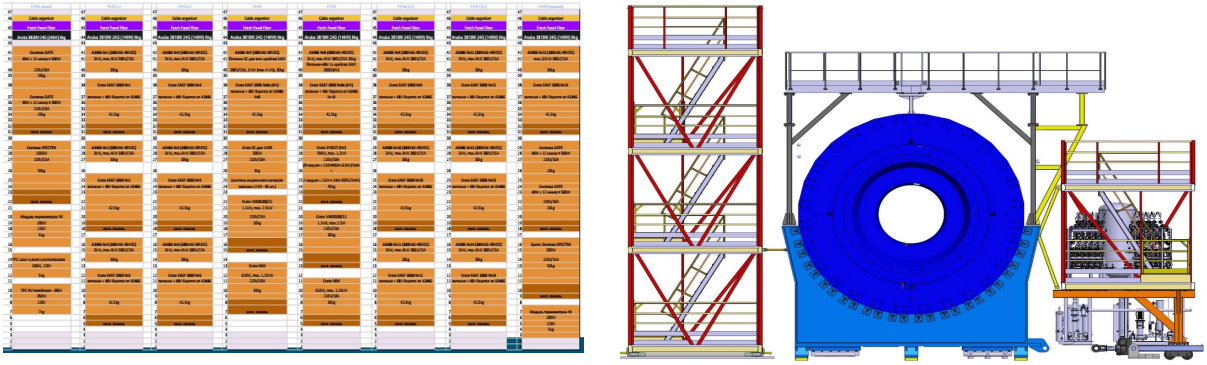

a) b)

Fig.16 Filling of 8 racks with TPC equipment on the 'Electronic' platform (a) and arrangement of cooling systems for TPC and ECAL detectors on the 'Southern' platform (b).

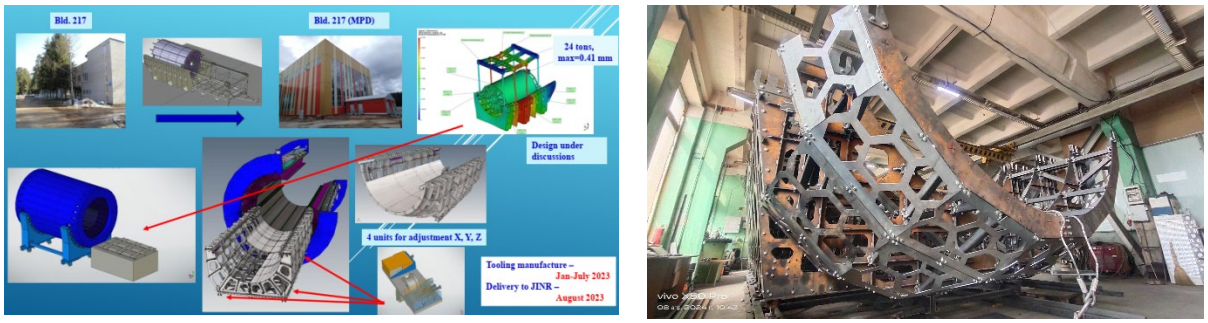

a) b)

Fig.17 Concept of TPC installation into the MPD (a). Loading device for installation TPC into MPD (b).

Reference

1. V. Abgaryan et al. (MPD Collaboration). Status and initial physics performance studies of the MPD experiment at NICA. Eur. Phys. J. A, V.**58**, 140 (2022). (*IF=2.6*)
https://doi.org/10.1140/epja/s10050-022-00750-6
2. A.Averyanov[1)], I.Balashov[1)], A.Bazhazhin[1)], V.F.Chepurnov[1)], V.V. Chepurnov[1)], G.Cheremukhina[1)], O. Fateev[1)], J. Lukstins[1)], A. Makarov[1)], G. Mescheryakov[1)], S.Movchan[1)1], A.Pilyar[1)], D.Potapov[1)], A.Ribakov[1)], V.Samsonov[1)],V.Serdyuk[1)], S.Vereschagin[1)], S.Zaporozhets[1)], V.Zruyev[1)], J.Fedotova[2)], Ya.Galkin[2)], A.Kunts[2)], A.Litomin[2)], S.Savitsky[2)], V.Tchekhovski[2)]. MPD TPC status // Physics of Atomic Nuclei, Vol. 86 (2023), No 5, pp. 796-804, DOI: 10.1134/S106377882305006X. (*IF=***0.3**)
3. S.V.Vereschagin, S.A.Zaporozhets, S.A.Movchan, and D.S.Potapov. Data Acquisition System of the TPC/MPD Detector for the NICA Project // Physics of Atomic Nuclei, Vol. 86 *(2023), No 5, pp. 805-809, DOI: 10.1134/S1063778823050411. (IF=0.3)*
4. Ya.D.Galkin, V.N.Zryuev, A.V Kunts, A.V Litomin, A.A.Makarov, G.V Meshcheryakov, S.A.Movchan, A.A.Rybakov, O.V.Fateev and V.A.Chekhovskii. Controlling Temperature Regimes of Electronics of the ROC Chamber of the TPC Detector for the MPD Experiment: Comparison of Experimental and Calculated Results.// *Physics of Particles and Nuclei, 2023, Vol. 54, No. 6, pp. 1120–1131. (IF=***0.6**)
5. Y.Ghoniem, A.Pilyar and T.Smolyanin. Slow control for MPD TPC LV and HV systems based on CAEN Equipment // Physics of Particles and Nuclei Letters, 2024, Vol. 21, No. 6, pp. 1145–1151. ISSN 1547-4771, © Pleiades Publishing, Ltd., 2024 (*IF=0.4*)

Conference

1. Sergey Movchan, TPC MPD Collaboration. TPC Assembling // VI-th Collaboration Meeting of the MPD Experiment at the NICA Facility, Joint Institute for Nuclear Research, Dubna, Russia, 2021.
https://indico.jinr.ru/event/2002/contributions/12063/attachments/9844/15924/61_Movchan_TPC status Collab meeting v02_20_04_2021.pdf
2. S. Movchan, TPC MPD Collaboration. MPD TPC STATUS // 6th International Conference on Particle Physics and Astrophysics (ICPPA), National Research Nuclear University “MEPhI”. Moscow, Russia, 2022.
https://indico.particle.mephi.ru/event/275/contributions/3141/attachments/1852/3260/76_MPD_TPC_Status_ICPPA-2022_v03_30_11_2022-fin.pdf
3. Bazhazhin A., TPC MPD Collaboration. STATUS OF THE TIME PROJECTION CHAMBER FOR THE MPD/NICA PROJECT // IV International Scientific Forum “NUCLEAR SCIENCE AND TECHNOLOGIES” dedicated to the 65th anniversary of the Institute of Nuclear Physics, , Алматы, Казахстан, 2022.
https://indico.alem.cloud/event/1/attachments/1/100/Abstract_v3.pdf
4. Sergey Movchan, TPC MPD Collaboration. MPD TPC status // IX Collaboration Meeting of the MPD Experiment at the NICA Facility, Joint Institute for Nuclear Research, Dubna, Russia.
https://indico.jinr.ru/event/2933/contributions/15779/attachments/12036/20611/70_Movchan_TPC status v03_25_04_2022.pdf
5. Sergey Movchan, TPC MPD Collaboration. MPD TPC status // X Collaboration Meeting of the MPD Experiment at the NICA Facility, JINR, Dubna, Russia, 2022.
https://indico.jinr.ru/event/3251/contributions/17606/attachments/13642/22652/75_Movchan_TPC status v05_08_11_2022 eng mov.pdf

---

[1)] ОИЯИ; [2)]ЯФ БГУ

6. Stepan Vereschagin, on behalf of the TPC/MPD group. Time Projection Chamber Assembling // XII Collaboration Meeting of the MPD Experiment at the NICA Facility, JINR, Vinca Institute of Nuclear Sciences, Belgrade, Serbia , 2023.
https://indico.jinr.ru/event/3746/contributions/20806/attachments/16941/28847/XII_MPD_collab_meeting_Vereschagin.pdf
7. Stepan Vereschagin, on behalf of the TPC/MPD group. Data acquisition system of the TPC/MPD detector of the NICA project". 6th International Conference on Particle Physics and Astrophysics (ICPPA2022), Moscow, Russia, December 2, 2022.
https://yandex.ru/search/?text=6th+International+Conference+on+Particle+Physics+and+Astrophysics+(ICPPA2022)%2C+Moscow%2C+Russia%2C+December+2%2C+2022.&clid=2052601&banerid=6400000000%3A58f49f054bd85c0019c5755a&win=250&lr=215
8. Stepan Vereschagin, on behalf of the TPC/MPD group . Time-projection chamber for MPD // IUPAP Conference "Heaviest nuclei and atoms", National Academy of Sciences of the Republic of Armenia, 2023, Republic of Armenia.
https://indico.jinr.ru/event/3622/
9. Stepan Vereschagin, on behalf of the TPC/MPD group . Data acquisition system of the TPC/MPD detector for the NICA project.// The 6th Technology and Instrumentation in Particle Physics (TIPP 2023) conference, iThemba LABS, IUPAP, Department of Science and Innovation of South Africa, Cape Town, South Africa, 4-8 September 2023
https://indico.tlabs.ac.za/event/112/contributions/2773/
10. A.Bazhazhin. TPC MPD Collaboration. Status of some parts of the TPC for the MPD at the NICA facility // The XV-th International School-Conference "The Actual Problems of Microworld Physics", 2023, Minsk, Belarus.
https://indico.jinr.ru/event/3604/contributions/22636/
11. S.Movchan, TPC MPD Collaboration. MPD TPC STATUS // The XV-th International School-Conference "The Actual Problems of Microworld Physics", Joint Institute for Nuclear Research (Dubna, Russia), Institute for Nuclear Problems of Belarusian State University (Minsk, Belarus), B.Stepanov Institute of Physics of the National Academy of Sciences of Belarus (Minsk, Belarus), Minsk, Belarus, 2023
https://indico.jinr.ru/event/3604/contributions/22633/attachments/16599/28318/82_MPD TPCstatus v06 30_08_2023_K.pdf
12. A.S. Fedotov, I.Zur. The computer-aided design of cooling system for MPD detector of NICA // The XV-th International School-Conference "The Actual Problems of Microworld Physics": Scientific Program (Minsk, Belarus, 27 August – 3 September, 2023). – Minsk, 2023. – P.3.

3.4 TOF identification system

3.4.1 Time-of-flight system design

The time-of-flight (TOF) system is the basic identification system for charged hadrons of the multipurpose detector (MPD). In the initial configuration, the TOF will be represented as a cylinder about 6 meters long and 3 meters in diameter, assembled from 28 modules (Fig. 1). Each module contains 10 MRPC subdetectors (Fig. 2). The TOF detector system is organized according to the modular principle in order to minimize the number of components and cost. In addition to the TOF modules themselves, the system includes the following service subsystems: low and high voltage power supplies, gas system, data acquisition electronics, cooling and slow control.

Each TOF module consists of 10 identical multigap resistive plate chambers (MRPCs) with 24 readout strips each. The development and testing of MRPC prototypes were carried out between 2013 and 2017. During this time, several different versions of the MRPC were tested using cosmic rays and a Nuclotron deuteron beam. The final version of the MRPC is made of commercial float glass with a thickness of 280 microns. It has 15 gas gaps with a width of 200 microns and provides a time resolution of 50 ps.

MPDRoot simulation has shown high identification efficiency (Fig. 2) when using such a design of MRPC detectors and TOF configuration.

Mass production of TOF detectors and modules began in 2019. The assembling of 300 MPCs and 28 TOF modules was completed in 2023. All TOF modules passed long-term testing on cosmic rays. Currently, ready-to-install TOF modules are stored in special racks (Fig. 3).

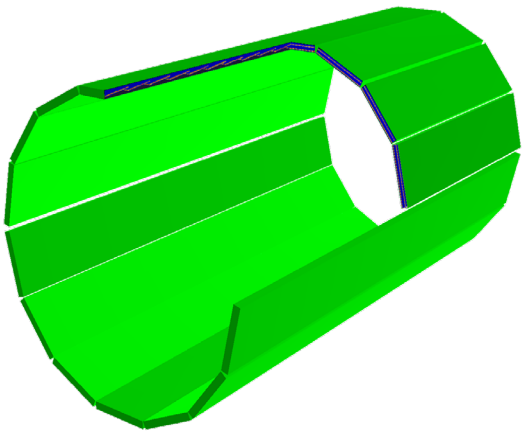

Fig. 1. TOF geometry in MPDRoot.

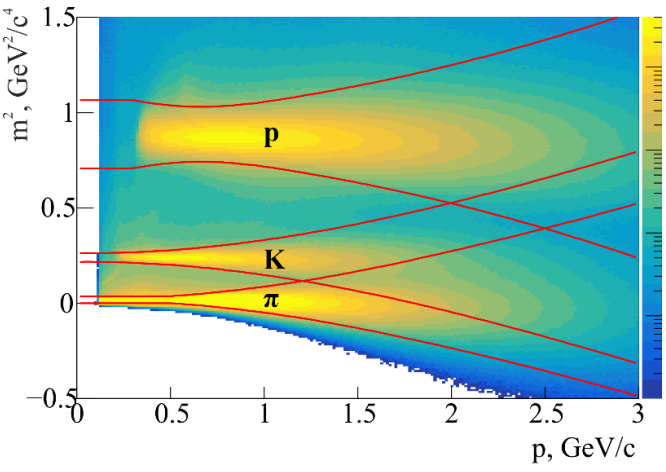

Fig. 2. Identification by the m^2 using TOF.

Fig. 3. Assembled and tested TOF modules are stored in racks

3.4.2 Readout electronics and data acquisition system

A 24-channel PA2402V4 discriminator preamplifier based on the NINO chip was developed for the TOF MPD (Fig. 4). This preamp board is specially adapted for two-side reading of signals from both ends of MRPC strip electrodes in the MPD experiment. The distinctive features of the MPD TOF preamplifier board are: stabilized NINO power supply voltage; input impedance matched with the impedance of the detector electrodes and cables; capacitors at the inputs for two-side reading of signals; remote monitoring and control of discrimination thresholds and amplifier power supply, as well as the presence of sensors to measure the temperature of the amplifier board and the gas volume below it. Production and testing of all 560 preamps were completed at the end of 2019.

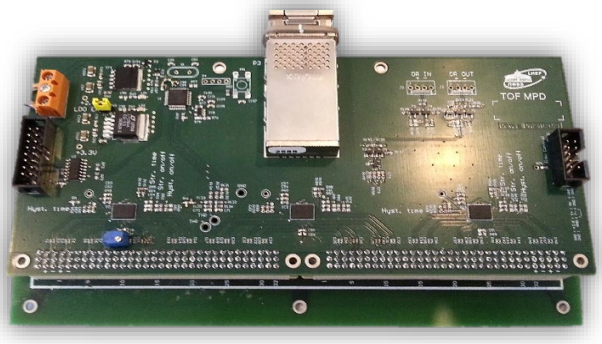

Fig. 4. 24-channel PA2402V4 preamp based on NINO chip.

Fig. 5. 72-channel time-to-digital converter TDC72VXS based on HPTDC.

The TDC72VXS time-to-digital converter (Fig.4) based on the HPTDC chip was specially developed for data readout from MPD TOF and FFS systems. It is used to digitize LVDS signals coming from the output of the NINO amplifier using Molex P/N11102512xx cables with Molex 76105-0585 connectors. The sampling time of the TDC72VXS is 24 ps. The measured time resolution of the TDC, after taking into account all nonlinearities, is about 20 ps. The TDC module provides the possibility of accurate time synchronization with other devices using the ”White Rabbit" technology. The total number of TDCs required for MPD TOF is 196 (14 modules for each of the 14 WIENER VME-VXS crates).

All VXS crates were purchased and delivered to JINR in 2017-2019. The TDC72VXS modules are also fully produced with spare in 2020. Testing and calibration of the readout and data acquisition electronics was completed in 2022.

3.4.3. Closed-loop gas system

TOF detectors will work with a non-flammable gas mixture containing 90% C2H2F4 + 5% i-C4H10 + 5% SF6. The total volume of gas in a TOF barrel is approximately 3,000 liters, taking into account the volume occupied by the detectors. Due to such a large volume of gas, it was decided to use a closed-loop gas supply system with recirculation and purification of the gas mixture.

In 2024, the purchase of equipment for the gas system is completed. Installation work is underway. The racks (cabinets) of the control, mixer, recirculation unit, analyzer and purifier of the gas mixture are assembled. The racks of the gas distribution system of the mixture into the TOF modules are also ready for installation on the 3rd floor of the MPD electronic platform. All the main elements of the TOF gas system, together with the cylinders, will be placed in the western half of the MPD hall (Fig. 6). The gas supply system racks in the hall and on the platform will be connected by steel pipe lines laid along the walls, as well as a flexible stainless steel metal sleeve necessary to move the MPD detector from the service to the working position.

The installation of the TOF gas system is scheduled to be completed in early 2025. In the first half of 2025, the automatic gas supply control system will be configured and debugged. It is planned to test and put the system into operation by July 2025.

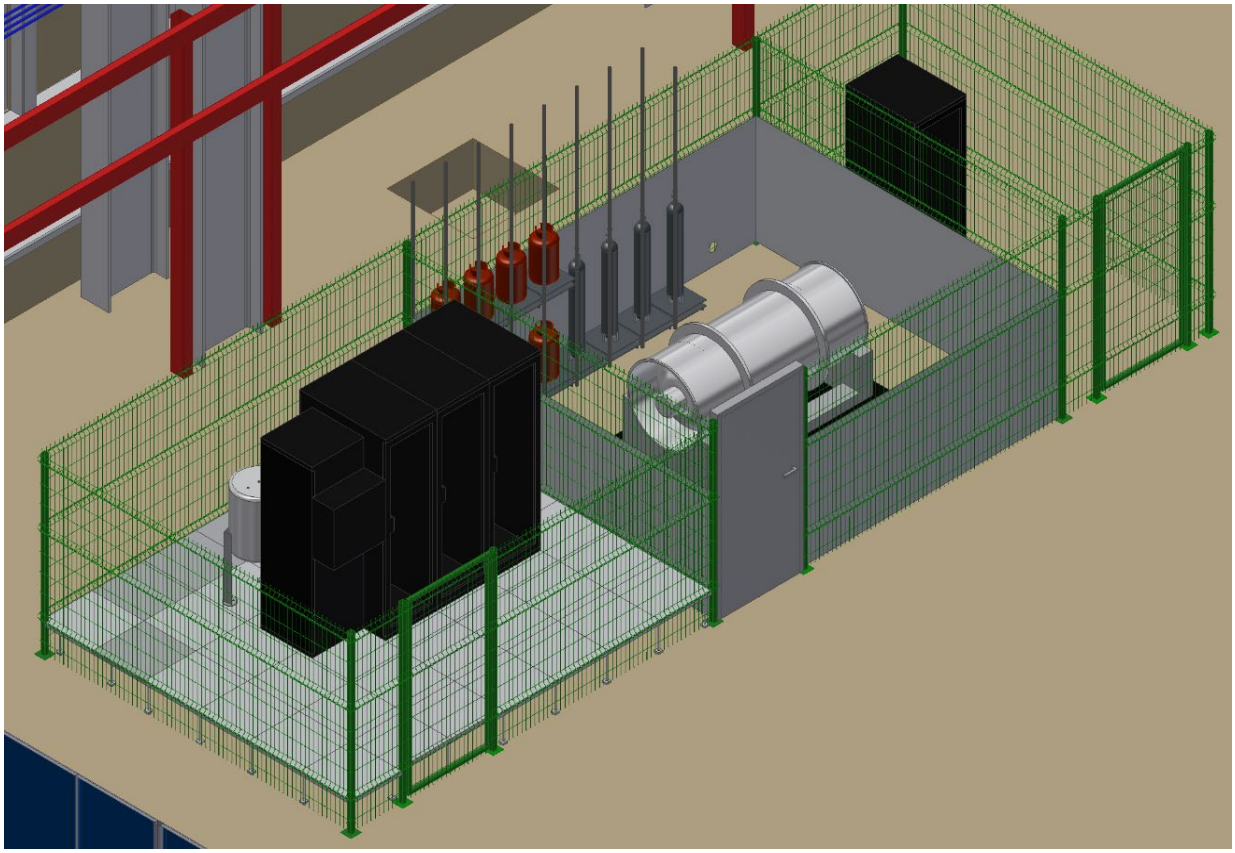

Fig. 6. The model of the location of the gas system equipment in the MPD hall.

3.4.4. High-voltage and low-voltage power supply systems

To supply high voltage to the detectors in the TOF modules, high-voltage sources manufactured by iSeg (Germany) in the WIENER MPod standard are used. The entire TOF high-voltage power supply system consists of 28 4-channel iSeg EHS4080p(n) power supplies (up to 8 kV/1 mA) located in four MPod crates. All iSeg high-voltage modules and MPod crates were purchased in 2017-2019. Cables and connectors required for high voltage supply were purchased in 2020. The distribution of high voltage to the detectors is carried out using a special HVDCM distribution device. By 2023, all HVDCM boxes have been manufactured and tested.

To power 560 preamps of the TOF system, 14 WIENER MPV8016I low-voltage power sources in the MPod standard are sufficient. Each MPV8016I low voltage module has 8 power channels with a maximum power of 50W per channel at a supply voltage from 0 to 15 V. Low-voltage power supply modules and cables for supplying voltage to TOF modules were purchased and delivered to the VBLHEP in 2017-2020 in full.

The crate with high-voltage and low-voltage power modules is planned to be installed on the 3rd floor of the electronic platform in the first half of 2025.

3.4.5. TOF modules integration

The installation of the TOF modules will begin after the installation of the ECal modules is completed. Each TOF module will be installed in its place on both sides of the magnet yoke one at a time. The installation will be carried out using a mobile support structure (Fig. 7). The structure is equipped with guide rails of the same type as inside the MPD power frame. In order to install the module in the MPD, it is enough to fix the support structure on the lifting platform in front of the required sector and connect the rails together so that a single sliding line is formed, which will allow the module to be pushed into the desired position.

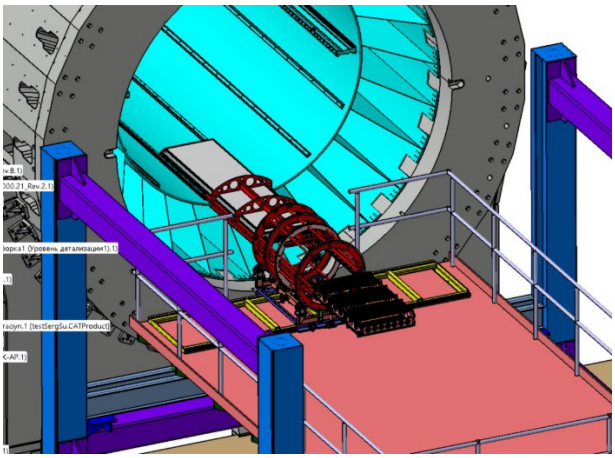

Fig. 7. TOF integration equipment.

Fig. 8. Installation bench test

All TOF integration equipment was designed and manufactured from 2020 to 2023. In 2023, guide rails were installed on the power frame. In 2024, the procedure for installing the module on rails in the power frame was worked out with a fully assembled TOF module (Fig. 8).

The final installation of TOF modules on the MPD power frame is planned to be completed in the second half of 2025. After that, power, signal and slow control cables, as well as gas supply and cooling hoses will be laid.

3.4.7. Slow control system

The slow control and monitoring system is necessary to control and monitor the parameters of TOF MPD service subsystems, such as the gas system, high-voltage and low-voltage systems, on-camera electronics, etc. Currently, most of the control system has been developed, is actively used in testing and continues to be improved. In 2025, it is planned to complete the creation of the TOF slow control system and integrate it into the global Detector Control System (DCS).

3.4.8. Cooling system

Cooling of the front-end electronics is necessary to meet the temperature requirements of the central MPD area (the detector surface must have a temperature no higher than 25 °C). The

readout electronics of all TOF modules emit up to 1 kW of thermal power. That is, 18 watts per square meter of the surface of the TOF modules. In this case, the most optimal cooling method for removing heat from TOF modules is the use of an air cooling. This option is more acceptable than water cooling due to its low cost, lower probability of damage to electronics and the absence excess materials in the modules affecting particle characteristics. However, this method does not allow to control the process of thermal stabilization.

The design of the TOF air cooling system was carried out in 2024. In accordance with the project, cooling system equipment will be purchased and installed on MPD in 2025.

Publications in 2021-2024.

1. *Статус времяпролетной системы TOF эксперимента MPD на коллайдере NICA*. В.М. Барышников, В.А. Бабкин, С.Г. Бузин, А.С. Бурдыко, М.Г. Буряков, В.М. Головатюк, А.В. Дмитриев, П.О. Дулов, М.М. Румянцев, С. Ромахов, Т. Смолянин, А.А. Федюнин, С.П. Лобастов и др., Ученые записки физического факультета Московского университета, 3, 2330204, 2023

2. *Status of the Time-of-Flight System of the MPD Experiment at the NICA Collider*. V. Baryshnikov, V. Babkin, S. Buzin, A. Burdyko, M. Buryakov, V. Golovatyuk, A. Dmitriev, P. Dulov, M. Rumyantsev, S. Romakhov, T. Smolyanin, V. Dronik, E. Kidanova, A. Pyatigor, K и др., Physics of atomic nuclei, 86, 5, p. 788 - 795, 2023.

3. *Bayesian Approach to Particles Identification in the MPD Experiment*. V.A. Babkin, V.M. Baryshnikov, M.G. Buryakov, S.G. Buzin, A.V. Dmitriev, V.I. Dronik, P.O. Dulov, A.A. Fedyunin, V.M. Golovatyuk, E.Yu. Kidanova, S.P. Lobastov, A.D. Pyatigor, M.M. Rump., Journal of instrumentation, 19, P08007, 2024

Conference reports in 2021-2024.

1. V. Baryshnikov, *Software method of determination of the event collision time with the TOF detector of the MPD at NICA*, IV International Scientific Forum “NUCLEAR SCIENCE AND TECHNOLOGIES”, Almaty, Kazakhstan, 26.09.2022.

2. V. Baryshnikov, *Status of the Time-of-Flight and ECal Particle Identification Systems of the MPD Experiment at the NICA Collider*, 21st Lomonosov Conference on Elementary Particle Physics, Moscow State University, Moscow, Russia, 27.08.2023.

3. V. Babkin, *Overview of MRPC based ToF systems developed in JINR*, The 2023 International Workshop on the High Energy Circular Electron Positron Collider, Nanjing University, Nanjing, China, 24.10.2023.

4. Бабкин В.А., *Наука и технологии на ускорительном комплексе NICA*, Всероссийская научная конференция студентов-физиков (ВНКСФ-28), СО РАН, Россия, Новосибирск, 01.04.2024.

5. V. Babkin, *Status and Prospects of the MPD Time-of-Flight Identification System at NICA*, The 2nd China-Russia Joint Workshop on NICA Facility, Shandong University, Tsinghua University, Qingdao, Beijing, China, 13.09.2024.

Presented PhD thesis in 2021-2024

Бабкин В.А. Времяпролетная система идентификации частиц Многоцелевого детектора (MPD). 01.04.01: приборы и методы экспериментальной физики, физико-математические, 20.4.2021.

3.5 Fast Forward Detector (FFD)

The FFD is designed for fast detection of nucleus – nucleus collision events at the center of the MPD facility, determination of the position of the interaction point, generation of the necessary trigger signals for the MPD experiment and the T0 pulse for the TOF detector.

The FFD detector consists of two identical sub-detectors FFD_E и FFD_W, located along the beam axis at a distance of 140 cm from the center of the MPD setup, as shown in Fig. 1. Each of them has a modular structure and contains 20 Cherenkov modules and 80 independent registration channels.

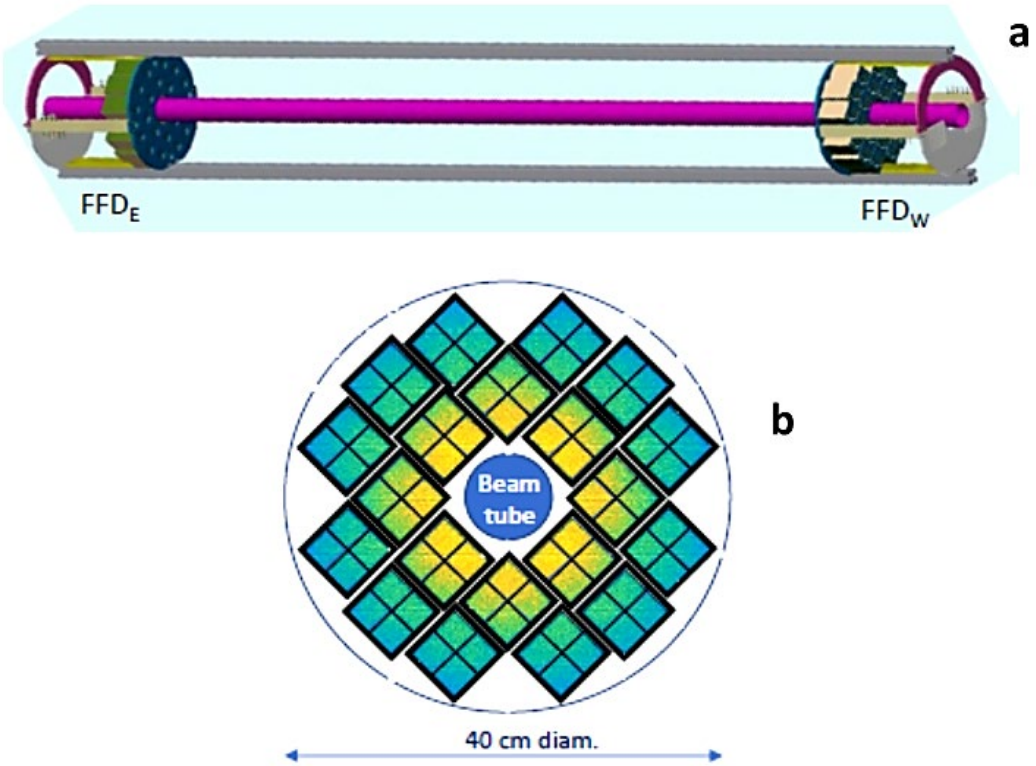

Fig. 1. View of the FFD detector (a) and the modular sub-detector assembly (b).

In addition to the sub-detectors, the FFD includes other subsystems that ensure its operation, signal processing to achieve the FFD goals, calibration and control. These subsystems, shown in Fig. 2, are: electronics for receiving and branching LVDS pulses of the detector modules, which also includes low-voltage power supply for the front-end electronics of the modules (Fanout + LV); electronics for processing LVDS pulses and generating signals for the MPD trigger (FFD trigger crate); a high-voltage power supply system for the photomultipliers of the detector modules (HV crate); a system for monitoring analog pulses of the detector (Multiplexers + CAEN digitizers); a laser calibration system based on a picosecond laser (Laser & Ref. detector + Laser patch boxes); a system for cooling and monitoring the temperature of the detector modules; a system for controlling the detector subsystems and interacting with the MPD control system (Detector Control System, DSC), and a cable system.

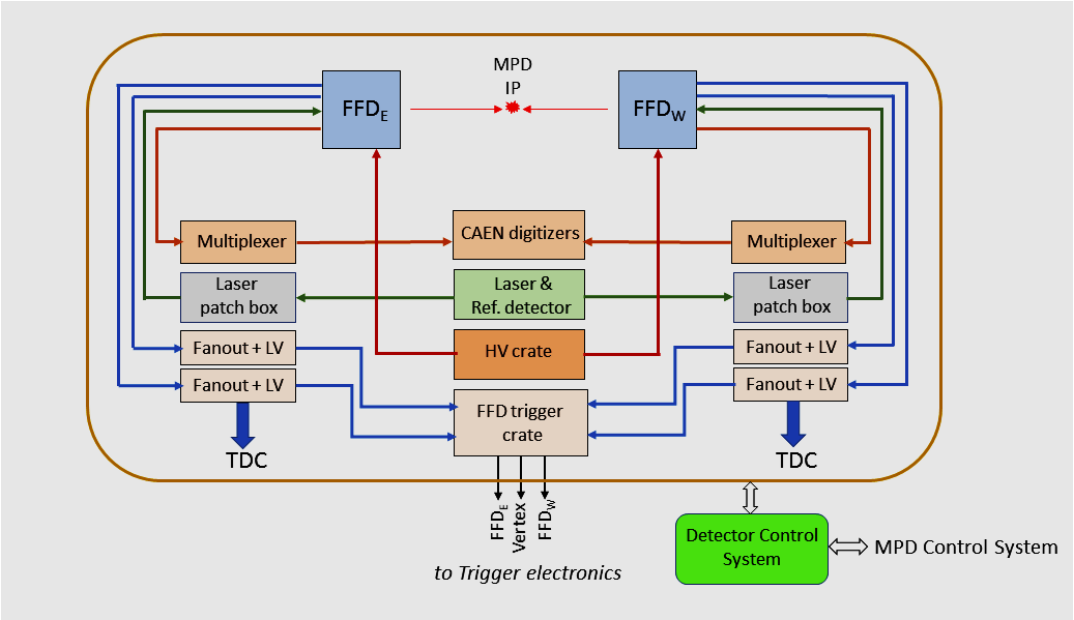

Fig. 2. A scheme of the FFD subsystems.

The results of the FFD detector project implementation over the past period are described below.

Sub-detectors FFD$_E$ и FFD$_W$ are created in full (20 + 20 modules). Each module includes 4 quartz radiators, an XP85012/A1 photomultiplier based on an assembly of two MCPs, a front-end electronics board, a lead gamma-ray converter in front of the radiators, a high-voltage divider and a housing. A photo of the module is shown in Fig. 3 on the left. The mechanical design of the sub-detectors is shown in Fig. 3 on the right.

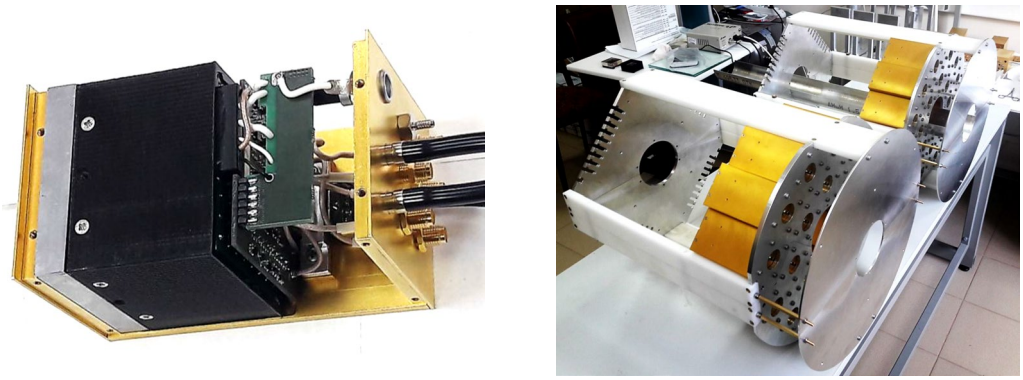

Fig.3. FFD detector module (left) and modular assemblies of FFD$_E$ and FFD$_W$ sub-detectors (right).

The FFD$_E$ and FFD$_W$ sub-detectors are now ready for final laboratory testing.

The electronics for receiving/branching LVDS pulses and LV power supply of the front-end electronics consists of 4 electronic modules for each sub-detector, placed in a mini-crate. LV power supply is controlled by the DCS system. The modules and crates were developed and manufactured at LHEP JINR, and their creation and testing was completed in 2024.

The electronics for processing LVDS pulses and generating signals for the trigger were developed, manufactured and tested at LHEP JINR. It has a modular structure and consists of 4 + 4 modules placed in a VME crate. In 2024, the creation of these modules and the crate was completed. In 2025, it is planned to manufacture the last module of this subsystem, responsible for generating the Vertex signal for the MPD trigger. The electronic modules use FPGA technology with control from the DCS system.

The high-voltage power supply system of the FFD detector is based on a crate with three 16-channel modules manufactured by Wiener/Iseg (Germany). All module outputs have independent floating ground and adjustable voltage up to -3 kV. The high-voltage system is controlled via DCS with the help of a user interface and it has passed the necessary tests. It is currently used in the laboratory for test measurements with FFD modules.

The detector analog pulse control system is designed to set the optimal detector operating mode and to perform operational control and analysis of the pulse shape generated by the FFD modules. The electronics of the sub-detector multiplexers allows for a 4-fold reduction in the number of output pulses by controlled switching of input channels. The modules of this electronics were developed, manufactured and tested over the past 5 years. Pulse shape measurement is performed using N6742 digitizer modules from CAEN, purchased in the past period together with the data transmission system to the computer. This subsystem is now fully ready for final testing.

The laser calibration system was manufactured during the previous period of the FFD project implementation based on the PiLas picosecond laser with a pulse width of 30 ps and a wavelength of 405 nm (manufacturer Advanced Laser Diode Systems, Germany). The system includes: a PiLas laser control module, a laser emitter with an optical system for uniform illumination of 130 quartz fibers WF100/140/300N, NA 0.22 (manufacturer CeramOptec Co.). Light pulses are transmitted to the front ends of the FFD detector modules and the reference detector. In 2024, a control interface was developed as part of the DCS system.

The cooling and temperature control system of the detector modules was developed to minimize and control the heat generation inside the FFD detector modules. This is done by blowing the modules with compressed cooled air or nitrogen at a flow rate of 100 l/min per sub-detector, which ensures the removal of half of the generated thermal energy. At the same time, the remaining heat generation in the sub-detector is only 10 W. It is assumed that the operating temperature inside the modules will not exceed 25°C. All components of the local FFD cooling system are available, and the system has been successfully tested in the laboratory. Thermal sensors are used to measure the temperature inside and outside the modules. The information read from them is used for automatic air flow adjustment and is simultaneously displayed on the monitor for operational control.

The control detector system DCS is built using the client-server architecture and includes control and monitoring of all FFD subsystems. At the same time, several levels of control of the subsystems state are used, ensuring timely decision-making in case of significant deviation of the operating regime from the established one, including emergency shutdown. At present, the developed system is being debugged in test measurements in the laboratory.

The cable system includes sets of all types of cables used in FFD subsystems: HDMI and Molex cables for LVDS pulse transmission, coaxial cables for analog pulses, optical cables for

the laser system, high-voltage cables for PMT power supply, power supply cables, DCS control cables. All cables are manufactured, tested and used in full-scale FFD testing in the laboratory.

The readout electronics used for LVDS pulses of the FFD consists of two modules TDC72 VHL for each sub-detector and sits in VME crates of the TOF readout system.

Long term test with cosmic muons and laser is prepared in our laboratory with full scale FFD including all subsystems. In previous years for this aim, a special stand with four granulated scintillation layers was designed and produced for triggering events induced by cosmic muons. We plan to begin the test measurements in December 2024 and it will continue during the first half of 2025. The main goal of the study is to get stable operation of the FFD subsystems with required parameters under control of the DCS.

In the second half of 2025 the FFD will be ready for installation into the MPD setup.

Readiness of FFD in December 2024

- Subdetectors FFD_E and FFD_W – 100%
- HV & LV system – 100%
- Electronics – 95% (Vertex module in production, final test is required)
- Laser system – 100%
- Cooling system – 100%
- Detector Control System – 95% (final test is required)
- Cable system – 95% (some special cables and patch panels are required)

Full readiness planned will be in September 2025.

Publications

V. I. Yurevich, S. A. Sedykh, S. V. Sergeev, D. N. Bogoslovski, V. Yu. Rogov, V. V. Tikhomirov and N. A. Lashmanov, *Development of scintillation detectors with SiPM readout for the NICA project*, Applications of Nuclear Techniques (CRETE19), International Journal of Modern Physics: Conference Series Vol. 50 (2020) 2060008.

Conference reports

V. I. Yurevich, S. A. Sedykh, S. V. Sergeev, V. Yu. Rogov, V. V. Tikhomirov, N. A. Lashmanov, A. A.Timoshenko, N. A. Kozlenko, Fast Interaction Trigger for MPD Experiment at NICA (Poster), The International Conference "Instrumentation for Colliding Beam Physics" (INSTR-20), Novosibirsk, Budker Institute of Nuclear Physics, 24-28 February 2020.

3.6 Forward Hadron Calorimeter (FHCal)

The Forward Hadron Calorimeter (FHCal) is one of the basic detectors of MPD setup which is intended for the measurements of the geometry of heavy ion collisions and for the production of minimum bias trigger. The calorimeter is constructed in the frame of the collaboration between JINR and INR RAS (Moscow). The main purpose of the FHCal is to provide an experimental measurement of a heavy-ion collision centrality and orientation of its reaction plane.

FHCal consists of two identical arms placed upstream and downstream the beam collision point. The modular structure of one FHCal arm, scheme and photo of individual module are presented in Fig.1.

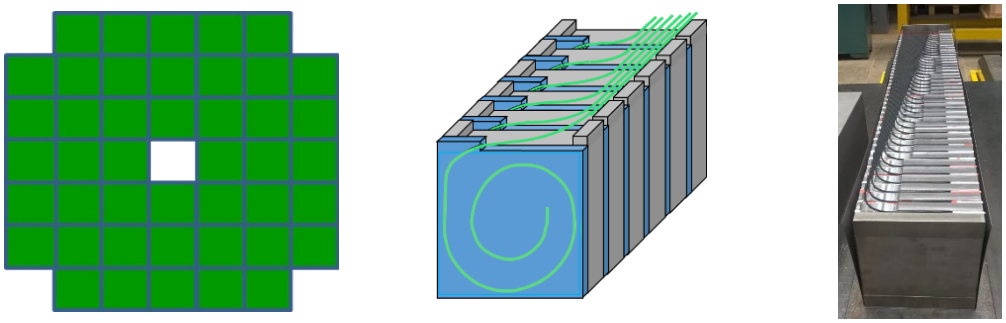

Fig.1. Left - the modular structure of the FHCal. Center – the scheme of the individual FHCal module. Right- photo of assembled module.

FHCal design

Each arm of hadron calorimeter consists of 44 individual modules with transverse sizes of 15 × 15 cm^2. The central hole has the same size to provide the positioning of beam pipe. Each module consists of 42 lead–scintillator tile sandwiches with the thickness of the lead plates and scintillator tiles 16 and 4 mm, respectively. The obtained sampling ratio 4:1 satisfies the compensation condition and provides the optimum energy resolution. According to simulation, the sampling fluctuations provide the energy resolution of calorimeter as: $\sigma_E/E \sim \sqrt{}55\%/E$ (GeV) The beam tests of the calorimeter with the same sampling confirm the results of simulation.

Scintillator light is readout by WLS-fibers embedded in the spiral grooves in the tiles providing high efficiency and uniformity of the light collection over the scintillator tiles within a few percent. WLS fibers Y-11(200) with double cladding and a 1 mm diameter were used for the FHCal assembling. One end of the WLS-fiber inside the scintillator grove is mirrored by silver paint, that improves the light collection by about 30%. WLS-fibers from each of 6 consecutive scintillator tiles are collected together in the optical connector at the end of the module and polished to improve the optical contact with the photodetector. This light readout scheme provides the module longitudinal segmentation in 7 sections that compensates the nonuniformity of the light collection along the module caused by different lengths of the WLS-fibers. As a consequence, 7 optical connectors and the same number of photodetectors are positioned at the rear side of each module.

All 42 layers of lead/scintillator sandwiches of the FHCal module are loaded into the box made of 0.5 mm stainless steel sheet and tied together in one block with a length of about 90 cm (4 nuclear interaction lengths) by a 0.5 mm stainless steel tape. After assembling the module is covered by another similar stainless steel box and these two up and down boxes are spot-welded providing a mechanically stable construction. The weight of each module is about 200 kg.

Readout of the FHCal

As mentioned above, 7 optical connectors at the rear side of each module are viewed by compacts photodetectors. FHCal requires a specific type of photodetectors with high internal gain, immunity to magnetic fields and without nuclear counter effect. Silicon photomultipliers, SiPMs, is an optimum choice for this case. Hamamatsu MPPC S14160-3010PS with a pixel size of 10x10 μm^2 were selected to ensure a high dynamic range of detected energies. The board with 7 SiPMs is shown in Fig.2, left. The Front-End-Electronics includes an amplifier and a shaper with differential output signals that increases the signal length t about 0.2 μs. This long signal is digitized by the pipe-line 64-channel 62.5 MS/s ADC64 board manufactured by the Dubna company AFI Electronics, Fig.2, right.

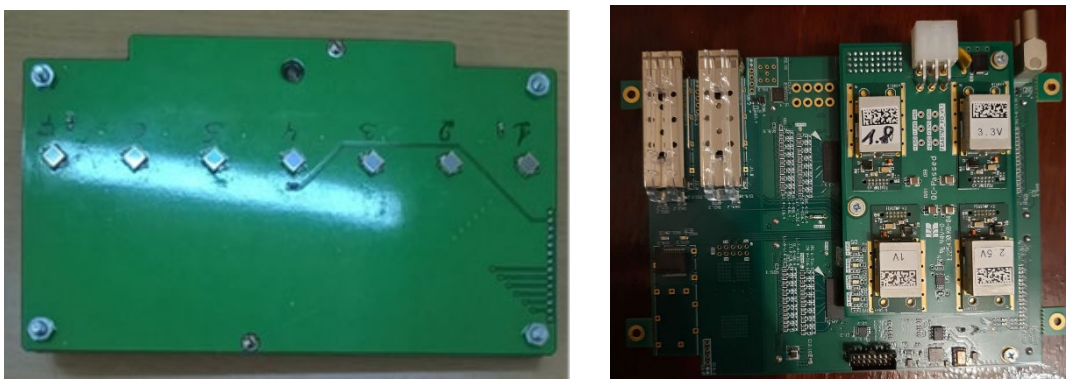

Fig.2. Photo of FHCal readout elements. Left - the board with SiPM. Right – analog-to-digital convertor ADC64.

Full readout scheme for one FHCal arm is presented in Fig.3. The main components of the readout system are: Front-End-Electronics (FEE) placed at the rear sides of modules; 5 ADC boxes located at the lateral sides of FHCal support frame; power suppliers and DAQ installed at electronic platform. A few types of cables including the coaxial and optical ones with the length of about 20 m would transmit the signals from ADCs to DAQ and trigger modules at the electronic platform.

The magnet poles with installed FHCal arms can be moved frequently outside the superconductive solenoid to access the inner volume of magnet for assembling and serving the sub-detectors, especially at the initial stage of MPD integration. Therefore, it is necessary to detach the cables from FHCal readout system. For this purpose, a patch-panel will be installed at the FHCal support frame that connects the cables from electronic platform and ones from ADCs.

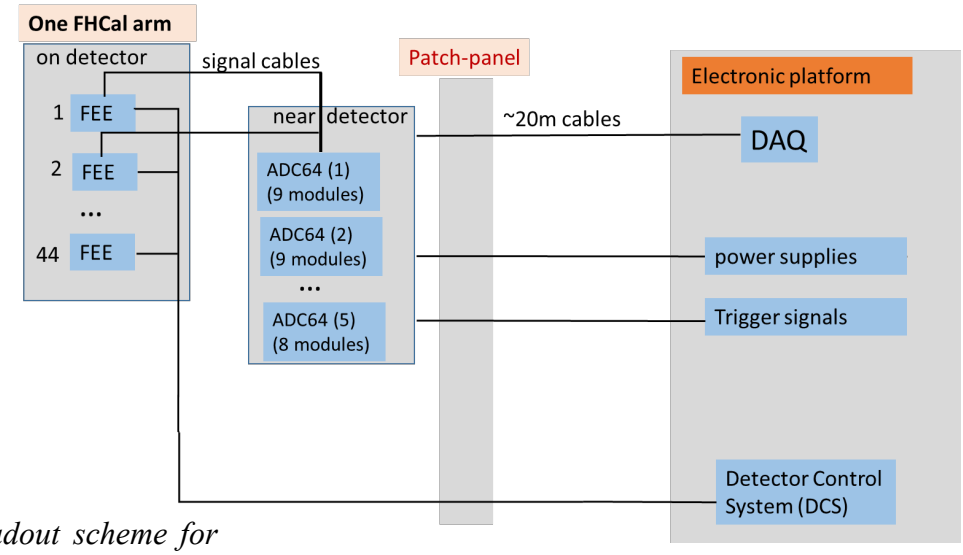

Fig.3. Readout scheme for one FHCal arm.

FHCal Detector Control System (DCS)

The DCS for FHCal should provide fast and stable access to all parameters of the FHCal FEE boards. These boards include precise HV power supplies and calibrating LED pulser, managed by two microcontrollers with common serial RS-485 bus. The HV microcontroller controls several parameters: status, set and measured channel voltage, set or measured common base voltage, HV ramp time, HV ramp status and temperature of SiPMs. The LED controller provides status, the LED pulse frequency and amplitude.

The electronic boards are connected with a common RS-485 bus to the Control Box Unit (CBU). Since each module has two transceivers one can connect up to 64 electronic boards (FHCal modules) to the CBU. FHCal setup will use two CBUs. The CBUs have a possibility to connect to LAN and be controlled directly by one DCS PC. The connection diagram for DCS is shown in Fig.4.

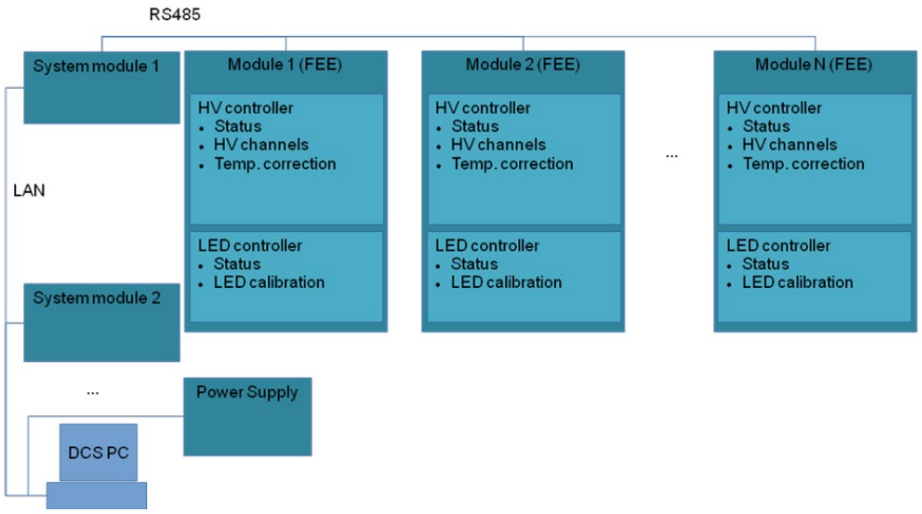

Fig.4. Connection diagram for FHCal DCS.

The DCS functions also include online temperature correction, logging parameters to database, and should have a fast connection with multiple devices. All detector parts have capabilities to read or write the controller registers available on the bus. The registers can be described in the configuration files.

FHCal energy calibration

Hadronic showers from free spectators deposit the visible energy in the range from a few MeV to hundreds of MeV in the scintillators of FHCal longitudinal sections. It is necessary to have a calibration of the calorimeter in this energy range. The FHCal position in MPD setup is fixed and does not allow the beam scan of the calorimeter modules. Therefore, the only option for the energy calibration is the use of cosmic muons. As measured in tests with muon beams, the spectrum of horizontal muons has a clear MPV (Maximum Probability Value) peak corresponding to energy deposition of about 5 MeV in the scintillators of one longitudinal section. Unlike the beam, cosmic muons have a wide range of the entry angles into calorimeter and the muon pass lengths in the scintillators depend strongly on the geometry of the muon tracks. As a consequence, the muon energy deposition in longitudinal sections of FHCal modules has a broad spectrum.

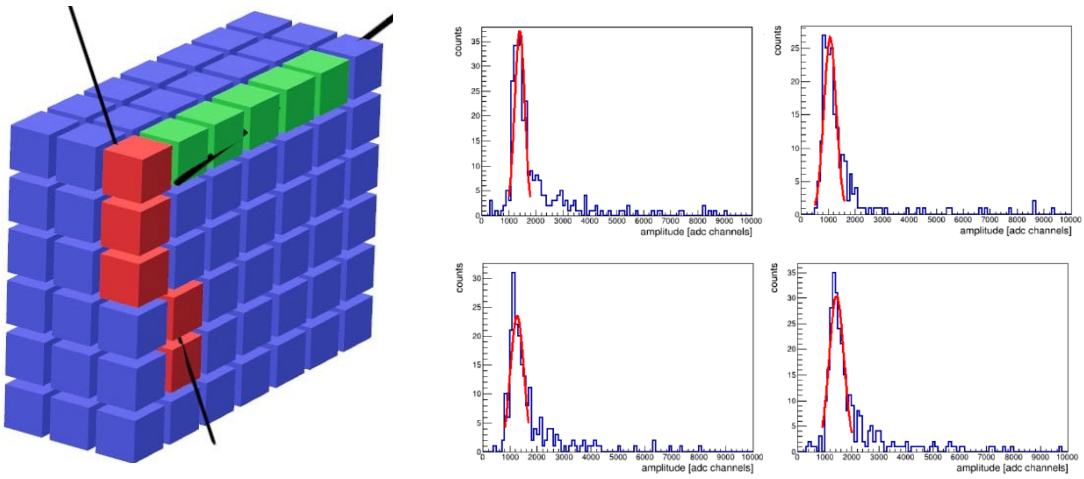

Fig.5 Left - the scheme of FHCal modules array, used for the test of cosmic muon calibration. Right panel presents the muon's amplitude spectra in scintillators of a single longitudinal section for horizontal tracks of cosmic muons.

The problem can be solved in two ways. First, one can collect cosmic muons with horizontal tracks that pass all 7 longitudinal section of the module, see Fig.5, left. The obtained amplitude spectra in the sections are shown in Fig.6, right. One can see narrow peaks corresponding to 5 MeV energy depositions. Unfortunately, this method requires almost one week of data acquisition. Therefore, another method of energy calibration with all-angles tracks of muons was elaborated with the subsequent correction of energy deposition. The amplitude correction to the pass length in scintillators relies on the restoration of the muon tracks geometry

with the following method. Each section of FHCal module can be regarded as a single cell of the track detector with the sizes 15x15x12 cm^3, where the transverse dimensions of the module and the length of the longitudinal section are taken into account. In spite of large cell size, it allows the reconstruction of the track geometry in case of muon detection by a few FHCal modules. For this purpose, the array of the modules was assembled, see Fig.5, left. The track can be reconstructed if muon passes a few longitudinal sections in different modules of an assembled array. And simultaneously the pass lengths of muon are identified in these sections with some accuracy. The subsequent pass length correction of amplitudes creates the peak-prominent structure in the spectrum. The peak position in the amplitude spectrum corresponds to 5 MeV of deposited energy and is used for the energy calibration.

Integration of FHCal to MPD experiment

All 90 FHCal modules were produced at INR RAS and shipped to JINR in the end of 2023. In parallel, the assembling table and support frames for FHCal installation in magnet poles were manufactured at JINR in 2024. At present, the support frames are installed into magnet poles.

First arm of FHCal calorimeter was assembled at floor in MPD experimental hall in the beginning of 2024, see Fig.6, left. After assembling at the table, the FHCal arm was installed in magnet pole (Fig.6, right). At present, first FHCal arm is equipped by the Front-End-Electronics.

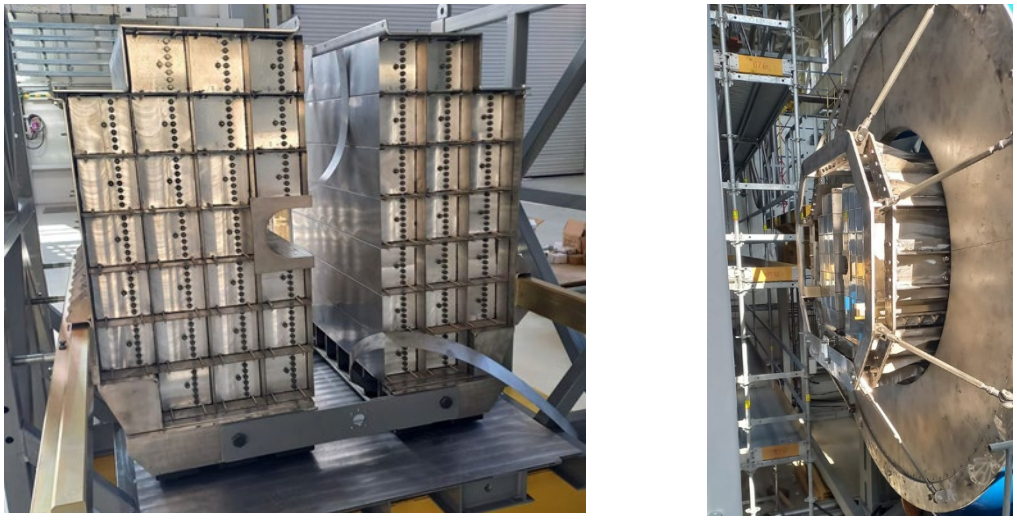

Fig.6 Left – Assembling of one FHCal arm at floor. Right – FHCal arm is installed in magnet pole.

Next stages of FHCal integration include: mounting and installation of second FHCal arm, assembling and tests of readout and control systems, cabling, manufacturing of patch-panel and development of ADC cooling system. At the final stage the energy calibration of FHCal modules with cosmic muons will be performed. According to current schedule, full FHCal integration to MPD experimental setup will be finished in the middle of 2025.

Publications:

1. A. Ivashkin, et al., Amplitude parameters of modules for hadron calorimeter at MPD/NICA, JINST 15 (2020) 06, C06044
DOI: 10.1088/1748-0221/15/06/C06044

2. V. Volkov, et al., Approaches in centrality measurements of heavy-ion collisions with forward calorimeters at MPD/NICA facility, 2020, J. Phys.: Conf. Ser. **1690**, 012103
DOI:10.1088/1742-6596/1690/1/012103

3. A. Ivashkin, et al., Measurements of Spectators with Forward Hadron Calorimeter in MPD/NICA Experiment, Phys.Part.Nucl. 52 (2021) 4, 578-583
DOI: 10.1134/S1063779621040298

4. V. Volkov, et al., Application of FHCal for Heavy-Ion Collision Centrality Determination in MPD/NICA Experiment, Particles 4 (2021) 2, 236-240
DOI: 10.3390/particles4020022

5. A. Strizhak, Reconstruction of energy and collision point of heavy ions with forward hadron calorimeter at MPD setup, AIP Conference Proceedings 2377, 030015 (2021).
DOI: 10.1063/5.0063348

6. A Izvestnyy, et al., Performance of Forward Hadron Calorimeter at MPD/NICA, 2020, J. Phys.: Conf. Ser. 1667 012016.

DOI: 10.1088/1742-6596/1667/1/012016

7. V Volkov, et al, Approaches in centrality measurements of heavy-ion collisions with forward calorimeters at MPD/NICA facility, 2020, J. Phys.: Conf. Ser. 1690 012103.

DOI: 10.1088/1742-6596/1690/1/012103

8. O Petukhov and S Morozov, Development of Detector Control System (DCS) for forward hadron calorimeters in the BM@N and the MPD experiments, 2020, J. Phys.: Conf. Ser. 1690 012063

DOI: 10.1088/1742-6596/1690/1/012063

Conferences:

1. A. Strizhak, Reconstruction of energy and heavy ion collision point at FHCal (MPD). The XXIV International Scientific Conference of Young Scientists and Specialists (AYSS-2020), JINR, Dubna, Russia

2. S. Musin, Centrality determination method based on observables from TPC and FHCal at MPD/NICA, he XXVth International Baldin Seminar on High Energy Physics Problems "Relativistic Nuclear Physics and Quantum Chromodynamics", 2023, JINR, Dubna, Russia

3. A. Strizhak, Determination of the ion collision point in the MPD/NICA facility using the Forward Hadron Calorimeter, 2020, 63rd MIPT scientific conference, MIPT, Moscow, Russia

4. A. Strizhak, Energy calibration of Forward Hadron Calorimeter at MPD with cosmic muons. The XXVth International Baldin Seminar on High Energy Physics Problems "Relativistic Nuclear Physics and Quantum Chromodynamics", 2023, JINR, Dubna, Russia

5. A. Baranov and A. Strizhak, Status of Forward Hadron Calorimeter at MPD/NICA. The 28th International Scientific Conference of Young Scientists and Specialists (AYSS-2024), JINR, Dubna, Russia

3.7 Electromagnetic Calorimeter

Electromagnetic barrel calorimeter (ECal) provides an access to the electromagnetic probes such as direct photons and lepton pairs, decays of neutral mesons, and significantly improves electron/hadron separation.

3.7.1 Design of the ECal

Large-sized (6-meters-long and 4.5-meters in diameter) electromagnetic barrel calorimeter (ECal) is an important part of the Multy-Purpose Detector (MPD) at heavy-ion NICA collider that covers the central pseudorapidity region of $|\eta|<1.2$. ECal is optimized to provide precise spatial and energy measurements for photons and electrons in the energy range from about 40 MeV to 2-3 GeV. To deal with a high multiplicity of secondary particles from central Au-Au collisions, ECal has a fine segmentation and consists of 38400 cells ("towers"). Taking all requirements (high energy resolution, large enough distance to the vertex, small Moliere radius, ability to work in the high magnetic field, high time resolution, resistance to radiation, and reasonable price) into consideration, a "shashlyk"-type electromagnetic calorimeter was selected. Each "tower" has a sandwich structure of 210 polystyrene scintillators and 210 lead plates with 16 wave length shifting (WLS) fibers that penetrate the plates to collect the scintillation light; the thickness of each scintillator plate is 1.5 mm, and the thickness of the lead plate is 0.3 mm (Fig. 3.7.1). Monte-Carlo (MC) simulations show that such a proportion of scintillators and lead converters provides the sampling fraction of about 34-39% (depending on energy), and results into relatively small statistical term and a good energy resolution in the energy range below 1 GeV. The limited space inside the MPD magnet leads to the limited ECal thickness just above 11 X_0, and the correspondent visible energy leak from the backend of the calorimeter. However, the leak does not exceed 10-12% in the ECal energy range.

Based on the MC studies, a decision was made to build the calorimeter with the projective geometry (where the towers are inclined along the beam axis to keep the tower axis to be consistent with the direct view of the beams intersection region). The main advantages of this design are a reduction of dead zones, an increase in the detector efficiency, an improvement of linearity, and an energy resolution of the calorimeter measurements in conditions of high multiplicity of secondary particles.

3.7.2 Production of Modules

ECal module consists of 16 towers that are glued together (Fig. 3.7.1). The geometry of each module depends on the module Z-coordinate (beam direction) location with respect to the beams interception point. In total, the ECal will contain 2,400 modules of 8 different types. The production of the ECal modules is divided between Russian and Chinese facilities.

For better light collection, the lead plates are coated with white glossy polyester powder paint Element (Turkey). A technology for applying a reflective coating was developed and implemented at two enterprises in the Moscow region. For the same purpose, glue-paint for gluing the towers of modules was developed and its production was established. Tests of the glue-paint (as glue) were carried out in a certified laboratory to test composite materials of the Dubna State University.

The tests showed that the gluing of 16 towers in one module has a sufficient margin of safety for their installation already in half-sectors.

More than 8 million scintillation plates were manufactured at Polipack company in Dubna and Uniplast company in Vladimir, which is enough for Ecal. Polipack produced a full set of module tower tightening caps and WLS tower assembly crowns in one bundle for the entire Ecal. The required number of lead plates was manufactured at IHEP (Protvino) and Armul company (Moscow Region).

Originally, we used Kuraray Y11 (200) WLS fibers with a diameter of 1.2 mm for collecting light. Later, due to sanctions, these fibers were replaced after additional studies with OSL 8 fibers with similar characteristics, manufactured by the Optical Polymer Fiber Technology Center (Russia, Tver). The full volume of Kuraray WLS fibers for all Chinese and 800 Russian-made modules was purchased, and the production of WLS fibers for the remaining modules is in progress.

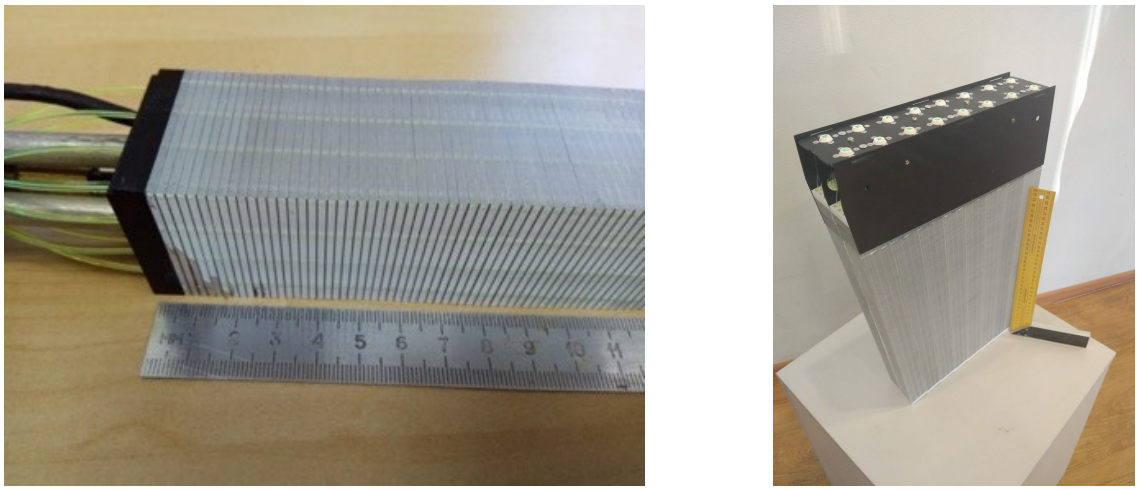

Fig. 3.7.1. Left panel: structure of ECal tower. Right panel: Ecal module.

3.7.3 Front-End Electronics

Front-end electronics will be located directly on the calorimeter. For each module type, front-end boards (Fig. 3.7.2) with 16 silicon photomultipliers (6×6 mm^2 Hamamatsu S13360-6025PE MPPC with a peak sensitivity at a wavelength of 450 nm), preamplifiers and slow-control electronics (that controls the temperature and makes the corresponding correction of about 45 mV/degree on photodetectors supply voltage) were developed in JINR. They were manufactured in Russia (1200 pieces) and China (1200 pieces).

To calibrate the operation voltage calibration for each photodetector, the SiPMs on the front-end boards were illuminated with short pulses of 300-500 nm light from an LED generator. During the calibration, the photodetectors' voltages were changed from 56 V to 64 V (with a step of 0.2 V) using HVSys SM-G761 controllers. After analysis of the spectra at different voltages, the optimum voltage was chosen to provide maximal photodetector efficiency with minimal noise contribution. The stand allows three boards to be calibrated simultaneously. Currently, 1622 front-end boards have been calibrated. We expect that about 2000 boards will be calibrated before the end of 2024. Given the current pace (from 10 to 30 boards per day), the remaining 400 boards will be calibrated before April 2025.

Fig. 3.7.2. Left panel: front-end boards. Right panel: ADC boards ready for installation.

To digitize the signals, the JINR-designed 64-channel 14-bit 62.5 MS/s Pipelined ADC64ECAL boards were used (Fig. 3.7.2). These boards have a signal processing core and an Ethernet interface with the ability to synchronize time over the White Rabbit network. The data readout, triggering, and synchronization function is performed over a single fiber-optic communication channel. An additional QSFP connector can be used to provide an external clock for high-precision measurements, as well as triggering and data readout channels.

The ADCs are placed in heat-insulated boxes to minimize influence on the photodetectors; one box accommodates 4 ADC boards. The boxes also provide the necessary communications for operation (viz., cables and optic fibers) and cooling systems. On the front side of the box, there is a patch panel with connectors for connecting cables and cooling air/water. All 600 ADC boards we need are purchased. Currently, 135 boxes are assembled, and the remaining 15 boxes are expected to be delivered. With the box assembly production rate of 1 piece per two days, we plan to complete the assembly of all boxes within a month after the delivery of the missing elements.

3.7.4 Test of Modules with Cosmic Muons

A preliminary calibration of the module towers' response was performed using minimally ionizing particles (cosmic muons). Originally, the calibration area consisted of four light-tight tents; each can simultaneously test 8 modules of two types. The total calibration rate is 32 modules per day. Each tent is equipped with two power supplies (Mean Well MDR-60-12); a circuit breaker (ABB SH202L C6); two ADC boards (ADC64ECAL), one controller (HVSys SM-G761), and 8 pre-calibrated front-end boards. The selection of cosmic muons in the module was organized in "self-triggering mode": in every 8-tower column, two outer towers are used for the trigger coincidence, while the towers in between are under the test. For the calibration of the outer towers, the close neighbor towers are used as trigger ones. Fig. 3.7.3 shows peak values of ADC integral distributions for towers built by different manufacturers. Towers from different manufacturers show a noticeable difference in distribution, which indicates differences in the tower responses from slightly different module assembling techniques (probably).

Currently, 1499 modules have been tested. Due to working conditions, two test tents were dismantled. The plan is to complete the testing by March 2025, given the testing pace (about 16 modules per day).

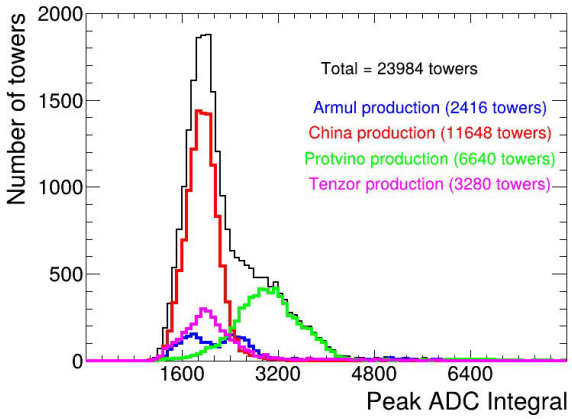

Fig. 3.7.3. Results of module tests with cosmic muons.

3.7.5 Test of Modules with Electron Beams

Tests of the single prototype modules were performed with electron beams at DESY (Hamburg, Germany) and Lebedev Physics Institute of the Russian Academy of Science (Troitsk, Russia). For the measurements with electron beam energies above 1 GeV at DESY, a visible deviation from linearity for the ECal response was observed. It was found that this deviation is connected mostly with the signal saturation because of the limited number of pixels in the MPPC; the correction of this effect restores the linearity.

An energy resolution of the single ECal module was measured recently with a relatively low-energy electron beam in Troitsk. The obtained data (shown in red in Fig. 3.7.4) are in good agreement with the results of Monte-Carlo simulations for a single module (shown in blue in Fig. 3.7.4). The same Monte-Carlo simulation made with whole calorimeter allows to make a preliminary estimation of the expected energy resolution of the ECal:

$$\Delta E/E \approx \frac{3.0\%}{\sqrt{E(GeV)}} \oplus 2.4\%$$

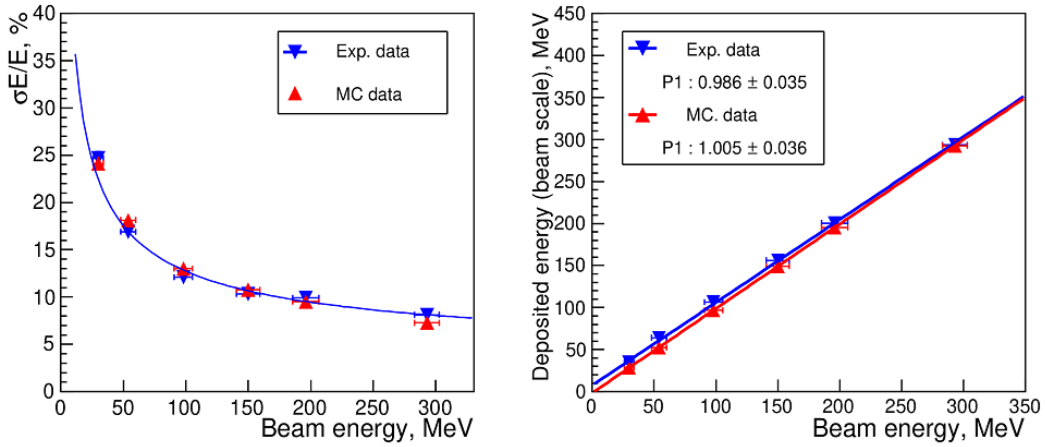

Fig. 3.7.4. Energy resolution (left) and linearity (right) from modules tests with electron beam in Troitsk.

3.7.6 Production of Half-Sectors

From a geometrical point of view, the ECal is divided into 25 sectors or 50 half-sectors; each half-sector contains 6×8 = 48 modules of 8 different types. These modules are located in the half-sector container (basket) made of fiberglass material. The basket is 3.12 m long and 0.56×0.56 m^2 in cross-section. The basket walls are 6 mm thick and are coated on the outside with a special compound to remove electrostatics and to provide better sliding during the installation of the basket in the MPD power frame. The rigidity of the container was tested, and it was found strong enough to provide deformation of less than 0.5 mm under a full half-sector load of about 1.5 tons. Fig. 3.7.6 shows a photo of the basket with glued modules and partially installed electronics, as well as a schematic view of the Ecal supporting structure. to this date, TsNIISM company (Khotkovo, Moscow Region) has supplied a full set of baskets (51 pcs.) under the contract.

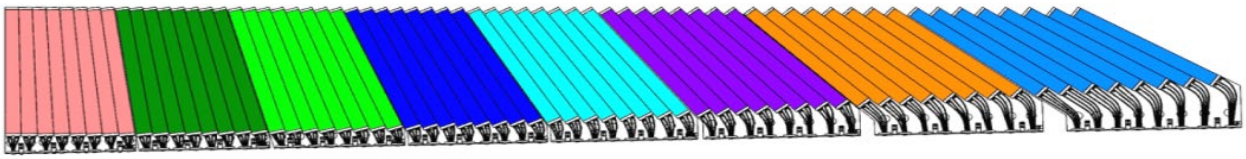

Fig. 3.7.5. Layout of the modules in the half-sector.

After the procedure of checking the modules received from the manufacturers for the quality of gluing the towers and geometric parameters according to the design documentation, and testing of the modules with cosmic muons, 16 modules of 8 types were glued into a cluster using a device created for this purpose. In the last stage, 3 clusters are glued into a half-sector using a stand designed and manufactured by Polipak. For this operation, a special glue developed for carbon and fiberglass by TsNIISM is used. Fig. 3.7.5 shows the layout of the modules in the half-sector.

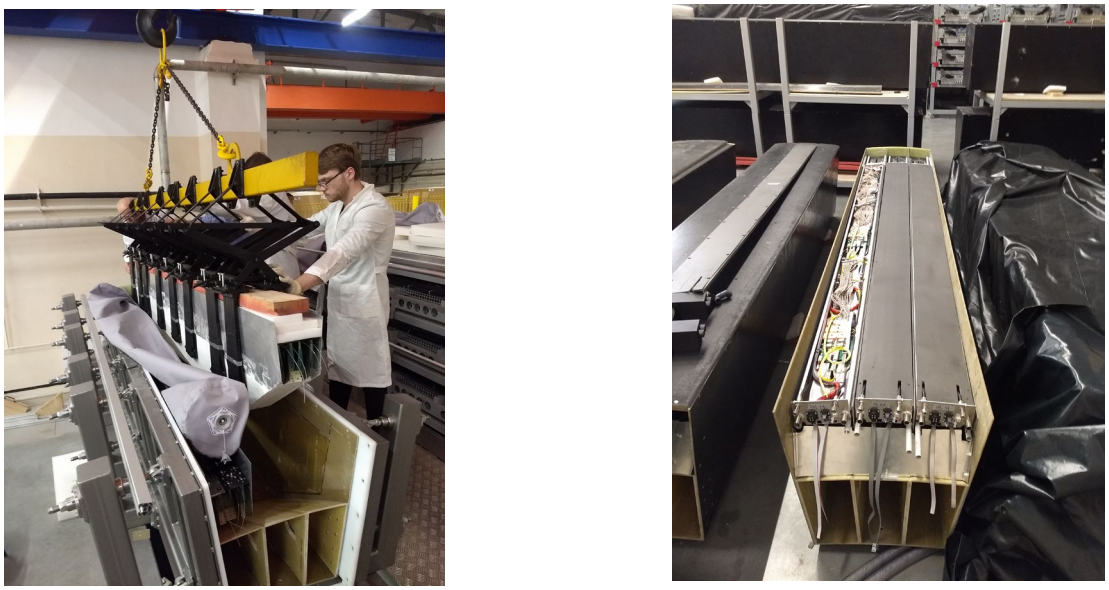

Fig. 3.7.6. Gluing of the clusters into the basket (left) and assembled half-sector (right).

Almost 800 modules were manufactured at 4 universities in China, and 1,320 modules were manufactured in Russia (IHEP, Armul, and Tensor). By the end of 2024, all these modules will be glued into 40 half-sectors, which is 80% of the total number of towers in Ecal. According to the

plan, the remaining 10 half-sectors will be manufactured in 2025. Some contracts to manufacture missing components and modules by Russian manufacturers have been signed.

3.7.7 ECal Cooling Systems

The heat production is estimated at 180 W per half-sector (or about 9 kW for the whole ECal), and two independent cooling systems are developed to evacuate the heat from the boxes. The water-cooling system removes heat from the ADC and creates a stable temperature using copper tubes and water blocks for the uninterrupted correct operation of the ADC. Each ADC has a maximum power of 15 W, and it is equipped with a copper water block that is connected to a system of copper tubes for supplying cooling water. The permissible temperature of the ADC is no more than 45 °C is controlled by a built-in temperature sensor. All components for water-cooling systems are purchased (Fig. 3.7.7), and 135 out of 150 water-cooling systems are installed in the heat-insulated boxes and tested for leaks using a vacuum stand. The delivery of the 15 remaining boxes is expected in November 2024, and the installation of water-cooling systems is expected before the end of 2024.

Fig. 3.7.7. Water-cooling systems ready for installation.

The air-cooling system is developed to evacuate the heat generated by the ECal electronics from the half-sector volumes (both inside and outside the heat-insulated boxes). The main air-cooling system evacuates the heat near the front-end boards (viz., SiPMs). The reserve air-cooling system is to remove the heat from the volume of nearby ADCs (in addition to the water-cooling system). For the operation of the system, an airflow of 30 m^3 per hour per half-sector is needed. Air-cooling systems for both SiPMs and ADCs provided stable operation without the water cooling system during a few-month cosmics run. Currently, the manufacturing and installation of 12 (out of 50) air-cooling systems next to the front-end boards are finished. Needed materials have been purchased, the installation is carried out as the baskets are assembled. Manufacturing and installation of 120 (out of 150) air-cooling systems in the heat-insulated are finished. The materials have been purchased, the installation is carried out as the ADC boxes are assembled. The air collectors are assembled and will be installed and tested as the finished baskets are tested on the stand.

3.7.8 ECal Stability Control System

The electromagnetic calorimeter is controlled and managed using high and low-voltage supply control systems, as well as a system for monitoring the operation of photodetectors and readout electronics. The latter system does not provide accurate calibration of the detectors and electronics; its tasks are limited to monitoring the overall performance of the calorimeter elements and tracking possible significant changes in the detector characteristics. Based on these tasks and taking into account the expected energy resolution of the calorimeter, a monitoring accuracy of 1-2% was considered sufficient. The need to monitor a significant number of calorimeter cells imposes additional requirements: the monitoring system must be sufficiently simple and reliable, and the cost of monitoring each calorimeter cell (readout electronics channel) must not be too high.

The monitoring split system based on the SOF-2 side-glow fiber was considered. The side-glow fiber is capable of emitting light in transverse directions. A system design was developed, where the light from one LED is distributed to 256 towers, i.e. one cluster, which corresponds to one box of electronics for reading signals from photodetectors. SOF-2 side-emitting fibers with a diameter of 2 mm and a length of ~3 m are placed in polycarbonate tubes with an internal diameter of 3 mm and a wall thickness of 1 mm. To couple the fibers with the LED, a special holder was designed and manufactured on a 3-D printer, to one side of which an LED with a driver and a monitor photodiode manufactured by HVSYS was attached, and four side-emitting fibers were attached to the other side. Each fiber distributes light to 64 bundles of WLS fibers, as shown in Fig. 3.7.8.

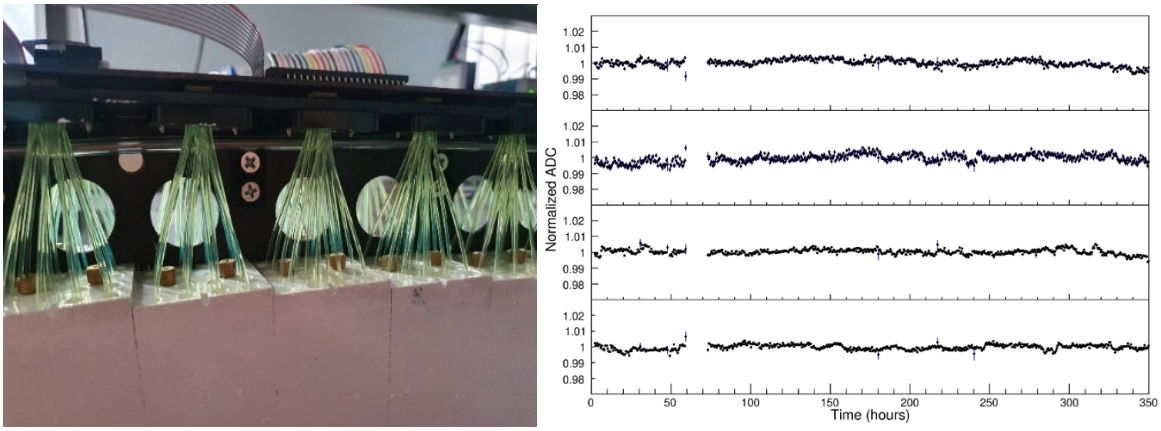

Fig. 3.7.8. Left panel: distribution of the light to WLS fibers. Right panel: results of long-tern stability test for a few channels.

The long-term stability of the prototype monitoring system was investigated. The measurements for four channels lasted 350 hours, the temperature compensation of the photodetector signals was enabled, air cooling of the electronics was used, and normalization to the photodiode signal was not performed. The LED firing frequency was 0.1 Hz. The measurement results are shown in Fig. 3.7.8. Each point in the figure represents the result of averaging the signals from the ADC for 30 minutes. It is evident that the signal spread was less than 1% in absolute value, and a break in operation lasting approximately 13 hours did not have a noticeable effect on the stability of the calorimeter monitoring system.

3.7.9 ECal Integration

Originally, the electromagnetic calorimeter was planned as a self-supporting structure, where each sector contributes as a power element to the whole structure. However, after splitting the ECal modules production between Russian and Chinese sites (with different time schedules), the ability to install and re-install calorimeter sectors (half-sectors) without the whole calorimeter and MPD dismantle was requested. To meet this demand, we will use a special support frame (about 8 meters long and about 4.5 meters in diameter) made of carbon-fiber composite material that can hold the whole load from MPD detectors without support from ECal sectors (Fig. 3.7.9). This frame consists of inner (20-mm-thick) and outer (15-mm-thick) cylindrical shells with 25 bulkheads (10-mm-thick) in between them to form 25 cells for calorimeter sectors installation. Rigidity calculations for the simplified frame model were performed and demonstrate that the planned total load of 120 tons will cause maximum frame deformations of about 2-3 mm meets our demand to have deformations below 5 mm to keep the ability of installation and re-installation of ECal half-sectors. Strength calculations ensure the frame's ability to hold the load about 10 times higher than our maximal expectations, and durability calculations and tests assure 15-year frame operation. In March 2023, the frame was delivered to JINR and will be installed into the MPD magnet after finishing the magnet mapping.

To install ECal half-sectors into the frame, the special tool was designed and produced (Fig. 3.7.9). It allows precise positioning and rotations of 1.5-tons half-sector in 3D space as well as low-friction movement of the half-sector along the tool axis. The tool was delivered to JINR in October 2024 for final setting.

Fig. 3.7.9. Left panel: MPD power frame. Right panel: the tool for half-sectors installation.

3.7.10 Reference

[1] ECal/MPD Collaboration JINR "TDR of the Electromagnetic calorimeter (ECal)" 2018, Rev. 3.6.

[2] I. Tyapkin et al., "NICA/MPD Electromagnetic Calorimeter based on Multipixel Avalanche Photodetector", PoS PhotoDet2015 (2016) 053.

[3] Basylev, S. et al., Projective geometry for the NICA/MPD Electromagnetic Calorimeter. Journal of Instrumentation, V.13, Is. 02, pp. C02030 (2018); doi:13(02):C02030-C02030.

[4] Durum et al., Optimization of a light collection in the Shashlyk-type electromagnetic calorimeter with projective geometry for the NICA/MPD experiment. EPJ Web Conf. 222 (2019) 02007, DOI: 10.1051/epjconf/201922202007

3.8 The MPD thin-wall beampipe

The beam pipe of the MPD is nine meters long thin-wall UHV compatible beampipe depicted in Fig. 3.8.1. Manufacturing of the MPD beampipe is a very complex proccess. Required vacuum inside of the pipe have to be better then 10^{-10} torr. We consider the beampipe which made of beryllium on the central part, in the interaction region and aluminum on the edges. The typical minimal wall thickness is 1 mm both for beryllium and aluminum parts. Russian company Composit – Beryllium Institute produced two samples of beryllium part 1700 mm in length.

The outer parts of the beam pipe will be made of special alloy of aluminum.

On the first time in order to get experience we are planning to produce completely aluminum beam pipe the same geometry as a basic one.

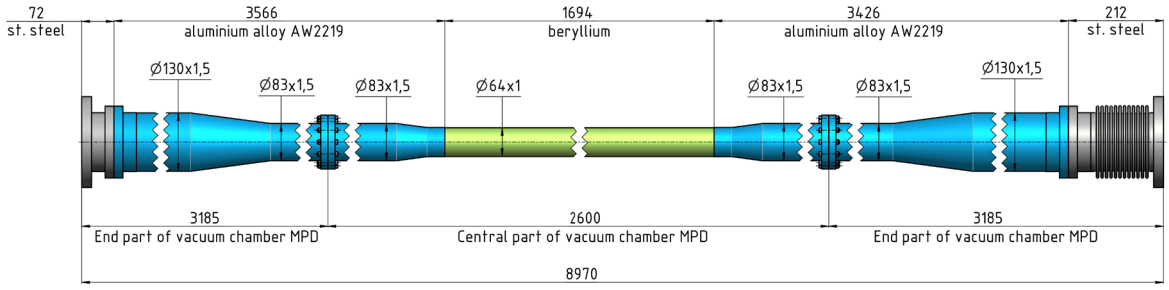

Fig. 3.8.1. A tentative design of the MPD beam pipe. Absent is any indication of the vacuum equipment at the rare ends of the beampipe. According to the integration scenario the beampipe is baked at the vacuum stand and filled in with dry Neon and only then is shipped to the assembly stand c/o the MPD ITS team.

3.9 MPD Data Acquisition (DAQ) system and computer cluster

The core function of the DAQ system is realization of data transfer from the detector to the storage system. It includes the data flow from readout electronics to the First Level Processor (FLP) fabric, to the Event Building (EB), High Level Trigger (HLT) and to the Storage System. Main DAQ components are data transfer networks, data processing servers, online storage system, software packages, network communication protocols and data formats. Readout electronics interface, Clock and time synchronization (Timing) System, Trigger System are also included in MPD DAQ system.

3.9.1 Data Readout Electronics

TOF detector will be readout using 2 types of modules – TDC72VHL and TTVXS (figure 3.9.1). TDC72VHL is a 72 channels timestamping time-to-digital converterw with typical accuracy of 20 ps per channel. Hit timestamps are kept for 52 μs in ring type memory. The total trigger latency should not exceed this value. TTVXS module is a Time and Trigger Unit (TTU). This module distribute trigger and synchronous clock to TDC72VHL modules installed in the same VXS crate. Also TTVXS collects data from TDC72VHL modules and trasmits this data to event building system via 10G Ethernet. For TOF detector 14 VXS crates will be used.

FFD DAQ is similar to TOF DAQ, but it uses 1 VXS crate and 4 TDC72VHL per crate.

In total 200 TDC72VHL and 15 TTVXS modules are needed to readout TOF and FFD detectors. Produced 219 TDC72VHL modules and 20 TTVXS modules. TTVXS modules will be used in trigger distribution.

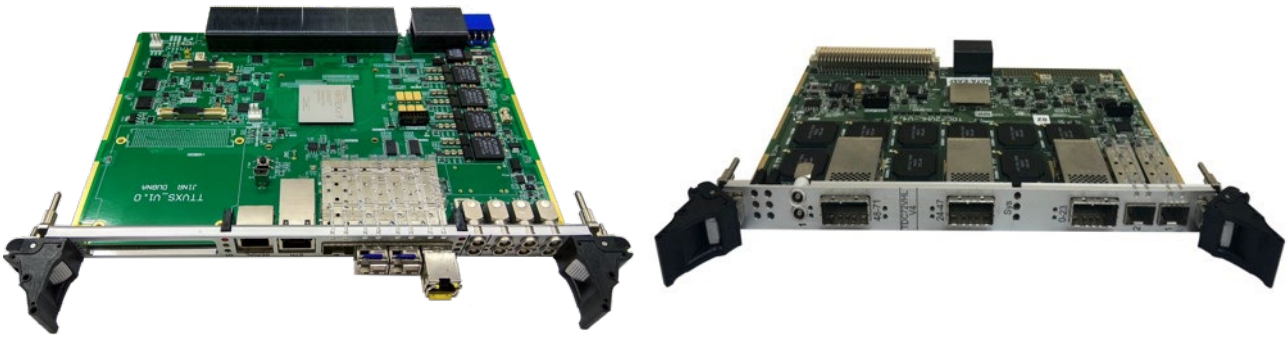

Fig 3.9.1. TTVXS (left) and TDC72VHL (right) modules

For ECAL detector readout ADC64ECAL electronic modules were designed and produced (figure 3.9.2). ADC64ECAL is a 64 channels ADC module, with 14 bits quantization and 62.5 MSPS discretization. For synchronization and trigger distribution module CRU16 was designed (figure 3.9.3). It's capable to synchronize up to 16 modules, provide a trigger signals and collect the data form them. All collected data are transmitting to the switch, using 40 Gbps optical interface.

To readout ECAL detector 600 ADC64ECAL and 38 CRU16 modules are needed.

4 ADC64Ecal modules will be placed inside the one box (figure 3.9.4). Custom Liquid Cooling System (LCS) and internal communications (power, data cables and etc.) are produced and delivered. 130 boxes are fully assembled and vacuum checked. 20 more boxes are expected to be assembled by the end of 2024.

FHCAL detector will be readout using 10 ADC64S2 modules (figure 3.9.2). It is a 64 channels ADC module, with 14 bits quantization and 62.5 MSPS discretization. Trigger and time synchronization will be done via 2 CRU16 modules.

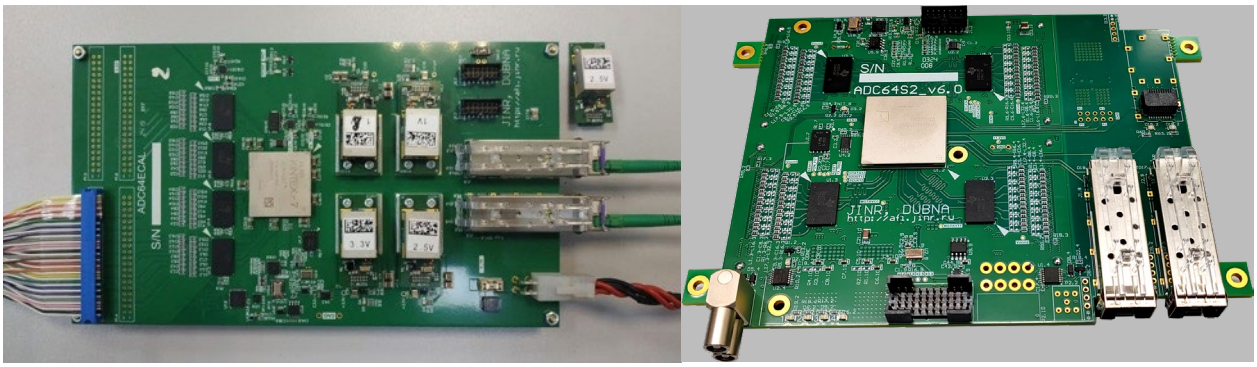

Fig. 3.9.2. ADC64ECal (left) and ADC64S2 (right) electronic modules.

Fig. 3.9.3. CRU16 electronic module.

All electronic modules toreadout ECAL and FHCAL are produsedand tested: 630 ADC64ECAL (105%), 12 ADC64S2 (120%) and 45 CRU16 (112%). Some CRU16 modules will be used for trigger distribution.

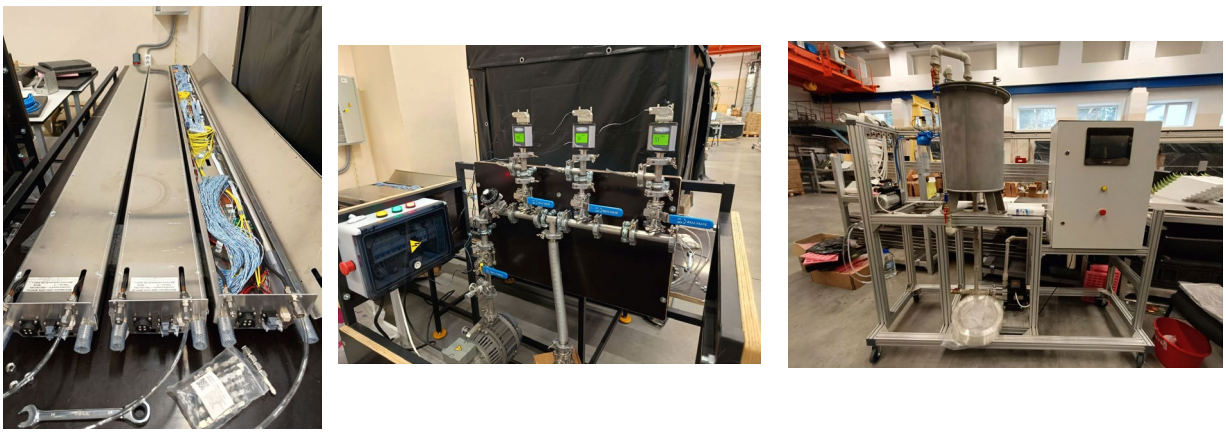

Fig. 3.9.4. Box for ECAL electronics (left), air vacuum test stand for ECAL LCS (center), LCS test stand (right).

CRU16 (Fig. 3.9.3, right) is a common readout unit with White Rabbit support. It's capable to synchronize up to 16 modules, provide a trigger signals and collect the data form them. All

collected data are transmitting to the switch, using 40 Gbps optical interface. All 45 CRU16 boards are produced and tested by the end of 2023.

3.9.2 MPD Trigger Electronics

Trigger system process information from trigger detectors and produced readout triggers for all MPD. There are 4 trigger detectors: FFD, TOF, Luminosity and FHCAL. To prevent loss of tracking information from TPC the time to process trigger signals from trigger detectors has to be minimized. Full trigger latency expected to be about 1us.

FHCAL trigger processed on the ADC64S2 DRE board. All 10 board will be used for trigger system. For TOF and Luminosity detectors new trigger processing modules were designed – TLU40LVDS and TLU16SFP (figure 3.9.5).

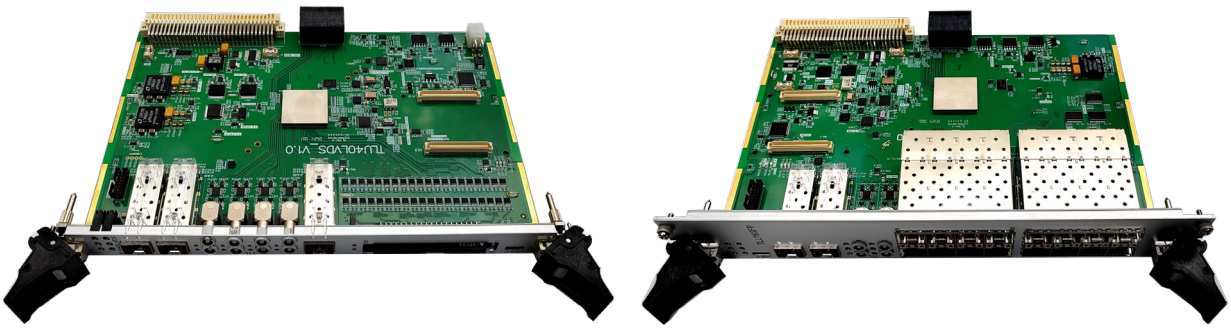

Fig. 3.9.5. TLU40LVDS (left) and TLU16SFP (right).

FFD group designed their own trigger electronics and provide 3 trigger signals to central trigger module.

Electronic module UT24VE will be used as central trigger module (figure 3.9.6). Central trigger module receives 3 trigger signals from FFD, 1 trigger signal from TOF, 1 trigger signal from Luminosity and 10 trigger signals from FHCAL.

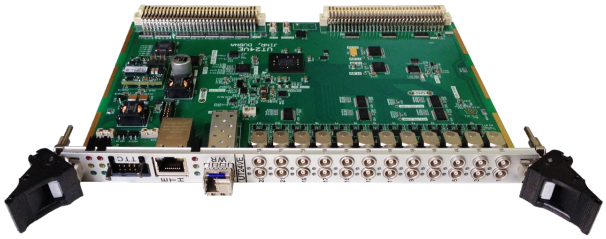

Fig. 3.9.6. UT24VE – central trigger module.

3.9.3 MPD DAQ network

Networking devices and DAQ DRE electronics will be placed on and into the Barrel, at MPD platform and inside the Modular Data Center (MDC). The data path is: from the DRE to the network switches at platform, and from the Network switches to the MDC.

Main MDC characteristics:

- permanent data storage (PDS) to store 5 Pebibytes of data;
- 2000 computing cores.

By the end of 2024, the Control Room is fully equipped (see Fig. 3.9.7) and put in operation.

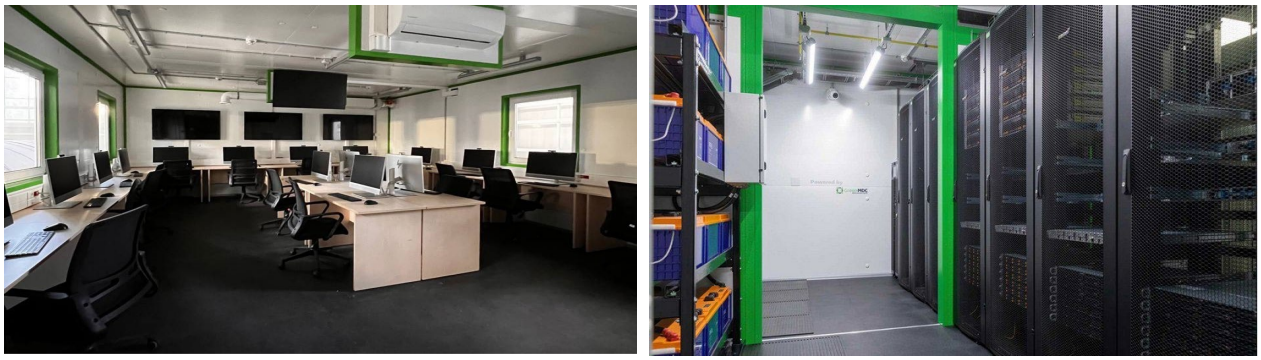

Fig. 3.9.7. Control Room (left), MDC inside (right).

White Rabbit provides sub-nanosecond accuracy and picoseconds precision of synchronization for large distributed systems. It also allows for deterministic and reliable data delivery. DRE boards digitize detector signals using common notion of time and frequency provided by the White Rabbit (WR) network. The time reference is provided by GPS/GLONASS receiver and backup precision frequency reference (Cesium or Rubidium clock). Timing Network structure and WR switches test stand are shown in Fig. 3.9.8.

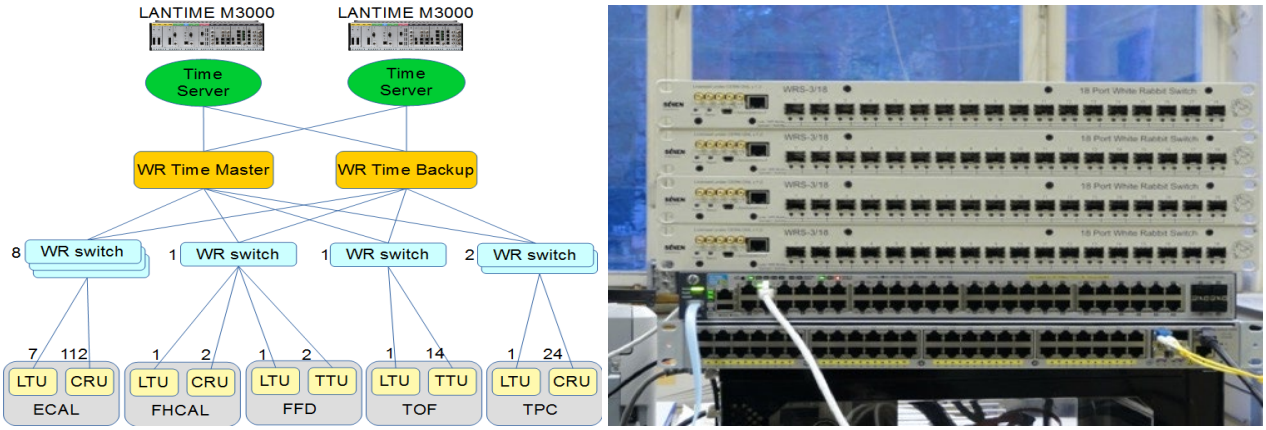

Fig. 3.9.8. The MPD Timing Network structure (left) and WR switches test stand (right)

3.9.4 MPD DAQ software

DAQ software is capable to configure all modules described in previous sections. All data is received from devices, packed in MpdRawData format and saved in to a file. Run configuration (all program configuration participating in the experiment) stores in a database as non-modified record. Planed to add ability to change program configurations according to selected Run preset.

3.10. Engineering Support

The NICA-MPD-Platform is designed and installed for the operation of all subsystems of the MPD multipurpose detector (Fig. 3.10.1). It is an integral part of the infrastructure of the NICA project and is mechanically connected to MPD.

The NICA-MPD-Platform is designed to ensure continuous operation of DAQ electronics, power supply of subdetectors, monitor and control elements of subdetectors.

Fig. 3.10.1. NICA-MPD-Platform

The following works were performed to construct the NICA-MPD-Platform:

- 25 racks were installed for equipment with ventilation panels and 13 fan coils for cooling equipment on each floor of the platform (Fig. 3.10.2).

- Each rack has a 3-phase socket block of C14 standard, with phase load monitoring for balancing and the possibility of remote disconnection.

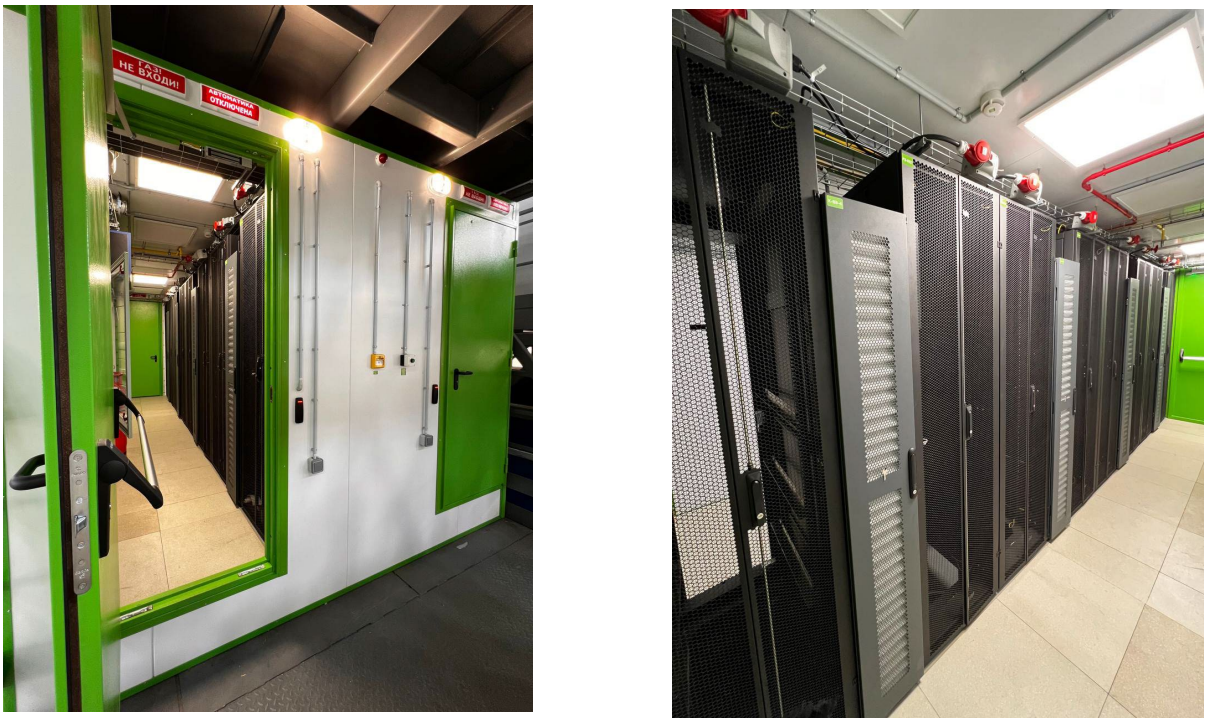

Fig 3.10.2. Racks and fan coils

- the power supply project is fully implemented on all 4 floors. The power supply of the platform is isolated, and switchboards are installed on each floor, which allows preventive maintenance of each floor without disconnecting the entire NICA-MPD-Platform.

- an access control and management system were installed. This system is integrated with the existing DAQ-DATA CENTER system. For access to all premises, employees can use an existing pass issued to JINR employees.

- a video surveillance system was installed on each floor of the NICA-MPD-Platform.

- an autonomous fire extinguishing system was installed on each floor, based on reducing oxygen concentration by introducing non-flammable gas. HFC-125 is used as a fire extinguishing agent. Detectors and light displays located according to the project above each entrance of the protected facility are also installed and connected. The autonomous fire extinguishing and fire alarm system was put into operation and is connected to transmit a fire and malfunction signal. (Fig. 3.10.3)

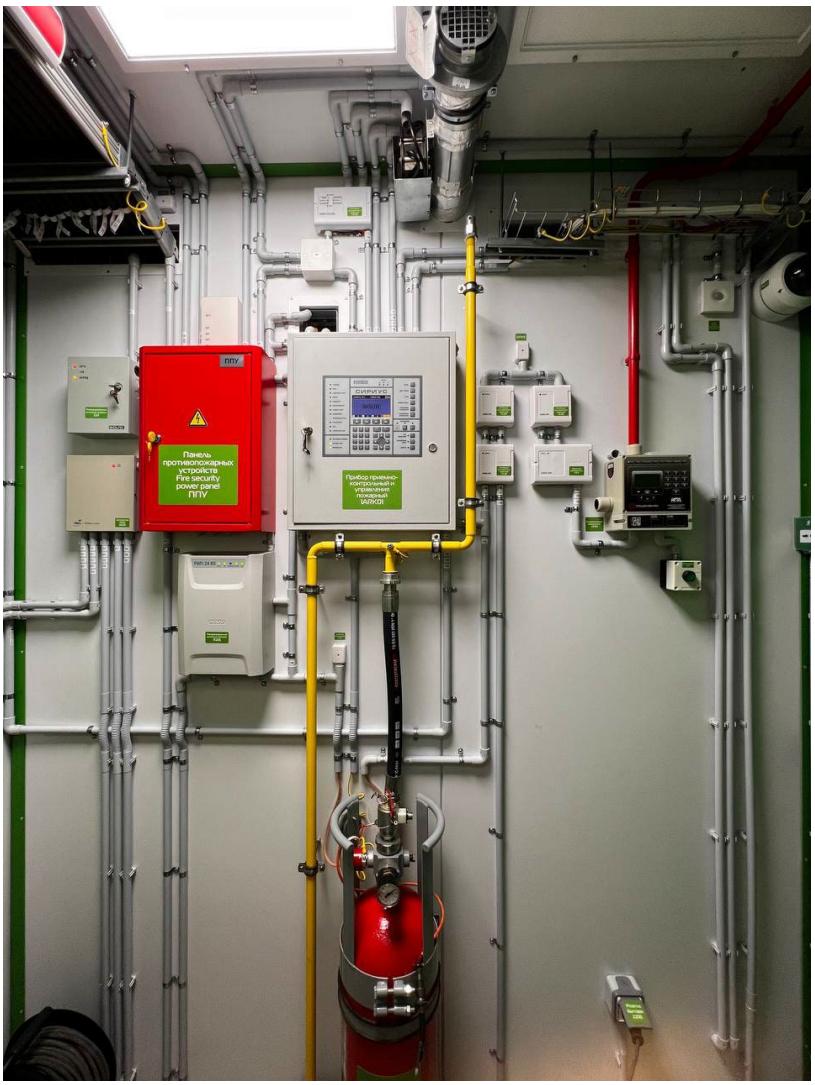

Fig 3.10.3. Fire automation of extinguishing system

- A ventilation system is installed on each floor.

- An optical cable interstorey system was implemented and tested.

- The water cooling system of the platform was implemented.

- The design of the cable tray system from the MPD detector to the NICA-MPD-Platform was developed and approved.

- Fasteners and racks for crates located on the magnet on the west and east sides were developed, tested and approved.

- A system for storing and visualizing cable marking and tracing detector groups was implemented. Much work has been done to collect data from all cables of each detector group. This information will be integrated into the created database system. This will be necessary when connecting (and later maintaining cable systems) subdetectors to equipment located on the magnet and the NICA-MPD-Platform.

NICA-MPD-Platform engineering systems are fully installed, water cooling is scheduled to be launched at the end of 2024, and all systems are tested under a design load of 330 kilowatts. Testing of each floor will be performed under a load of 100 kilowatts.

In 2025, it is planned to install a module to accommodate the electronics of the ITS subdetector (Fig. 3.10.4).

The module will be located on the second floor of the Southern Platform above the TPC and Ecal water treatment system. The module being created for the placement of electronics will be fully integrated into the existing NICA-MPD-Platform for power supply, fire alarm, water cooling and dispatching systems.

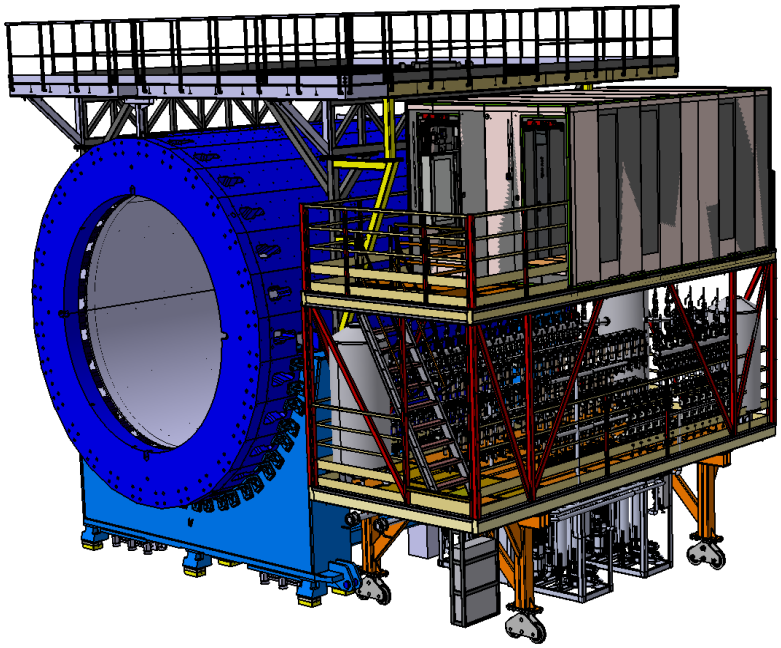

Fig. 3.10.4 Southern Platform

Presentations at international conferences in 2022-2024:

1) XI Collaboration Meeting of the MPD Experiment at the NICA Facility, VBLHEP, Joint Institute for Nuclear Research, on April 18-20, 2023.
2) NICA Days 2023 and XII MPD Collaboration Meeting, Belgrade, Serbia, on November 02-06, 2023.
3) XIII Collaboration Meeting of the MPD Experiment at the NICA Facility, VBLHEP, Joint Institute for Nuclear Research, on April 23-25, 2024

4. Detectors of the Second Stage Configuration of the MPD

4.1 The Inner Tracking System of the MPD.

4.1.1 Report on the ITS Development in period 2021-2025

The MPD-ITS functions as an international project with the participations of JINR and SPbSU in Russia and CCNU, USTC, IHEP and IMP in China. Following are the main achievements of each side of the collaboration from 2021 to 2025.

In Russia:

1) The draft of the TDR for building the inner vertex all MAPS tracker comprising six layers of cylinders around the collider interaction diamond grouped in a 3-layers inner barrel surrounded by a 3-layers outer barrel (OB and IB) (Fig.1) was completed in all technical details on the readout electronics, mechanics, leakless liquid and gas cooling systems, etc., together with the results of computer modeling carried out during the optimization of the setup and demonstration of its feasibility for identification of short range decays of D^0 and D^+ mesons (Fig.2). A two stage scenario for building ITS in close correspondence with the accelerator division plans for commissioning the NICA collider was worked out with OB to be built first by 2028, while the complete configuration of the ITS, - OB+IB built within the technology inherited from CERN ALICE ITS2 to be commissioned in 2030 after the exchange of the initial beam pipe of diameter 64 mm to the beam pipe of smaller 38 мм diameter. Currently the document goes through final editing to submitted for publication in the first half of 2025.

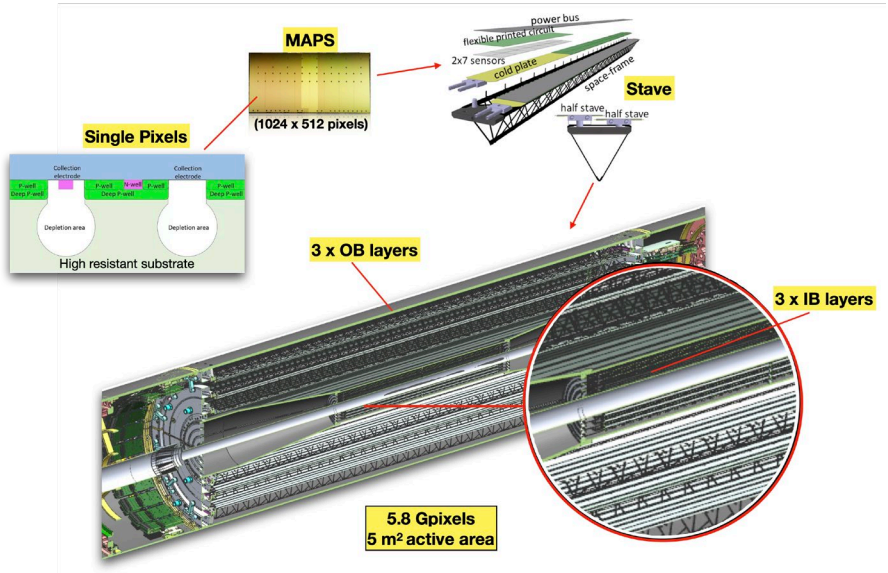

Fig.1 Full structure of the 6-layers MPD-ITS detector from a single pixel up to the Inner and Outer barrel layers.

2) The work plan for building the system was revised and clarified after the breakout of complete embargo on Western-made microelectronics components in February 2022 initially expected to be received from CERN according to the Protocol #136 signed by CERN and JINR in 2018. An agreement was reached with Chinese partners for joint R&D on components missed in sensors and readout parts of the system.

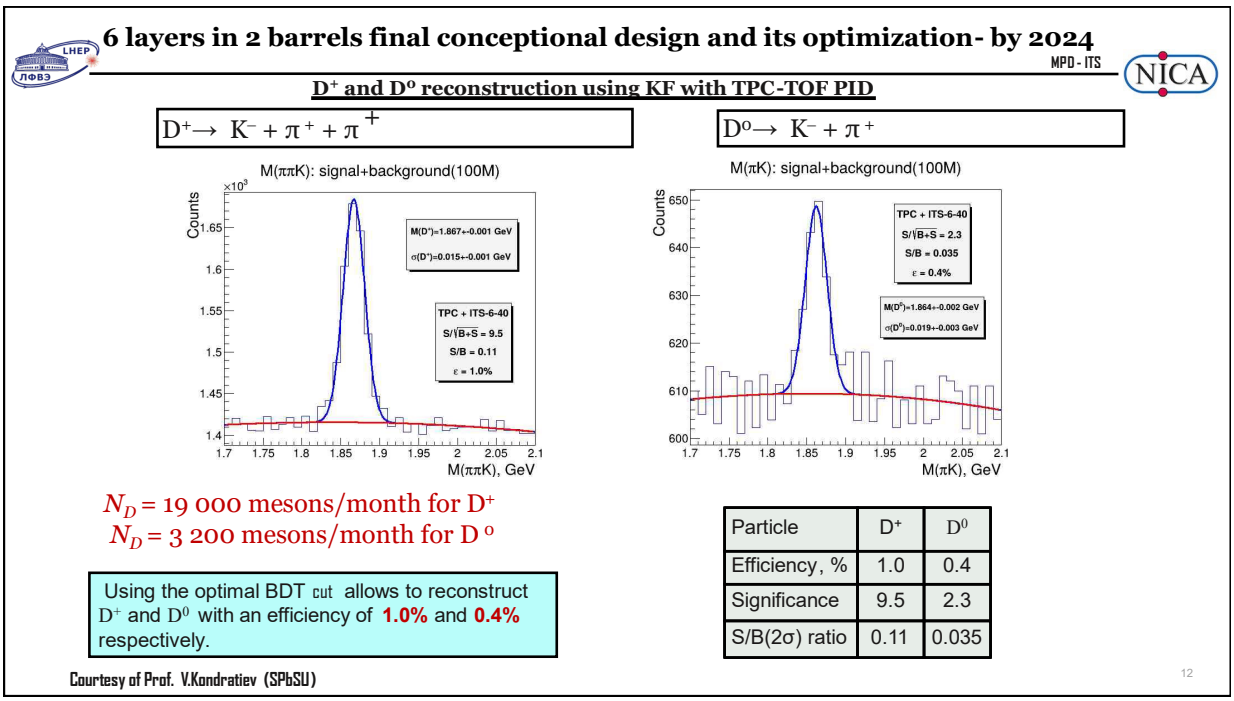

Fig.2 D^0 and D^+ simulated reconstruction using information from ITS+TPC+TOF subsystems.

3) An original scenario of integration of the ITS, beam pipe and two FFDs was put forward with 95% of parts, auxiliary tooling and fixtures currently manufactured in-house (Fig.3), by partners from SPbSU and domestic GRAFIT Pro company. Dry tests of the integration of the Installation Container with the embedded ITS mechanics are planned to be carried in Quarters 1-2 of 2025

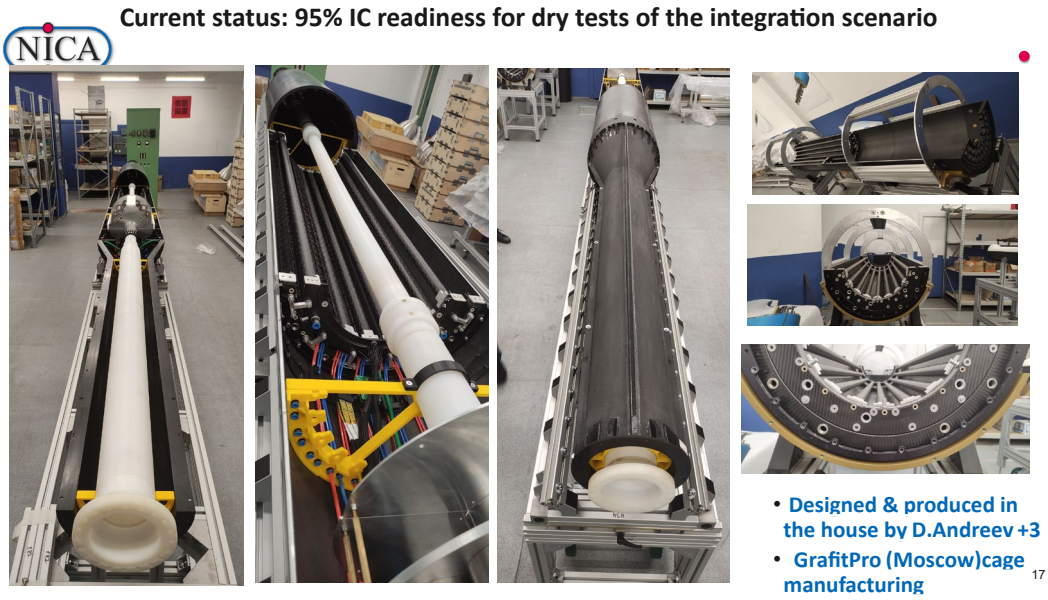

Fig.3 Real components of the Installation Container already produced with mockups of the beampipe and FFD in place.

4) The cooling plant (Fig.4) for liquid leakless cooling of ITS has been designed and is now being manufactured by the DSSE company with delivery time to JINR not later April 2025. The corresponding infrastructure is under preparation for the commissioning of the system and the starting of the planned SCADA development for the ITS cooling.

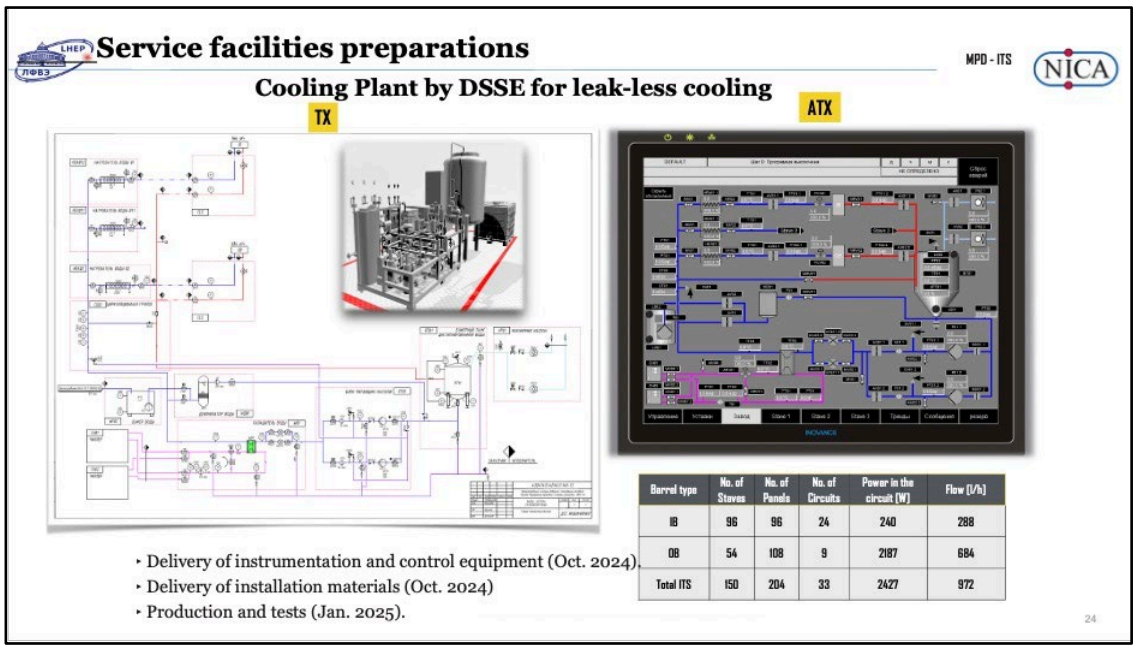

Fig.4 Sketch of the MPD-ITS dedicated leak-less cooling plant (left) and a sample of the automation control panels (right).

5) A readout system was developed in-house for lab and in-beam tests of ALPIDE-like Monolithic Active Pixel Sensors (MAPS). The system was tested successfully in an experiment carried out in a 1 GeV proton beam of PNPI, Gatchina (Fig.5).

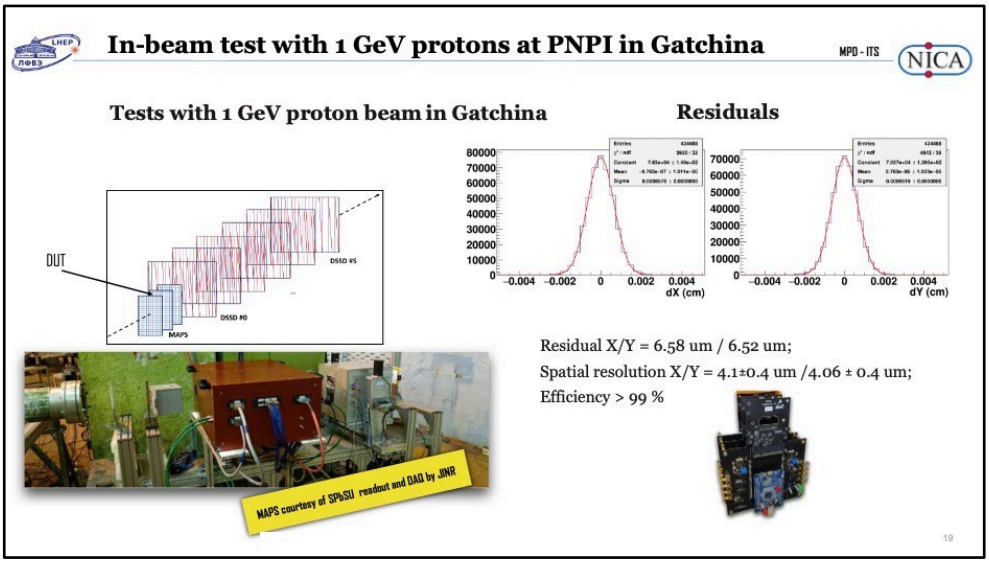

Fig.5 Summary of the setup and results of the in-beam tests conducted at the 1 GeV proton beam accelerator in PNPI, Gatchina.

6) A fully equipped module assembly site infrastructure was setup at LHEP including two skillful engineers and three trained technicians capable of assembling ITS modules under supervision of the automated Construction Management System adopted and installed at LIT facilities. The equipment for assembling supermodules was delivered from CERN but not yet installed for operation due to absence of the clean area needed for its installation that are currently occupied by the MPD TPC team.

In China:

1) The First prototype of ALPIDE-like MAPS (MICA) sensor was developed at CNNU and produced at a Chinese foundry (Fig.6) on high resistive P substrate with lab tests (Fig.7) to be carried out jointly in CCNU and JINR by the end of 2024. In-beam tests are planned with 1 GeV protons in 2025 (optionally). The design (a.k.a. “tapeout”) of the second prototype should be available no later than the 3-rd quarter of 2025.

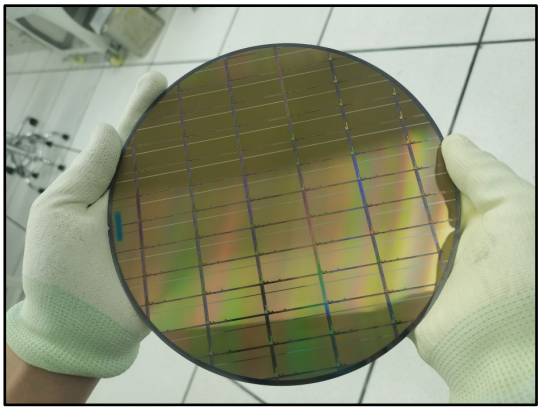

Fig.6 First produced wafer of the first prototype of the MICA chips.

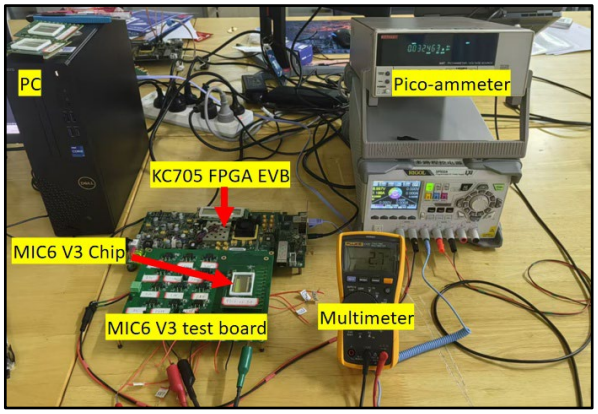

Fig.7 Test setup for the in-lab characterization of the first prototype of the MICA chip.

2) Custom designed FPGA-based Readout System along with the Power Unit was developed at USTC for reading out the supermodules (a.k.a. “staves”) comprising of MICA sensors of IB and OB . The modules have already delivered to JINR for further lab tests at LHEP scheduled for 2025
3) The first protypes of the GBT ASICs for the fast aggregation of data and its transfer via optical lines from the detector area to the nodes of the online server was designed and manufactured with lab tests currently being undertaken in CCNU.

Published papers.

1. NICA-MPD Vertex Tracking Detector Identification Capability for Reconstructing Strange and Charmed Particle Decays.A.I.Zinchenko, S.N.Igolkin, V.P.Kondratiev, Y.A.Murin, Physics of Elementary Particles and Atomic Nuclei, Letters, 17, 6, 856-870, 2020.

2. Detection of D+-meson decays in the tracking system of NICA-MPD. V. Kondratiev, C. Ceballos, S. Igolkin, A. Kolozhvari, Y. Murin, A. Sheremetiev, Acta Physica Polonica B, 14, 3, 497-501, 2021.

3. The Inner Tracking System for the MPD Setup of the NICA Collider", Physics of Particles and Nuclei, 2021, Vol. 52, No. 4, pp. 742–751. Yu. A. Murin, and C. Ceballos for the MPD-ITS Collaboration.

4. Status and initial physics performance studies of the MPD experiment at NICA. MPD Collaboration, Eur.Phys.J. A, 58, 140-189, 2022.

5. LDALA14:a 14 Gbps optical transceiver ASIC in 55 nm for NICA multipurpose detector project. Chen Q., Guo D., Zhao C., Arteche R., Ceballos C., Fang N., Gan Y., Guo Z., Murin Y., Sun X., Yi L., Journal of instrumentation, 17, August, C01027, 2022.

6. A low noise 5.12 GHz PLL ASIC in 55 nm for NICA multi purpose detector project. Zhao C., Guo D., Chen Q., Guo Z., Arteche R., Ceballos C., Fang N., Gan Y., Murin Y., L.Yi, Journal of instrumentation, 17, August, C09003, 2022.

7. A 13 Gbps 1:16 deserializer ASIC for NICA multi purpose detector project. Chen Q., Guo D., Zhao C., Guo Z., Arteche R., Ceballos C., Fang N., Gan Y., Murin Y., L.Yi, Journal of instrumentation, 17, August, C08027, 2022.

8. A 14 Gbps VCSEL driving ASIC in 55 nm for NICA multi purpose detector project. Zhao C., Chen Q., Guo Z., Arteche R., Ceballos C., Fung N., Gan Y., Murin Y., L.Yi, Guo D., Journal of instrumentation, 17, August, C08027, 2022.

9. Construction Management Information System at JINR. C. Ceballos, A. A. Kolozhvari, A. G. Dolbilov, R. N. Semenov, E. A. Tsapulina, A. Rodriguez, A. D. Sheremetiev, Yu. A. Murin, Physics of Particles and Nuclei Letters, 2023, Vol. 20, No. 5, pp. 981–987.

10. MPD-ITS Current Status. A. D. Sheremetev, C. Ceballos and Yu. A. Murin for the MPD-ITS Collaboration, Physics of Particles and Nuclei, 2023, Vol. 54, No. 4, pp. 720–724.

11. Modern Microelectronics for MPD-ITS. Monolithic Active Pixel Sensors and Readout System. Yu. A. Murin and C. Ceballos Sanchez for the MPD-ITS Collaboration, Physics of Particles and Nuclei, 2024, Vol. 55, No. 4, pp. 1061–1065.

12. Determination of the natural frequencies of ultralight carbon fiber trusses for silicon tracking systems. M. Herrera, T. Ligdenova, C. Ceballos, D. Dementev, S. Igolkin, V. Zherebchevsky, accepted for publication at Revista Mexicana de Física.

Talks at conferences

1. *Towards MAPS based Inner Tracking System of NICA MPD.* César Ceballos Sánchez for the MPD-ITS Collaboration. LXXI International conference "NUCLEUS – 2021. Nuclear physics and elementary particle physics. Nuclear physics technologies", St. Petersburg, September 20-25, 2021.

2. Construction Management Information System at JINR. *César Ceballos Sánchez for the MPD-ITS Collaboration. LXXII International conference "Nucleus-2022: Fundamental problems and applications" Moscow, July 11-16, 2022.*

3. Modern Microelectronics at NICA. *To be or not to be? Yuri Murin and Cesar Ceballos Sanchez or the MPD-ITS Collaboration. XXV International Baldin Seminar On High Energy Physics, Dubna, September 18-23, 2023.*

4. MPD-ITS Current Status. *César Ceballos Sánchez (JINR) for the MPD-ITS Collaboration. LXXIV International conference "Nucleus-2024: Fundamental problems and applications". Dubna, July 1-5, 2024.*

5. Status and Perspective of the NICA MPD Project. Yu.Muri. *Invited talk at the CEPC Workshop, Hangzhou October 22-27, 2024.*

Team description

Total number: 19 Full FET +2x0.5 FET=20 FET

Researchers: 4

Engineers: 10

Technicians: 2

Specialist: 3

Laboratory assistant: 1

Estimated consumption of ITS (OB+IB)	
Cooling system electric power	< 33 kW
CAEN electric power	< 3.3 kW
Chiller cooling water flow	< 20 l/min
Readout crates cooling water flow	< 10 l/min
Compressed air (6 – 8 bar)	< 1500 l/min
Pure nitrogen for detector cooling (6 – 8 bar)	< 140 l/min

4.1.2 Development of ITS System in 2026 – 2030

The Inner Tracking System (ITS) [1] of the Multi- purpose Detector (MPD) [2] will be a vertex silicon detector designed for the efficient registration of short-lived products of nucleus–nucleus interactions and it is planned to be built using the novel technology of monolithic active pixel sensors (MAPS) following the corresponding know-how and technological transfer from CERN's ALICE-ITS upgrade project (ALICE-ITS2) to JINR to create a large-area MAPS-only tracker at NICA. The project is being implemented as a collaboration of several institutions from Russia and China lead by JINR and the Central China Normal University (CCNU) respectively. Figure 1 shows the scheme of the tracker comprising six layers of cylinders around the collider interaction diamond grouped in a 3-layers inner barrel surrounded by a 3-layers outer barrel (OB and IB). The main quantitative figures of the MPD-ITS are listed in table 1.

Table 1 Main figures of the MPD-ITS detector.

Barrel	Layers	Staves	Numb. MAPS	Giga Pixels	Area (m^2)
OB	3	54	10584(*)	5.55	4.76
IB	3	48	864(**)	0.45	0.39
Total	**6**	**102**	**11448**	**6.00**	**5.15**

(*) Thickness = 100 um.

(**) Thickness = 50 um

Thanks to the remarkable spatial resolution (~ 5 um) and high counting rate of the MAPS it is expected that the ITS in combination with the TPC will make possible to detect short-lived products of AA interaction with maximum efficiency.

Figure 2 shows the results of the simulations carried out within the MpdROOT framework for the reconstruction of short range D mesons from the invariant mass spectrum of their decay products $D^0 \rightarrow K^- + \pi^+$ (λ= 123 um) and $D^+ \rightarrow K^- + \pi^+ + \pi^+$ (λ= 312 um) for a 6-layers MAPS ITS in combination with the TPC and a beampipe diameter of 40 mm for Bi+Bi collisions at $\sqrt{S_{NN}}$ =11 GeV.

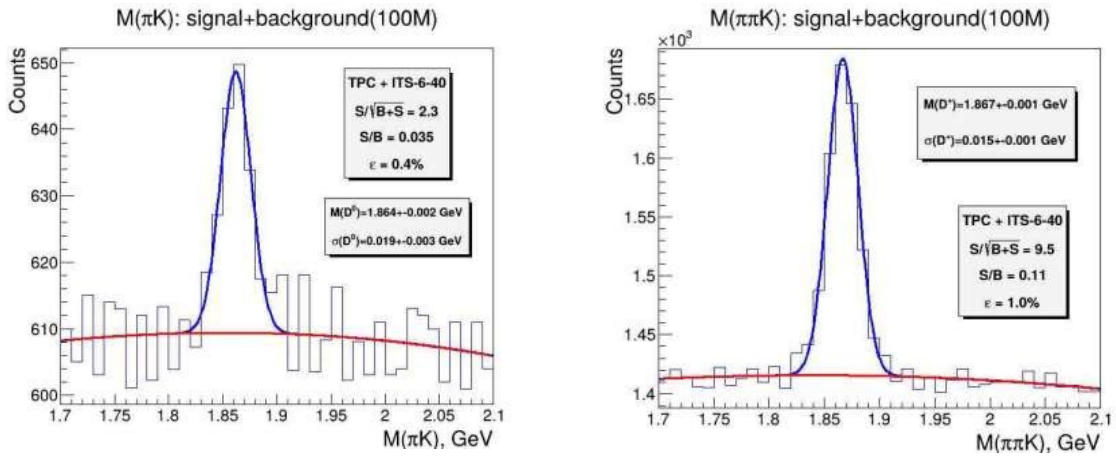

(a) (b)

Fig. 2 Extraction of the signal in the invariant mass spectrum from the combinatorial background for Bi+Bi central collisions at $\sqrt{S_{NN}}$ =11 GeV for D^0 (a) and D^+ (b) mesons.

For these simulations 10^8 signal events (decays) and $5 \cdot 10^5$ minimum bias background events were generated based on the thermal generator and the DCMSMM respectively. The results show that with this configuration it is possible to reach a pointing resolution of 120 um that would allow for the reconstruction of D^0 mesons with p_t > 500 Mev/c. Table 2 show the results for the reconstruction of both particles in terms of Efficiency, Significance and Signal-to-Background ratio.

Table 2. Main values of the reconstruction of D^+ and D^0 mesons with the proposed configuration of tracker and beampipe.

Magnitude	D^+	D^0
Efficiency (%)	1.0	0.4
Significance	9.5	2.3
S/B(2**σ**) ration	0.11	0.035

According to these results the proposed configuration allows for a monthly reconstruction rate for D^0 and D^+ mesons of 3200 and 19000 respectively.

The MICA MAPS

The MAPS sensors to be used for the production of the MPD-ITS are currently being developed at the CCNU under the name of MICA and are based on the concept of the ALPIDE sensor designed at CERN [3] that are currently banned to be imported into Russia. The design takes full advantage of a particular process feature, the deep p-well, which allows for full CMOS circuitry within the pixel matrix, while at the same time retaining the full charge collection efficiency. This, together with the small feature size and the availability of six metal layers, enables the placement of a continuously active, low-power front end in each pixel. The goal is to produce a chip with the characteristic listed in table 3.

Table 3. Nominal characteristics of the MAPS sensor.

Parameter	Value
Chip size	15 × 30 mm
Number of pixels	512 × 1024
Pixel Size	28 × 28 um
Event time resolution	<2 us
Power consumption	39 mW/cm2

Figure 3 shows a cross-section of the MICA sensor, where it can be seen that in this case the expitaxial layer has been fully replaced by a high-resistivity substrate that simplifies the production process.

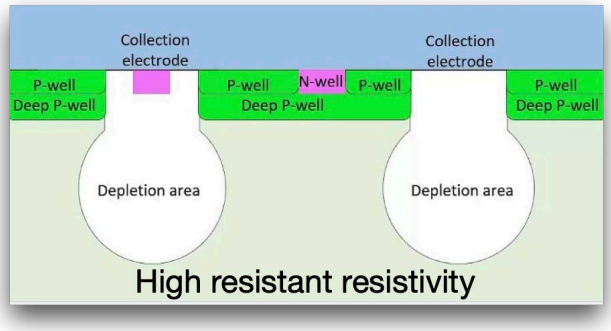

Fig 3 Cross section of the MICA Chip

The CMOS production of the prototype test chip is based on 130 nm, using a Multi-project wafer service (MPW) that allows to aggregate different chip designs in the same wafer, making the prototyping process faster and cost effective. For example, the in the first batch 3 different pixels structures each one comprising a 4x4 matrix were tested. At present the first prototype of the sensor has been produced and is undergoing the in-lab tests at CCNU for the characterization of the pixel matrix. The second version of the chip is expected to be sent soon to the foundry in China. The first samples of the MICA chips have already been received at JINR to continue with the in-lab studies and characterization in parallel with CCNU.

Readout system.

As a first approach a custom designed FPGA-based Readout System along with the Power Unit was developed at USTC for reading out the supermodules (a.k.a. “staves”) comprising of MICA sensors. The modules have already delivered to JINR for further lab tests at LHEP scheduled for 2025

On the other hand, the final readout is planned to be based on the ASICs from the GBTx family as follows.

NICA_ROC: Concentrates the output data of front-end MAPS chips and transfer the packaged data to the following NICA_GBTx ASIC. It also receives control commands, clocks, and trigger signals from the backend and distributes them to the MAPS chips.

NICA_GBTx: A high-speed bidirectional data interface ASIC for optical links. It receives multichannel data from the front-end (NICA_ROC), performs scrambling, encoding, frame building and serializing as the main function for the up-link direction. It receives high-speed serial data from the back-end, performs CDR (Clock and Data Recovery), deserializing, decoding and distributing to the front-end as the main function for the down-link direction.

NICA_LD (Laser Driver) and NICA_TIA (Transimpedance Amplifier): Are two analog ASICs that would be integrated together with the laser and PD (Pin Diode) in the customized optical transceiver module. NICA_LD receives the high-speed up-link serial data from NICA_GBTx and amplifies the signal to drive the laser.

NICA_TIA receives the down-link serial signal from the pin diode, and amplifies the signal to NICA_GBTx, so that the data can be furthered processed in NICA_GBTx.

All these ASICs are currently banned for export either to Russia or to China. For that reason, the development and production of these chips in China was included in the framework of the MPD-ITS project so to have free access to a full family of GBT (GigaBit Transceiver) ASICs both in Russia and China. Additional details may be found in the related published articles [4–7].

The second version of the prototypes of the NICA_GBT family ASICs is currently ready. This includes the NICA_LD, NICA_TIA and NICA_GBTx chips. The design of the NICA_LD_v2 and NICA_TIA_v2 were combined into one chip for further test and verification and the design of the NICA_GBTx_v2 that includes all the analog sub-modules. The R&D process is still ongoing and the finalized readout unit of the MPD-ITS based on self-designed ASICs is expected to be accomplished by mid-2027.

The schedule of the main milestones of the project in the period 2026-2030 may be summarized as follows:

2026:

Lab and in-beam tests at NPNI of the second version of the MICA chip.

Design of the ITS IB mechanics and jigs for its manufacturing and integration with ITS OB.

Infrastructure preparations for the supermodule assembly site at LHEP accomplished.

2027:

Lab and in-beam tests at NPNI of the third (final) version of the MICA chip (optional).

Start of the pre-serial production of MICA chips in China.

Lab tests of the RU and PU modules (ROC ASIC used) delivered from USTC.

Commissioning of the supermodule assembly site at LHEP.

2028

Manufacturing of RU and PU (final version with ASIC) in China in quantities enough for readout of ITS OB.

Start of assembling of modules and supermodules in China.

2029

Start of assembling of modules and supermodules at LHEP.

Continuation assembling of modules and supermodules at CCNU.

Assembling of the ITS-OB.

Commissioning ITS-OB.

2030

Building ITS-IB.

Integration of ITS in full configuration (ITS=OB+IB) with beam pipe diameter 38 мм .

Commissioning ITS.

References:

1. MPD-ITS technical design report. https://disk.jinr.ru/index.php/s/SgscL93JwxKpoDp.

2. The MPD experiment. https://nica.jinr.ru/projects/ mpd.php.

3. M. Mager et al. (ALICE Collab.), “ALPIDE, the monolithic active pixel sensor for the ALICE ITS upgrade,” Nucl. Instrum. Methods Phys. Res., Sect. A 824, 434–438 (2016).

4. Q. Chen, D. Guo, C. Zhao, R. Arteche, C. Ceballos, N. Fang, Y. Gan, Z. Guo, Yu. Murin, X. Sun, and L. Yi (MPD ITS Collab.), “LDLA14: A 14 Gbps optical transceiver ASIC in 55 nm for NICA multipurpose de- tector project,” J. Instrum. 17, C01027 (2022).

5. C. Zhao, D. Guo, Q. Chen, Z. Guo, R. Arteche, C. Ceballos, N. Fang, Y. Gan, Yu. Murin, and L. Yi, “A low noise 5.12 GHz PLL ASIC in 55 nm for NICA multipurpose detector project,” J. Instrum. 17, C09003 (2022).

6. Q. Chen, D. Guo, C. Zhao, Z. Guo, R. Arteche, C. Ceballos, N. Fang, Y. Gan, Yu. Murin, and L. Yi, “A 13 Gbps 1:16 deserializer ASIC for NICA multipur- pose detector project,” J. Instrum. 17, C08027 (2022).

7. C. Zhao, Q. Chen, Z. Guo, R. Arteche, C. Ceballos, N. Fang, Y. Gan, Yu. Murin, L. Yi, and D. Guo, “A 14 Gbps VCSEL driving ASIC in 55 nm for NICA multipurpose detector project,” J. Instrum. 17, C08027 (2022).

4.2. Forward tracker for the MPD experiment

4.2.1 Introduction

The Multi-Purpose Detector (MPD) at NICA is aimed to investigate the phase diagram of QCD matter at high baryon densities and search for transition of nuclear matter into a deconfined state of quarks and gluons, known as the Quark-Gluon Plasma (QGP). The MPD will be constructed in two stages. The Stage 1 setup includes the time projection chamber (TPC), the time-of-flight (TOF) detector and the electromagnetic calorimeter (ECAL) covering the pseudorapidity range $|\eta|<1$ and supplemented with beam-beam counters and zero degree calorimeters at forward rapidities. The installation of the inner tracker and the forward tracking detector is foreseen at the second stage of the experiment. In this note, we discuss the physics motivation and required properties and considerations for the construction of the forward tracker.

4.2.2 Physics program

The thermodynamic variables quantifying the state of matter are temperature (T) and baryon chemical potential (μ_B) [1]. At finite μ_B, QCD-based models predict a first-order phase transition and the existence of a critical point at the end of the first-order phase transition line. As the collision energy is reduced, the QGP is doped with more quarks than antiquarks, thus reaching a higher μ_B. At NICA energies, a significant amount of evolution happens before nuclei have completely passed through each other therefore the full three-dimensional picture of the system and the modeling of the pre-equilibrium stage become important. In order to trace the dynamics of the collision at NICA energies, it would be critical to study rapidity dependence of various observables.

4.2.3 Identified particle spectra

Extended pseudorapidity coverage would allow us to extract total yields of mesons and baryons. The study of total meson yields and ratios is particularly important in view of the non-monotonic behavior of the K^+ over π^+ ratio observed in central heavy-ion collisions that agrees qualitatively with predictions of the Standard Model of Early Stage (SMES) [2, 3], in which quarks and gluons are the relevant degrees of freedom in the early stage of the collision at high energies. Within SMES, the sharp peak in the K^+ over π^+ (the horn) seen at $\sqrt{s_{NN}}$=8 GeV is interpreted as an indication of the onset of deconfinement – a beginning of the creation of quark-gluon plasma in the early stage of collision. In the case of intermediate-size systems, however, no such structure is visible, see latest results on Ar-Sc collisions by the NA61/SHINE experiment [4] in Fig. 1, left.

The measurements of light mesons at forward rapidities would also allow one to extract the inverse slope T of mT spectra that reflects the kinetic freeze-out temperature of the created medium. The flattening of the T parameter at mid-rapidity as a function of collision energy (the step) was interpreted as a signature of the mixed hadronic-QGP phase at early stages of the collision. It is remarkable that the step is not observed for the intermediate-size systems, see Fig. 1, right, thus highlighting the importance of the scan versus collision system, energy and centrality. Measurements of the inverse slope T as a function of rapidity would offer another dimension in these studies providing additional sensitivity to the equation of state of the produced matter.

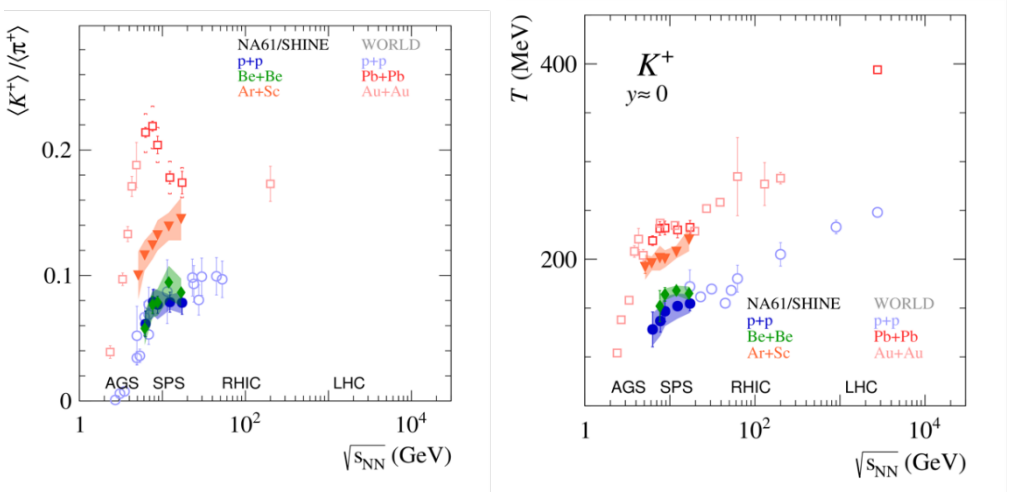

Figure 1: K^+ over π^+ yield ratio (left) and inverse slope dependence of K^+ as a function of collision energy. Figures from [4].

The forward rapidity behaviour of protons and light nuclei is particularly interesting since it is heavily influenced by the effects of baryon stopping that quantifies the amount of rapidity loss of the participant nucleons from the initial beam rapidity caused by the interactions with the other colliding nucleus. At mid-rapidity, the shape of the proton dN/dy distribution lowers and widens in more peripheral collisions as well as lower $\sqrt{s_{NN}}$, see Fig. 2. The nontrivial rapidity dependence highlights the effects of baryon stopping for proton yields and the different production mechanisms of $\pi^{\pm}$ and $K^{\pm}$. The relative abundance of these light hadrons indicates different thermodynamic environments at different energies, centralities, and rapidities.

TODO: light nuclei.

TODO: anti-baryon-to-meson ratios.

TODO: dN/dη' scaling observed both at BRAHMS and PHOBOS [5, 6, 7]. This energy scaling with ($\eta'=\eta-y_{beam}$) is usually referred as limiting fragmentation. The hypothesis of limiting fragmentation states that, in high-energy collisions, two incoming particles go through each other and break into fragments in the process instead of completely stopping each other [8]. It further predicts that at sufficiently high energies, both $d^2N/dy'dp_T$ and the mix of particles species reach a limiting value and become independent of energy in a region around $y' \sim 0$, where $y' = y - y_{beam}$ and y is the rapidity. It also implies a limiting value for $dN/d\eta'$ where $\eta' = \eta - y_{beam}$ [9].

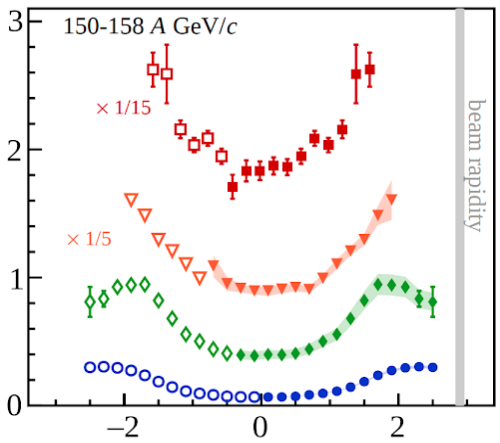

Figure 2: Proton rapidity spectra in various collision systems: p+p (blue), central Be+Be (green), central Ar+Sc (pink) and central Pb+Pb (red) collisions. Figure from [4].

Through the measurement of light hadron spectra, one would also be able to extract the temperature and baryon chemical potential as a function of the collision energy, centrality, and rapidity by fitting the yields to thermal models. Recent results from the STAR experiment [10] expand on the previously published BES-I studies at mid-rapidity [11] by examining the rapidity dependence of the rapidity density distributions and thermodynamic variables at chemical freeze-out. Similar measurements with MPD may extend our knowledge of the QCD phase diagram by examining how the thermodynamic quantities at chemical freeze-out change with rapidity.

4.2.4 Anisotropic flow

The QGP can be understood remarkably well when modeled as a hydrodynamic system, providing access to the equation of state of the QCD matter under extreme conditions. Measurements of anisotropic flow [12] have proven particularly useful to extract both the QGP properties as well as the nontrivial initial conditions [13]. The hot zone formed in any collision is geometrically anisotropic, leading to anisotropic pressure gradients and hydrodynamic response. Measured flow coefficients, vn, quantify the azimuthal anisotropy of particle emission relative to an event plane. Currently, most model studies focus around midrapidity due to both the lack of experimental data in the forward (backward) region and an insufficient understanding of particle production in the fragmentation region. The measurement of directed flow (v_1) and elliptic flow (v_2) observables over a wide pseudorapidity range will thus offer valuable constraints on the threedimensional initial state and evolution of the heavy-ion collision.

4.2.5 Directed flow measurements

The first-order flow coefficient (v_1), also referred to as the directed flow, quantifies the sideward motion of produced particles and nuclear fragments. It is particularly interesting at NICA energies, as it connects the longitudinal and transverse dynamics, manifestly probing the threedimensional nature of the system evolution. Directed flow is also sensitive to the early stage of the collision, especially in the fragmentation region, where it is believed to be generated during the nuclear passage time (~1 fm/c) [14, 15]. Directed flow therefore probes the onset of bulk collective dynamics during thermalization, providing valuable experimental guidance to models of the pre-equilibrium stage [16]. Model studies have indicated that directed flow is sensitive to the shear viscosity of the hot QCD matter [17], see Fig. 3. Furthermore, pseudorapidity dependence of the directed flow has demonstrated strong constraining power on the initial baryon stopping and can serve as a probe for the EoS in heavy-ion collisions [18, 19, 20, 21].

Past measurements have indicated that the directed flow signal is most pronounced at the forward(backward) (pseudo)rapidity [22, 23, 24, 25]. Therefore, any sensitivity of v_1 to the initial state, transport coefficients, or the EoS may be more evident at large (pseudo)rapidities. One of the remarkable observations at RHIC was that the directed flow follows the scaling behaviour similar to $dN/d\eta'$ scaling usually explained in the “limiting fragmentation” picture [22, 23, 25, 26, 27, 28], see Fig. 4. While the energy scaling of the yield around $\eta' \sim 0$ can be attributed to “spectators” minimally influenced by the collisions, the energy scaling of directed flow is less intuitive to comprehend, as v_1 is usually closely related to the collision dynamics. A common interpretation for large v_1 at the forward rapidity is the deflection of nuclear fragments. However, it is hard to explain the energy independence of the directed flow around $\eta' \sim 0$ with this picture. The limiting fragmentation of directed flow indicates the production of v_1 at the fragmentation region might not only come from the deflection.

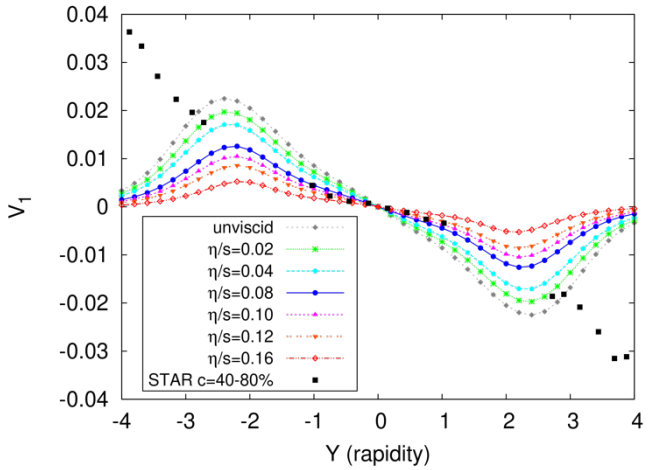

Figure 3: Directed flow of pions for different values of η/*s* compared with STAR data [25].

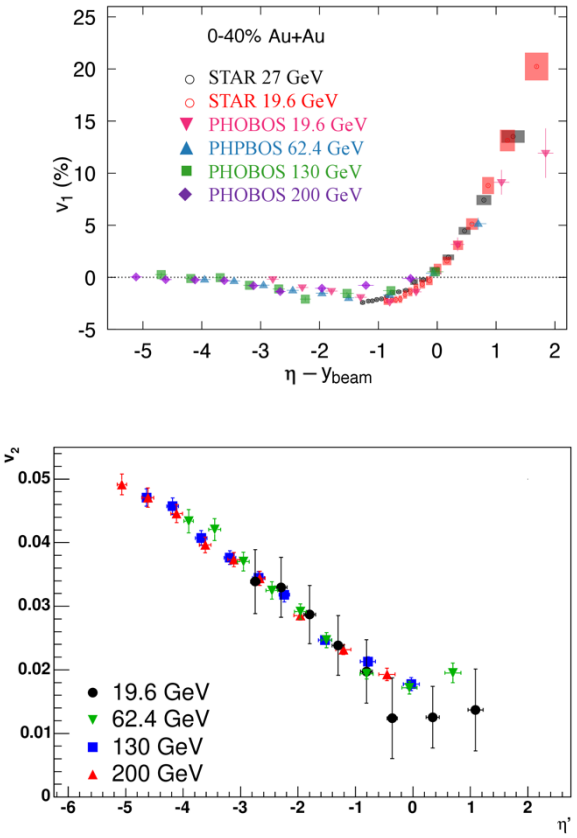

Figure 4: Directed flow (left) and elliptic flow (right) measurements as a function of $\eta'=\eta-y_{beam}$ in Au-Au collisions at 0-40% centrality for different collision energies. Figures from [29, 28].

TODO: v_1 of light nuclei and atomic number scaling [30].

4.2.6 Elliptic flow measurements

Up to now, most of the available elliptic flow measurements were performed at mid-rapidity thus limiting the scope of observables used to constrain the collision dynamics. On the other hand, v_2 measurements performed by the PHOBOS collaboration at different collision energies [28] reveal remarkable features of the v_2 behaviour as a function of pseudorapidity. Similar to the limiting fragmentation picture of charged particle density, v_2 exhibits a $dN_{ch}/d\eta$ dependence, with a maximum at mid-rapidity and falls off in the fragmentation regions. In particular, the PHOBOS

$v_2(\eta)$ data plotted against $\eta - y_{beam}$ collapses on the universal curve, see Figure 4. It would be important to trace this behaviour for different collision systems at NICA energies.

Moreover, the PHOBOS measurement of the elliptic flow at forward rapidity was shown to provide sensitivity to the temperature dependence of shear viscosity [31], see comparison of PHOBOS measurements with different assumptions on the temperature dependence in Fig. 5. There is a strong evidence that the shear viscosity must grow with decreasing temperature. This observation highlights the importance of the rapidity dependence of elliptic flow at NICA energies.

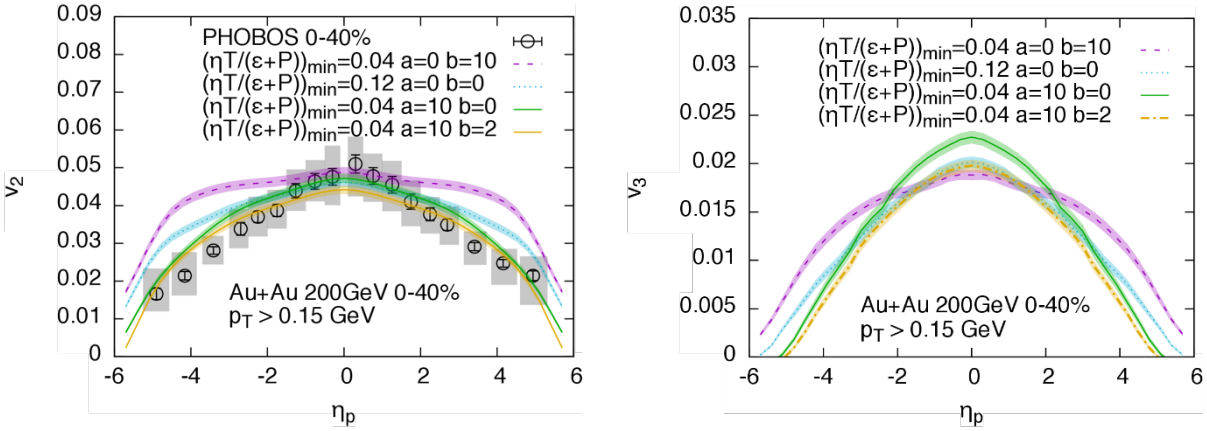

Figure 5: v_2 (left) and v_3 (right) coefficients as a s function of pseudorapidity for different assumptions on the temperature dependence of the shear viscosity. Figures from [31].

4.2.7 Global polarization measurements

Due to the presence of an initial large angular momentum in the collisions, the created QCD matter acquires vortical properties. This vorticity of the created matter is in turn reflected in spin polarization of produced particles, commonly referred to as the global polarization [32, 33]. Since the first measurements of non-zero global polarization of Λ hyperons in heavy ion collisions, it has been extensively studied over a wide range of collision energies [34, 35, 36, 37, 38]. In particular, the global polarization rises with decreasing collision energy, reaching ≈5−7% at $\sqrt{s_{NN}}$=2.4−3 GeV, as reported by the STAR and HADES collaborations [36, 38].

The rising trend of the global polarization with respect to the decreasing energy of collision qualitatively agrees with the theoretical predictions. However, the details of the evolution of polarization at lower energies have remained uncertain. Recent studies indicated the existence of a peak with the maximum value at NICA energies [39, 40, 41, 42, 43]. Extension of global polarization measurements towards forward rapidities may provide further insights on the origin of the global polarization signal.

4.2.8 Other opportunities

Here we provide a list of other opportunities opening up in case of installation of the forward tracker:

- Improved precision of centrality and reaction plane determination as well as trigger efficiency, that is especially important for small collision systems.
- TPC endcaps located in front of the forward tracker may serve for conversion of photons into electron-positron pairs thus providing an opportunity to study the spectra and effective temperature

of thermal photons in the forward direction via conversions and shed more light on the evolution of the hot and dense matter produced in heavy ion collisions at NICA [44].

- Two-particle correlation and multiparticle cumulant studies would also strongly benefit from the extended pseudorapidity acceptance thus providing additional tools for anisotropic flow measurements.
- Installation of the forward tracker and upgrade of the TPC to continuous readout may provide an opportunity to access various observables of the Spin Physics Detector (SPD) program at NICA [45].
- Extended forward rapidity coverage may be beneficial for diffractive studies in proton-proton collisions, such as instanton searches [46].

4.2.9 Forward tracker design and technology considerations

The proposed forward tracker setup is shown in Fig. 6 and consists of 5 tracking stations on each side from the interaction point. Installation of the tracker in the existing solenoidal magnetic field imposes a major challenge for the track reconstruction: momentum resolution in the solenoid field is driven by the radial distance available for the track curvature measurement that gets strongly reduced towards large η. In order to improve momentum resolution with the existing solenoid limitations and available tracking distance in z direction, one has two options: minimize the material budget of the detector to reduce multiple scattering effects and/or improve the hit resolution. This requirements strongly reduce the choice of detector technologies. In the following, strip thin gap chambers (sTGC) are considered as a baseline option for the forward tracker.

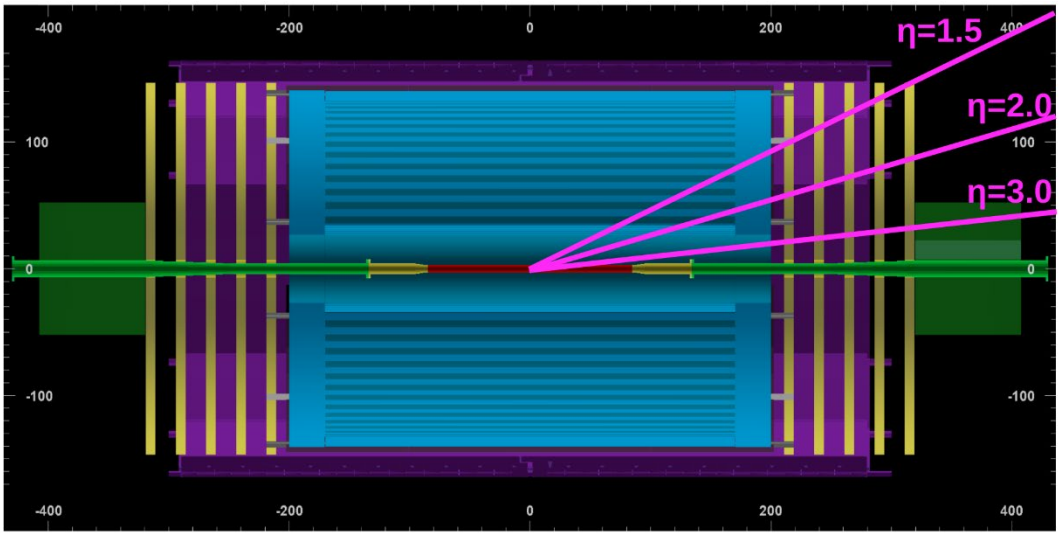

Figure 6: The proposed forward tracker setup.

4.2.10 Integration of the forward tracker into the MPD setup

The forward tracker stations can be placed in the gaps between TPC and FHCal volumes on both sides from the interaction point and cover radial distance from r_{min}=35.7 cm to r_{max}=130 cm. According to the latest engineering drawings, see Fig. 7, there is a beam pipe support foreseen at a distance |z|=250 cm from the nominal interaction point, therefore the tracker can be installed in two sub-volumes on both sides covering z-distance from 210 to 245 cm and from 255 to 295 cm. Optionally, the beam pipe can be fixed to support structures of the future forward tracker. These radial and longitudinal constraints induce the following limitations on the pseudorapidity coverage of the forward tracker: $1.55<\eta<2.47$.

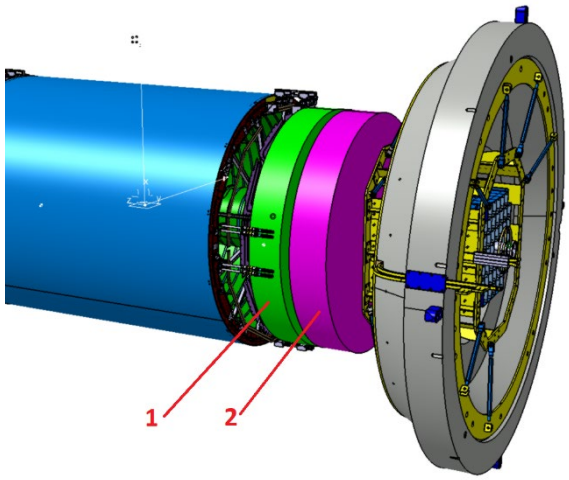

Figure 7: Engineering drawing showing two volumes (green and magenta) available for the installation of forward tracker stations.

4.2.11 Momentum resolution

Momentum resolution for the forward tracker prototype has been studied using the ACTS package [47]. The ACTS project provides experiment-independent high-level track reconstruction toolkit, including Kalman Filter for track fitting, seeding tools and combinatorial Kalman Filter for track finding as well as vertex reconstruction algorithms. In addition, the ACTS package contains a simple and fast particle transport code FATRAS which includes the effects of Bethe-Bloch energy loss for charged particles as well as angular deflection due to multiple scattering.

The FATRAS tool and a particle gun of pions and protons with transverse momenta from 0.1 to 1 GeV were used to simulate track trajectories in the the forward tracker assuming solenoid magnetic field with B_z=0.5 T. At the first stage, a standalone tracker prototype with 5 tracking layers located equidistantly from z_{min}=210 cm to z_{max}=300 cm and the total material budget of 1% X_0 was considered. The simulated Monte-Carlo hits were then smeared in x and y with the Gaussian sigma of 80 μm. The ACTS seeding algorithm was adapted to build track segments using hits in the first three layers, while the combinatorial Kalman Filter was then used to attach hits in the following layers. The resulting resolution of pion and proton pT in different η ranges is shown in Fig. 8. The momentum resolution ranges from 3% to 10% depending on pT and η range. The linear growth at high p_T is driven by the hit resolution while the degradation at low pT is caused by multiple scattering effects which are more pronounced for protons.

The obtained momentum resolution appeared to be in perfect agreement with analytical estimates of momentum smearing due to multiple scattering and hit resolution effects adapted from [48]. This agreement between analytical estimates and the results of ACTS simulations confirms the accuracy of ACTS simulations. This allows us to assess the impact of potential changes to hit resolution and material budget on track resolution without running complete simulations.

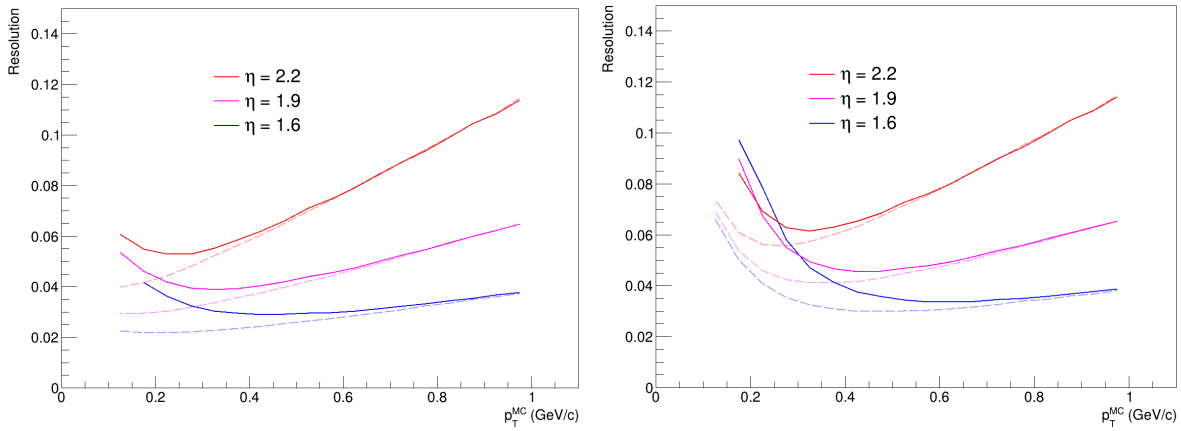

Figure 8: Transverse momentum resolution for pions (left) and protons (right) for different η regions. Dashed lines correspond to the standalone tracker while solid lines correspond to the resolution of the tracker supplemented with TPC endcaps.

However, the impact of TPC material in front of the tracker on the momentum resolution can hardly be evaluated analytically. In order to estimate the effect of TPC material budget, the FATRAS geometry of the tracker was supplemented with the toy model of TPC endcaps including readout chamber region of 25%X_0 and the frame region of 110%X_0. The resulting momentum resolution for tracks propagating through the readout chamber region is shown in Fig. 8 in comparison to the standalone tracker case. Propagation of fitted tracks through the endcaps to the interaction region results in significant degradation of the momentum resolution, most prominent at low momenta. It is worth noting that the impact of TPC endcaps might be reduced in case MWPCs are replaced with GEM-based detectors.

In conclusion, the momentum resolution for the considered tracker prototype stays within 3-10% in the η range from 1.6 to 2.2 and p_T<1 GeV that is sufficient for measurements presented in section 2.1. The momentum resolution of the tracker can be improved if forward tracks are matched to TPC track segments. On the other hand, TPC track segments may serve as seeds for forward tracking. The study of both options require development of dedicated algorithms and can be performed at the next stages of the project.

4.2.12 Track finding at forward rapidity

The track resolution study presented in the previous section was performed with a sigle-particle gun and doesn't take into account high multiplicity environment foreseen in heavy ion collisions at NICA. Moreover, FATRAS simulations do not allow one to evaluate the impact of hadronic interactions of particles with TPC material and production of secondaries. In order to estimate the impact of these effects on the track finding efficiency and the level of fakes, a more realistic forward tracker prototype was implemented in mpdroot with UrQMD generator (central Au-Au collisions at $\sqrt{s_{NN}}$=11 GeV) serving as input for MC simulations. Forward detector hits from mpdroot simulations were then propagated to ACTS for track finding. An event display for tracks reconstructed in the forward detector in a high-multiplicity collision is shown in Fig. 9. As illustrated in the figure, most of the tracks were properly reconstructed in spite of the high density of hits in the detector.

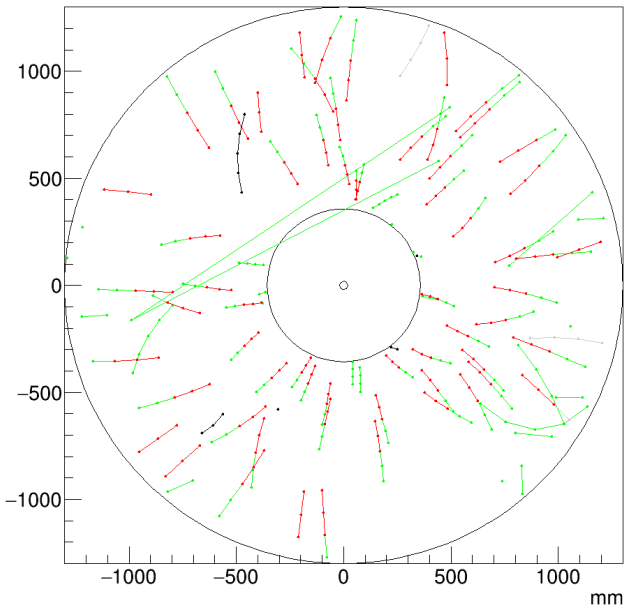

Figure 9: Projections in the xy plane for tracks reconstructed in the forward detector in high-multiplicity Au-Au collision at $\sqrt{s_{NN}}$=11 GeV. Found seeds and tracks are shown with red and green lines respectively.

Corresponding track reconstruction efficiency for primary pions and protons is shown in Fig. 10 in different η regions. The reconstruction becomes efficient starting from about 0.15 GeV and reaches 90-95% depending on η range. Reconstruction efficiency losses are caused by pion decays on the way to the forward detector and inelastic hadronic interactions of pions and protons with the material in front of the tracker.

In conclusion, the ACTS algorithms were adapted for the track reconstruction in the forward detector prototype. The ACTS toolkit can also be used for forward track matching with TPC track segments and secondary vertex reconstruction.

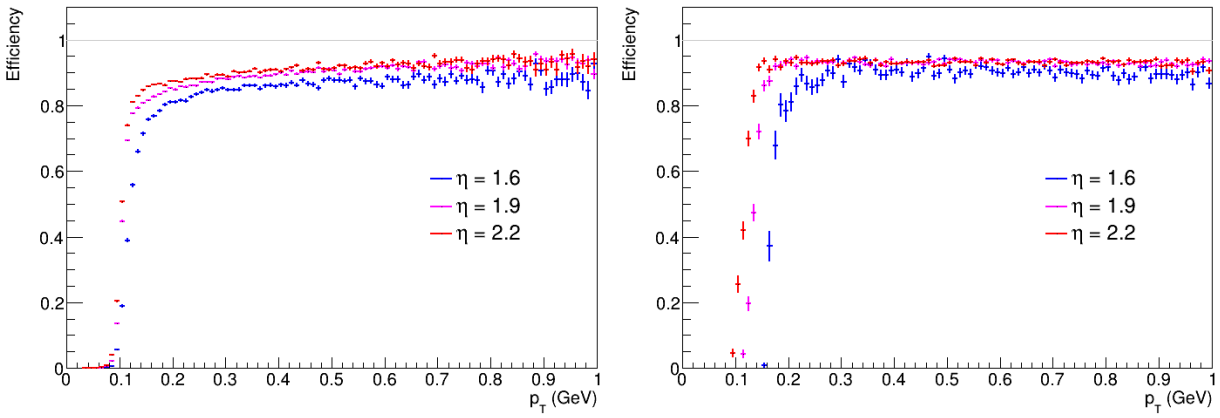

Figure 10: Tracking efficiency of the forward detector for pions (left) and protons (right) as a function of track p_T in different η regions.

4.2.13 Particle identification at forward rapidity

Most of the physics observables described in section 4.*2.2* require particle identification capabilities in the forward region. Installation of the time-of-flight (TOF) detector [49] based on multigap resistive plate chambers (MRPC) behind the forward tracker at a distance of ~3 m from

the interaction point would be a natural choice. Large length of particle trajectories at forward rapidity would be beneficial however limited momentum resolution may significantly reduce the range of momenta available for particle identification measurements. In order to assess the separation power of pions, kaons, and protons in different momentum and rapidity ranges, a toy model has been developed based on the time-of-flight resolution of 50 ps, typical for modern RPC detectors, and Gaussian momentum smearing according to estimates presented in Section 5 The squared invariant mass distributions as a function of particle momentum for protons, pions, and kaons are presented in Fig. 11 for two pseudorapidity ranges. A TOF detector with a resolution of 50 ps would allow for efficient separation of protons and kaons up to momenta of 3–4 GeV and kaon-pion separation up to 2–3 GeV depending on pseudorapidity range.

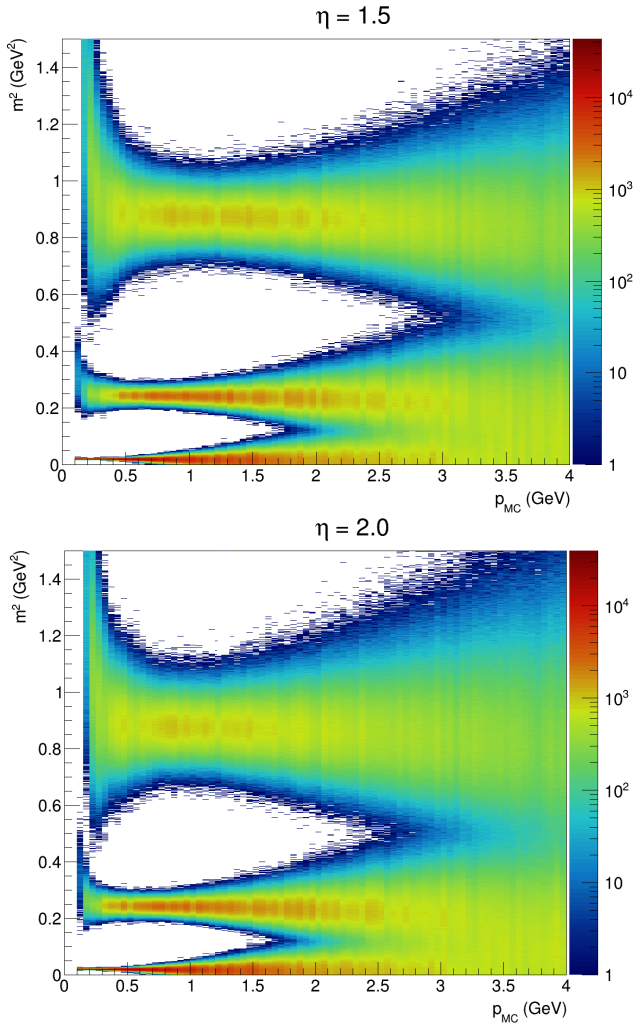

Figure 11: Squared invariant mass distributions as a function of particle momentum at η=1.5 (left) and η=2.0 (right).

References

[1] A. Sorensen *et al.*, "Dense nuclear matter equation of state from heavy-ion collisions," *Prog. Part. Nucl. Phys.* **134** (2024) 104080, arXiv:2301.13253 [nucl-th].

[2] M. Gazdzicki and M. I. Gorenstein, "On the early stage of nucleus-nucleus collisions," *Acta Phys. Polon. B* **30** (1999) 2705, arXiv:hep-ph/9803462.

[3] M. Gazdzicki, M. Gorenstein, and P. Seyboth, "Onset of deconfinement in nucleus-nucleus collisions: Review for pedestrians and experts," *Acta Phys. Polon. B* **42** (2011) 307–351, arXiv:1006.1765 [hep-ph].

[4] NA61/SHINE Collaboration, H. Adhikary et al., "Measurements of π±, K±, p and $\bar{p}$ spectra in 40Ar+45 Sc collisions at 13A to 150A GeV/c," Eur. Phys. J. C 84 no. 4, (2024) 416, arXiv:2308.16683 [nucl-ex]. [5]

BRAHMS Collaboration, I. G. Bearden *et al.*, "Charged particle densities from Au+Au collisions at s(NN)**(1/2) = 130-GeV," *Phys. Lett. B* **523** (2001) 227–233, arXiv:nucl-ex/0108016.
[6] BRAHMS Collaboration, I. G. Bearden *et al.*, "Forward and midrapidity like-particle ratios from p + p collisions at s**(1/2) = 200-GeV," *Phys. Lett. B* **607** (2005) 42–50, arXiv:nucl-ex/0409002.
[7] PHOBOS Collaboration, B. Alver *et al.*, "Phobos results on charged particle multiplicity and pseudorapidity distributions in Au+Au, Cu+Cu, d+Au, and p+p collisions at ultra-relativistic energies," *Phys. Rev. C* **83** (2011) 024913, arXiv:1011.1940 [nucl-ex].
[8] J. Benecke, T. T. Chou, C.-N. Yang, and E. Yen, "Hypothesis of Limiting Fragmentation in High-Energy Collisions," *Phys. Rev.* **188** (1969) 2159–2169.
[9] B. B. Back *et al.*, "The Significance of the fragmentation region in ultrarelativistic heavy ion collisions," *Phys. Rev. Lett.* **91** (2003) 052303, arXiv:nucl-ex/0210015.
[10] STAR Collaboration, M. Harasty, "Particle production in Au+Au collisions at beam energy scan II energies at STAR," *EPJ Web Conf.* **296** (2024) 14009.
[11] STAR Collaboration, L. Adamczyk *et al.*, "Bulk Properties of the Medium Produced in Relativistic Heavy-Ion Collisions from the Beam Energy Scan Program," *Phys. Rev. C* **96** no. 4, (2017) 044904, arXiv:1701.07065 [nucl-ex].
[12] S. A. Voloshin, A. M. Poskanzer, and R. Snellings, "Collective phenomena in non-central nuclear collisions," *Landolt-Bornstein* **23** (2010) 293–333, arXiv:0809.2949 [nucl-ex].
[13] B. H. Alver, C. Gombeaud, M. Luzum, and J.-Y. Ollitrault, "Triangular flow in hydrodynamics and transport theory," *Phys. Rev. C* **82** (2010) 034913, arXiv:1007.5469 [nucl-th].
[14] H. Sorge, "Elliptical flow: A Signature for early pressure in ultrarelativistic nucleus-nucleus collisions," *Phys. Rev. Lett.* **78** (1997) 2309–2312, arXiv:nucl-th/9610026.
[15] N. Herrmann, J. P. Wessels, and T. Wienold, "Collective flow in heavy ion collisions," *Ann. Rev. Nucl. Part. Sci.* **49** (1999) 581–632.
[16] STAR Collaboration, M. M. Aggarwal *et al.*, "An Experimental Exploration of the QCD Phase Diagram: The Search for the Critical Point and the Onset of De-confinement," arXiv:1007.2613 [nucl-ex].
[17] F. Becattini, G. Inghirami, V. Rolando, A. Beraudo, L. Del Zanna, A. De Pace, M. Nardi, G. Pagliara, and V. Chandra, "A study of vorticity formation in high energy nuclear collisions," *Eur. Phys. J. C* **75** no. 9, (2015) 406, arXiv:1501.04468 [nucl-th]. [Erratum: Eur.Phys.J.C 78, 354 (2018)].
[18] Y. B. Ivanov, "Directed flow in heavy-ion collisions and its implications for astrophysics," *Universe* **3** no. 4, (2017) 79, arXiv:1711.03461 [nucl-th].
[19] L. Du, C. Shen, S. Jeon, and C. Gale, "Probing initial baryon stopping and equation of state with rapidity-dependent directed flow of identified particles," *Phys. Rev. C* **108** no. 4, (2023) L041901, arXiv:2211.16408 [nucl-th].
[20] Z.-F. Jiang, C. B. Yang, and Q. Peng, "Directed flow of charged particles within idealized viscous hydrodynamics at energies available at the BNL Relativistic Heavy Ion Collider and at the CERN Large Hadron Collider," *Phys. Rev. C* **104** no. 6, (2021) 064903, arXiv:2111.01994 [hep-ph].
[21] Y. Nara, H. Niemi, J. Steinheimer, and H. Stöcker, "Equation of state dependence of directed flow in a microscopic transport model," *Phys. Lett. B* **769** (2017) 543–548, arXiv:1611.08023 [nucl-th].
[22] STAR Collaboration, J. Adams *et al.*, "Directed flow in Au+Au collisions at $\sqrt{s_{NN}}$=62 GeV," *Phys. Rev. C* **73** (2006) 034903, arXiv:nucl-ex/0510053.
[23] STAR Collaboration, J. Adams *et al.*, "Azimuthal anisotropy at RHIC: The First and fourth harmonics," *Phys. Rev. Lett.* **92** (2004) 062301, arXiv:nucl-ex/0310029. [Erratum: Phys.Rev.Lett. 127, 069901 (2021)].
[24] STAR Collaboration, J. Adams *et al.*, "Azimuthal anisotropy in Au+Au collisions at s(NN)**(1/2) = 200-GeV," *Phys. Rev. C* **72** (2005) 014904, arXiv:nucl-ex/0409033.
[25] STAR Collaboration, B. I. Abelev *et al.*, "System-size independence of directed flow at the Relativistic Heavy-Ion Collider," *Phys. Rev. Lett.* **101** (2008) 252301, arXiv:0807.1518 [nucl-ex].
[26] PHOBOS Collaboration, B. B. Back *et al.*, "Energy dependence of directed flow over a wide range of pseudorapidity in Au + Au collisions at RHIC," *Phys. Rev. Lett.* **97** (2006) 012301, arXiv:nucl-ex/0511045.
[27] STAR Collaboration, G. Agakishiev *et al.*, "Directed and elliptic flow of charged particles in Cu+Cu collisions at $\sqrt{s_{NN}}$= 22.4 GeV," *Phys. Rev. C* **85** (2012) 014901, arXiv:1109.5446 [nucl-ex].
[28] PHOBOS Collaboration, B. B. Back *et al.*, "Energy dependence of elliptic flow over a large pseudorapidity range in Au+Au collisions at RHIC," *Phys. Rev. Lett.* **94** (2005) 122303, arXiv:nucl-ex/0406021.
[29] STAR Collaboration, "", "Measurement of directed flow in Au+Au collisions at $\sqrt{s_{NN}}$= 19.6 and 27 GeV with the STAR Event Plane Detector," arXiv:2406.18213 [nucl-ex].
[30] STAR Collaboration, X. Liu, "First order event plane correlated directed and triangular flow in Au+Au collisions from BES-II at STAR," *EPJ Web Conf.* **296** (2024) 05013.
[31] G. Denicol, A. Monnai, and B. Schenke, "Moving forward to constrain the shear viscosity of QCD matter," *Phys. Rev. Lett.* **116** no. 21, (2016) 212301, arXiv:1512.01538 [nucl-th].
[32] S. A. Voloshin, "Polarized secondary particles in unpolarized high energy hadron-hadron collisions?," arXiv:nucl-th/0410089.

[33] Z.-T. Liang and X.-N. Wang, "Spin alignment of vector mesons in non-central A+A collisions," *Phys. Lett. B* **629** (2005) 20–26, arXiv:nucl-th/0411101.
[34] STAR Collaboration, L. Adamczyk *et al.*, "Global Λ hyperon polarization in nuclear collisions: evidence for the most vortical fluid," *Nature* **548** (2017) 62–65, arXiv:1701.06657 [nucl-ex].
[35] STAR Collaboration, J. Adam *et al.*, "Global polarization of Λ hyperons in Au+Au collisions at $\sqrt{s_{NN}}$= 200 GeV," *Phys. Rev. C* **98** (2018) 014910, arXiv:1805.04400 [nucl-ex].
[36] STAR Collaboration, M. S. Abdallah *et al.*, "Global Λ-hyperon polarization in Au+Au collisions at $\sqrt{s_{NN}}$=3 GeV," *Phys. Rev. C* **104** no. 6, (2021) L061901, arXiv:2108.00044 [nucl-ex].
[37] STAR Collaboration, M. I. Abdulhamid *et al.*, "Global polarization of Λ and Λ hyperons in Au+Au collisions at sNN=19.6 and 27 GeV," *Phys. Rev. C* **108** no. 1, (2023) 014910, arXiv:2305.08705 [nucl-ex].
[38] HADES Collaboration, R. Abou Yassine *et al.*, "Measurement of global polarization of Λ hyperons in few-GeV heavy-ion collisions," *Phys. Lett. B* **835** (2022) 137506, arXiv:2207.05160 [nucl-ex].
[39] Y. B. Ivanov, "Global Λ polarization in moderately relativistic nuclear collisions," *Phys. Rev. C* **103** no. 3, (2021) L031903, arXiv:2012.07597 [nucl-th].
[40] V. Voronyuk, E. E. Kolomeitsev, and N. S. Tsegelnik, "Hyperon global polarization in heavy-ion collisions at NICA energies. Feed-down effects and the role of Σ0 hyperons," arXiv:2305.10792 [nucl-th].
[41] Y. Guo, J. Liao, E. Wang, H. Xing, and H. Zhang, "Hyperon polarization from the vortical fluid in low-energy nuclear collisions," *Phys. Rev. C* **104** no. 4, (2021) L041902, arXiv:2105.13481 [nucl-th].
[42] F. Becattini and L. Tinti, "The Ideal relativistic rotating gas as a perfect fluid with spin," *Annals Phys.* **325** (2010) 1566–1594, arXiv:0911.0864 [gr-qc].
[43] A. Ayala, I. Dominguez, I. Maldonado, and M. E. Tejeda-Yeomans, "An Improved Core-Corona Model for Λ and Λ Polarization in Relativistic Heavy-Ion Collisions," *Particles* **6** no. 1, (2023) 405–415.
[44] E. Kryshen, N. Burmasov, D. Ivanishchev, D. Kotov, M. Malaev, V. Riabov, and Y. Ryabov, "Prospects for Photon Conversion Measurements in the Future MPD Experiment at NICA," *Phys. Part. Nucl.* **54** no. 4, (2023) 613–618.
[45] SPD Collaboration, V. Abazov *et al.*, "Technical Design Report of the Spin Physics Detector at NICA," arXiv:2404.08317 [hep-ex].
[46] V. A. Khoze, V. V. Khoze, D. L. Milne, and M. G. Ryskin, "Central instanton production," *Phys. Rev. D* **105** no. 3, (2022) 036008, arXiv:2111.02159 [hep-ph].
[47] X. Ai *et al.*, "A Common Tracking Software Project," *Comput. Softw. Big Sci.* **6** no. 1, (2022) 8, arXiv:2106.13593 [physics.ins-det].
[48] R. L. Gluckstern, "Uncertainties in track momentum and direction, due to multiple scattering and measurement errors," *Nucl. Instrum. Meth.* **24** (1963) 381–389.
[49] V. Baryshnikov *et al.*, "Status of the Time-of-Flight System of the MPD Experiment at the NICA Collider," *Phys. Atom. Nucl.* **86** no. 5, (2023) 788–795.

4.3. Forward identification detector ETOF

4.3.1. Design of the ETOF

At the second stage of the development of the MPD detector, it is planned to expand the registration area of charged particles to pseudorapidity region up to $|\eta| < 2.5$. To identify particles in this range, it is proposed to supplement the time-of-flight TOF system with two ETOF (end-cap TOF) detectors in the form of rings (Fig. 4.3.1).

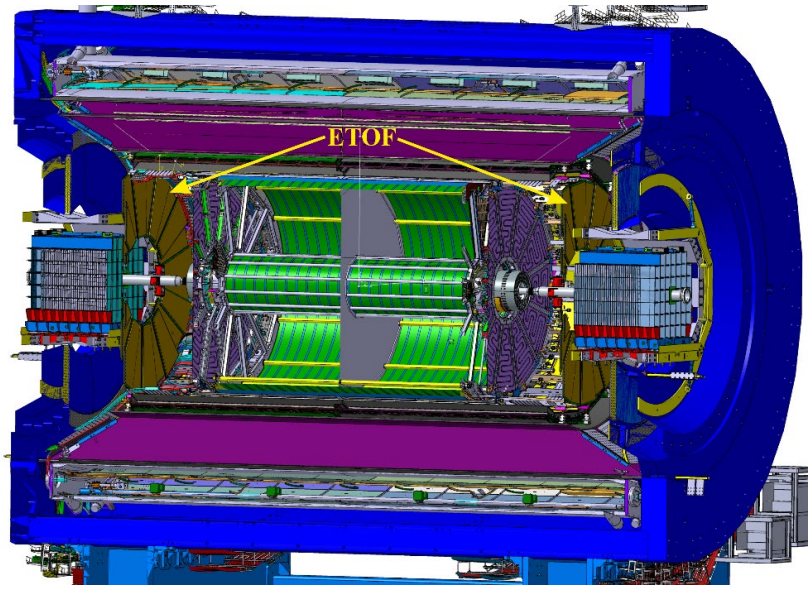

Fig. 4.3.1. The estimated location of the ETOF rings in MPD.

The ETOF rings, like the cylindrical part of the TOF, will be assembled of multigap resistive plate chambers (MRPCs). This type of detector has proven itself to be a reliable and accurate instrument for measuring the time of passage of particles. For the manufacture of ETOF rings, an MRPC design in the form of a trapezoid is proposed (Fig. 4.3.2).

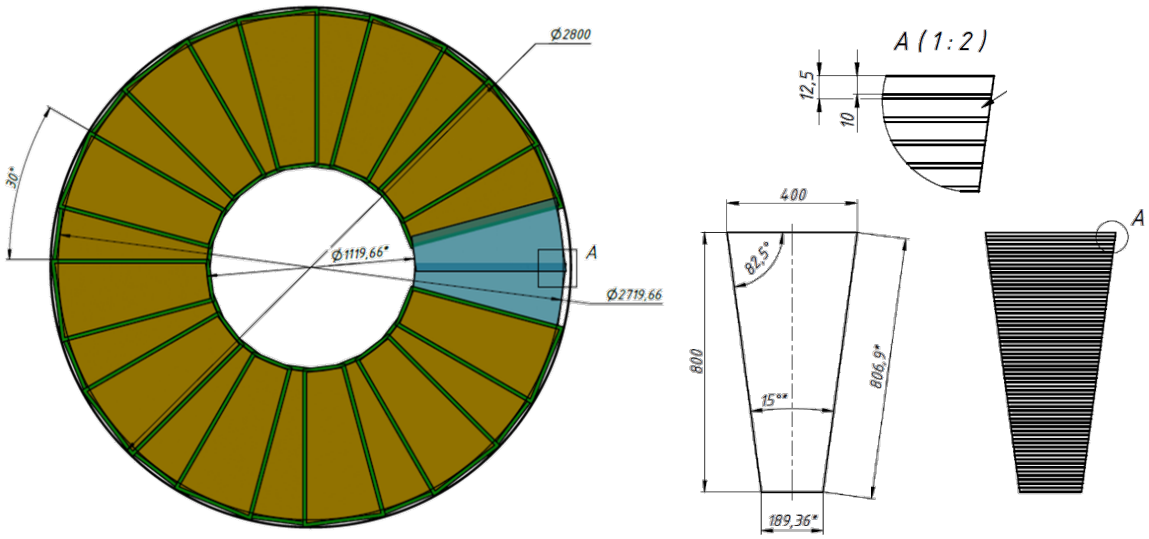

Fig. 4.3.2. The construction of the ETOF ring based on a trapezoidal MRPC.

It is proposed to make the readout electrodes of such MRPC in the form of strips of the same width as in TOF barrel detectors. This will allow using the standard principle of reading differential signals from electrodes. In the above design, the detector contains 64 strips, which, traditionally, will be read from both sides to restore the coordinates of the particle along the strip. Thus, one ETOF ring contains 24 MRPCs of 64 strips, read from two sides. In total, 3072 channels of electronics are needed to read signals from one ETOF ring. There are 6144 channels for the entire detector. This number of channels allows you to use the same combination of electronics based on NINO and HPTDC chips as in the basic configuration of the TOF MPD. However, it will be necessary to develop new discriminator preamp boards, since the redness of the 24 channels, as in the TOF preamp, is not suitable for ETOF detectors, which have 64 channels. The most likely option is a 16-channel amplifier board. In this regard, the input of the ADC will also have to be upgraded, since the CXP connector is designed for 24 differential pairs.

Preliminary modeling of the characteristics of the proposed ETOF design in MPDRoot showed that the average channel occupancy is about 8% (Fig. 4.3.3). At the same time, the radial distribution of multiplicity shows that the probability of multiple hits increases as it approaches the beam axis and may exceed 10%. This is mainly due to the large flow of secondary electrons from the substance of the reading planes of the time projection chamber - TPC.

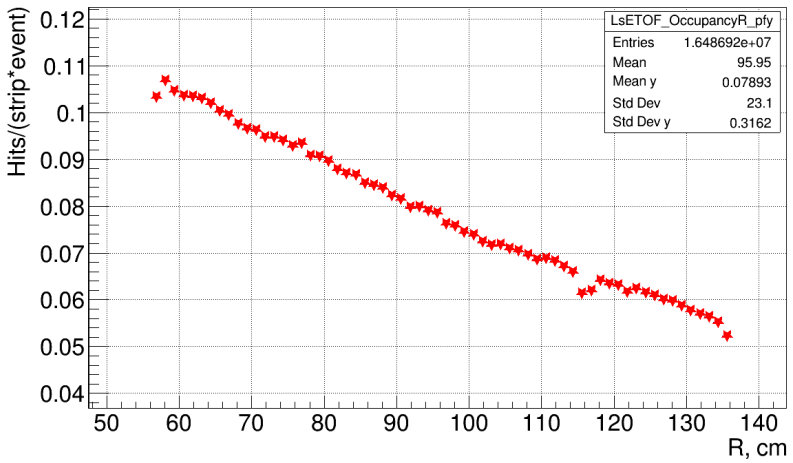

Fig. 4.3.3. Radial distribution of the occupancy of the ETOF channels at an Au-Au collision energy of 11 GeV.

4.3.2. Service subsystems

In order to put additional TOF detectors into operation, it will be necessary to modernize and supplement the service subsystems.

Gas system. In the basic version, ETOF detectors should be located inside gas volumes similar to TOF modules. In this case, the total gas volume of time-of-flight systems will increase by 1 m^3 and amount to about 4 m3. The TOF gas system will need to be upgraded to ensure that this additional volume is purged.

High-voltage power supply. If, by analogy with TOF modules, 6 detectors are supplied with high voltage from one source channel at once through a distributor, then 16 pairs of positive and negative high-voltage supply channels or 4 iSeg EHS4080p(n) modules of each polarity and 4 power distributors will be needed for both ETOF arms.

Low-voltage power supply. WIENER MPV8016I modules will also be used to power the amplifiers. If the electronics of 6 detectors (96 NINO) are powered from one connector of the module (4 channels of 50 W each) of low-voltage power supply, then 4 low-voltage power supply modules are needed for the entire ETOF. To install all HV and LV modules, you will need two MPod crates.

4.3.2. Integration

The ETOF modules must be attached to the correction coils (Fig. 4.3.4) and slide into the MPD with them. To do this, it is necessary to develop a design for attaching modules to coils. In the service position, there is constant access to the correction coils, so it will be possible to install ETOF detectors without additional devices, but only with the help of an overhead crane.

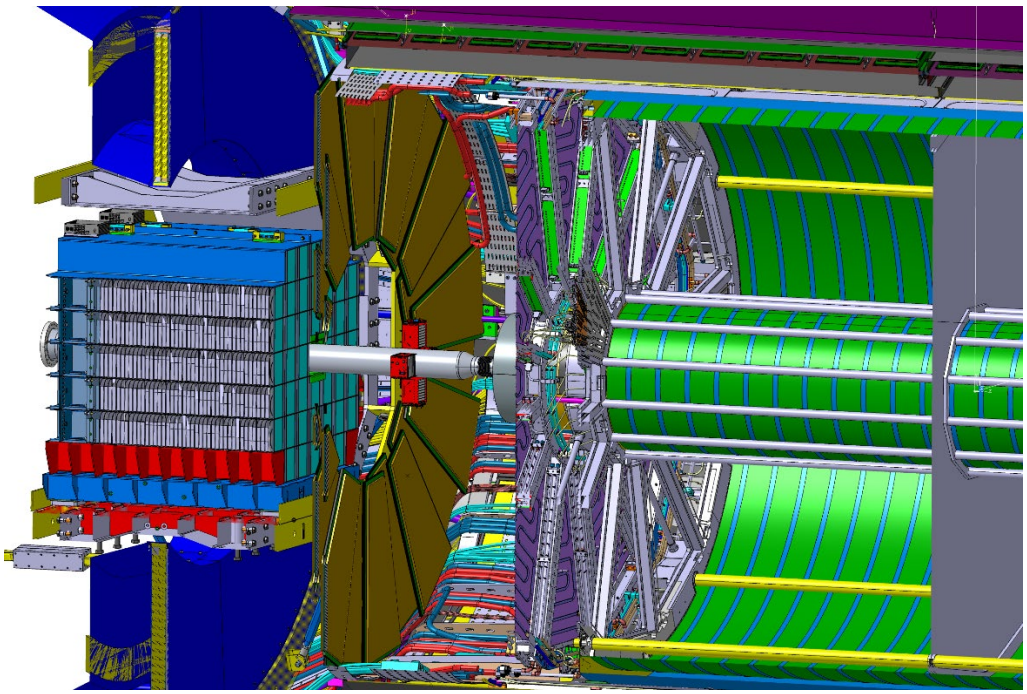

Fig. 4.3.4. ETOF mounting on the body of the correction magnet.

5. Milestones of MPD assembling in 2024-2025.

Assembling stage	Period
Preparation for switching on the solenoid magnet (cryogenics, power supply, etc.)	December 2024 - November 2025
Magnetic field measurements	Februaru - April 2025
Preparation for installation of detector subsystems	May 2025
Installation of ECal, TOF, TPC, platform with electronics, cables	May - October 2025
Installation of a beam pipe, FHCal	November - December 2025
Commissioning	December 2025
Working on a beam	December 2025

6. Cost estimation.

Proposed schedule and resource request for the MPD Project

Expenditures, resources, funding sources			Cost (thousands of US dollars)/ Resource requirements	Cost/Resources, distribution by years				
				1st year	2nd year	3rd year	4th year	5th year
		International cooperation	1000	200	200	200	200	200
		Materials	23350	3700	5250	6500	5350	2550
		Equipment, Third-party company services	6450	1100	1150	1850	1550	800
		Commissioning	300	0	50	100	100	50
		R&D contracts with other research organizations	450	100	100	100	100	50
		Software purchasing						
		Design/construction						
		Service costs (*planned in case of direct project affiliation)*	1000	200	200	200	200	200
Resources required	**Standard hours**	Resources						
		- the amount of FTE,	625	125	125	125	125	125
		- accelerator/installation,	13720	2200	2880	2880	2880	2880
		- reactor,…						
Sources of funding	**JINR Budget**	JINR budget *(budget items)*	**33000**	**5400**	**7050**	**9050**	**7600**	**3900**
	Extra fudning (supplement ary	Contributions by partners Funds under contracts with customers	500	100	100	100	100	100

Project Leader _____ V.M.Golovatyuk

Laboratory Economist _____ V.V.Morozov